Multi-Echo Radial FLASH Techniques for Real-Time MRI

Dissertation

zur Erlangung des akademischen Grades

doctor rerum naturalium
(Dr. rer. nat.)

genehmigt durch die Fakultät für Naturwissenschaften
der Otto-von-Guericke-Universität Magdeburg

von Dipl.-Phys. Markus Untenberger

geb. am 15. Mai 1985 in Villingen-Schwenningen

Gutachter: Prof. Dr. Oliver Speck

Prof. Dr. Jürgen Hennig

eingereicht am: 10. März 2015

verteidigt am: 9. Oktober 2015

Erklärung

Hiermit erkläre ich, dass die von mit eingereichte Dissertation mit dem Thema

Multi-Echo Radial FLASH Techniques for Real-Time MRI

selbstständig verfasst, nicht schon als Dissertation verwendet habe und alle benutzten Hilfmittel und Quellen angegeben sind.

Weiterhin erkläre ich, dass ich weder diese noch eine andere Arbeit zur Erlangung des akademischen Grades doctor rerum naturalium (Dr. rer. nat.) an anderen Einrichtungen eingereicht habe.

Göttingen, November 12, 2015

Markus Untenberger

Abstract

Magnetic resonance imaging (MRI) is a widely used diagnostic tool in medicine, which allows for the acquisition of cross-sectional images with a wide range of contrasts. However, because MRI emerges as a line scanning method in Fourier space, the data acquisition is relatively slow. Over the past decades faster acquisition techniques and image reconstruction methods have been proposed which mostly exploit undersampled datasets for accelerated imaging.

In this thesis, multiple gradient-echo MRI techniques have been translated from conventional settings to the conditions encountered for highly accelerated real-time MRI. The underlying data acquisition scheme is based on radial FLASH sequences, while corresponding iterative image reconstructions are accomplished with the use of a regularized nonlinear inversion (NLINV) as recently developed for real-time MRI using single gradient echoes. Here, both the - for radial MRI rather critical - gradient delay correction and various aspects of the image reconstruction method were extended to multi-echo radial data.

A first multi-echo radial FLASH application addressed here refers to T_2^* mapping, where the influence of motion on single-echo and multi-echo real-time acquisitions was investigated with the use of a motion phantom. Since the MRI physics of moving spins are well understood, the experimental findings could accurately be explained. As a possible medical application preliminary estimates of cardiac T_2^* in real-time reveal a T_2^* variation during the cardiac cycle, which may be attributed to differences in cardiac perfusion, tissue oxygenation and myocardial motion.

A second multi-echo radial FLASH technique which could be modified for real-time MRI is water-fat separation. A variety of water-fat separation methods were successfully implemented and experimentally tested, including saturation methods, Dixon methods and advanced echo-time independent methods. Water or fat saturation in real-time is accomplished by saturation pulses not before each measured k-space line, but between each frame. Due to the longer T_1 of water protons, the saturation approach favours water saturation, although fat saturation is also possible. The dependence of T_1 on magnetic field strength allows for an improved saturation at a field strength of 7 T.

Most of the implemented multi-echo water-fat separation methods were capable of generating correctly separated water and fat maps. However, for moving objects a reliable water-fat separation in real-time required the incorporation of prior knowledge. In this thesis, the use of temporal continuity was found to be very effective, leading to temporal phase unwrapping for the Dixon methods. In the two most promising water-fat separation methods, i.e. 'Analytical water/fat separation with a safest-first region-growing scheme' (ASR) and 'Iterative Decomposition of water and fat with Echo Asymmetry and Least-squares' (IDEAL), temporal continuity was successfully implemented using a coherent region growing with consideration of the previous frame in case of ASR. For IDEAL the field inhomogeneity map from the previous frame was exploited as initial guess. These methods in conjunction with NLINV reconstruction could be optimized for a qualitative water-fat separation in real-time. With respect to fat quantification a further method based on the optimized real-time IDEAL is proposed, which takes into account several confounding factors for fat quantification.

Phase unwrapping of in vivo images is a complex task, but was required for water-fat separation methods when moving to real-time MRI. As another clinically relevant application, spatiotemporal phase unwrapping was developed for velocity-encoded phase-contrast data. This allows for real-time flow MRI and was complemented by an automatized segmentation and analysis software. This strategy offered the possibility to reduce the velocity encoding gradient and achieve a corresponding increase in velocity-to-noise ratio.

In summary, in the first part of this thesis a robust physical gradient delay correction was developed for multi-echo radial real-time MRI sequences. As a technical prerequisite, this achievement then allowed for the successful adaptation of advanced techniques such as T_2^* mapping, water-fat separation and flow quantification to the growing real-time MRI regime.

Zusammenfassung

Die Magnetresonanz-Tomographie (MRT) ist ein weit verbreitetes Verfahren der diagnostischen Bildgebung in der Medizin, mit dem Querschnitte des menschlichen Körpers in vielen unterschiedlichen Kontrasten aufgenommen werden können. Durch die zeilenweise Datenaufnahme im Fourierraum ist die MRT jedoch im Prinzip eine relativ langsame Messtechnik, welche durch die Entwicklung von schnellen Messsequenzen und Rekonstruktionsalgorithmen, die erfolgreich auf stark unterabgetasteten Daten angewendet werden können, mittlerweile stark beschleunigt wurde.

In dieser Doktorarbeit werden konventionelle Multi-Echo Methoden auf Verfahren der Echtzeit-MRT übertragen. Die Messdaten werden mit einer auf die Bedingungen der Echzeit-MRT zugeschnittenen radialen FLASH Sequenz aufgenommen und mit einer zeitlich regularisierten, nicht-linearen Inversion (NLINV) rekonstruiert. Die Bildrekonstruktion und die für radial ortskodierte Messungen unverzichtbare Korrektur der physikalischen Gradientenverzögerung wurden auf die Multi-Echo Messdaten angepasst bzw. weiterentwickelt.

Eine erste Anwendung der radialen Multi-Echo FLASH-Technik ist die T_2^* Kartierung. Dazu wurde systematisch der Einfluss von Bewegung auf Einzel- und Multi-Echo Messungen an einem Bewegungsphantom untersucht. Da die zugrundeliegende Physik der MRT auch in Gegenwart von Bewegungen vollständig verstanden ist, kann die beobachtete T_2^* Verkürzung bei Bewegung exakt erklärt werden. Eine mögliche Anwendung ist die T_2^* Kartierung am Herzen und die damit verbundene Messung der Durchblutung des Herzmuskels in Echtzeit. Die vorläufigen Ergebnisse zeigen eine periodische Veränderung der T_2^* Werte während des Herzschlages, die auf eine Variation der Durchblutung, der Sauerstoffsättigung und der Bewegung des Herzens deutet.

Eine zweite Anwendung der radialen Multi-Echo FLASH-Technik ist die Wasser-Fetttrennung. Von den beschriebenen Verfahren wurden unter anderem die Sättigungsmethoden, die Dixon Methoden und fortgeschrittene Methoden umgesetzt, die von der Wahl bestimmter Echozeiten unabhängig sind. Die klassische Sättigungsmethode sättigt entweder Wasser oder Fett vor der Aufnahme jeder Linie aus dem Fourierraum. Durch die kurze Aufnahmedauer der Echtzeit-MRT genügt es, vor jedem Bild die Wasser- oder Fettprotonen zu sättigen, wobei die lange T_1 Relaxationszeit von Wasser die Wassersättigung begünstigt. Die längeren T_1 Relaxationszeiten bei einer Feldstärke von 7 T verbessern dabei die Qualität der Wasser- und Fettgesättigten Bilder.

Die implementierten Wasser-Fetttrennungsalgorithmen liefern gute Wasser- und Fett-Bilder, jedoch muss bei Echtzeit-Anwendungen der zeitliche Zusammenhang zwischen den Daten genutzt werden, um auch bei Bewegung korrekte Trennungen zu erhalten. Bei den Dixon-Methoden wurde daher ein zeitliches Phase Unwrapping entwickelt. Bei den zwei vielversprechendsten Algorithmen 'Analytical water/fat separation with a safest-first region-growing scheme' (ASR) und 'Iterative Decomposition of water and fat with Echo Asymmetry and Least-squares' (IDEAL) wurde der zeitliche Zusammenhang einerseits über das Region Growing unter Berücksichtigung des vorherigen Bildes (ASR) und andererseits durch die Verwendung der vorherigen Feldinhomogenitätskarte als Anfangswert (IDEAL) berücksichtigt. Diese beiden Methoden wurden zusammen mit der NLINV Bildrekonstruktion optimiert. In dem IDEAL Algorithmus für die Echtzeit-MRT wurden zusätzliche Korrekturen implementiert, die eine Quantifizierung des Fettanteils erlauben.

Schliesslich wurde für geschwindigkeitskodierte Phasenkontrast-Messungen in Kombination mit einer automtischen Gefäßsegmentierung ein räumlich-zeitlicher Phase Unwrapping Algorithmus entwickelt. Mit dieser Technik kann die Geschwindigkeitskodierung reduziert werden, was für quantitative Flussmessungen in Echtzeit zu einem erhöhten Geschwindigkeits-zu-Rausch Verhältnis führt.

Zusammenfassend wurde in der vorliegenden Arbeit eine robuste Methode für die physikalische Gradientenverögerungskorrektur entwickelt, die für die radiale Multi-Echo FLASH MRT in Echtzeit unverzichtbar und eine wesentliche technische Voraussetzung ist. Auf dieser Grundlage konnten mehrere spezifische MRT-Verfahren wie die T_2^* Kartierung, die Wasser- und Fetttrennung und die quantitative Flussmessung erfolgreich auf die exprimentellen Bedingungen der Echtzeit-MRT umgesetzt werden.

Acknowledgements

First of all, I would like to thank Prof. Dr. Jens Frahm, Head of Biomedizinische NMR Forschungs GmbH am Max-Planck-Institut für biophysikalische Chemie, for the support of my work, extensive assistance in the preparation of manuscripts and presentations and for the opportunity to perform research in this excellent research facility.

I am very grateful to Prof. Dr. Oliver Speck from the Department Biomedizinische Magnetresonanz at the Institut für Experimentelle Physik in the Fakultät für Naturwissenschaften of the Otto-von-Guericke University for the supervision of my thesis and for the continuous support of my scientific work.

I am deeply indebted to my colleagues Sebastian Schätz, Dirk Voit and Volkert Roeloffs for uncountable discussions, encouragement, and guidance throughout the years.

Further, I would like to thank all the present and former staff members of the Biomedizinische NMR Forschungs GmbH for a very pleasant working atmosphere and numerous table-soccer sessions.

Finally, I owe my deepest gratitude to Johanna, my parents, family, and friends for encouraging me and for helping to keep my life in context.

Contents

Chapter 1

Introduction

The development of nuclear magnetic resonance (NMR) traces back to the early 20th century when Sir Joseph Larmor found the Larmor equation. Later, in 1946, Edward Purcell and Felix Bloch discovered that certain nuclei are able to absorb electromagnetic energy when placed into a magnetic field and jointly received the Nobel Prize in Physics for the measurement of precessional signals of spins in water and paraffin samples. Felix Bloch also developed a phenomenological equation of motion for a classical magnetic moment in a magnetic field.

In 1974 Paul C. Lauterbur and Sir Peter Mansfield developed the spatial localization of the NMR signal by the use of magnetic field gradients. Their discoveries laid the foundation for magnetic resonance imaging (MRI) which was awarded with the Nobel Prize in Medicine in 2003. Another important step was made by Richard Ernst, who realized that Lauterbur's back-projection image reconstruction can be replaced by the Fourier transform if switched gradient fields are used.

Today MRI is widely used in medicine as a noninvasive tool for diagnostic imaging. It allows for the acquisition of cross-sectional and even three-dimensional images of humans and animals with a wide range of different contrasts. However, since MRI is a line scanning method in Fourier space, data acquisition is relatively slow. First major speed-ups were achieved with the invention of echo-planar imaging (EPI, [1]) and later by the fast-low angle shot sequence (FLASH, [2]). A second more recent speed-up came with the advent of parallel imaging, extreme data undersampling, and the development of corresponding iterative image reconstruction algorithms [3–7].

With these fast data acquisitions and advanced image reconstructions methods, both data acquisition and image reconstruction may be performed within a few tens of milliseconds [8, 9]. However, many of the so far developed real-time techniques are limited to single-echo data acquisitions [8]. Multi-echo acquisitions offer access to more contrasts, quantitative parameters like T_2 or T_2^* and image-based water-fat separation, all of which are active research areas in the MRI community, even without the challenges emerging from real-time MRI.

The focus of this thesis is to provide multi-echo methods for real-time MRI, thereby offering less patient restrictions, faster examination times and possibly dynamic diagnostics. The chosen real-time MRI technique relies on a radial FLASH sequences and serial image reconstruction by regularized nonlinear inversion (NLINV) [6, 8, 10].

The NLINV algorithm and a previous in-plane gradient delay correction for radial MRI [11] are extended to deal with multi-echo data. Additionally, the gradient delay is further developed to cope with asymmetric gradient echoes [12] as well as to estimate the physical gradient delays using the slice orientation, thereby improving the gradient delay correction.

Similar to T_2, T_2^* may serve as a biomarker representing normal or abnormal microstrucures [13–15], or even provide access to tissue perfusion via the oxygenation of blood [16–18]. Besides

that, T_2^* is already widely used as a marker for liver iron concentration to guide chelation therapy in transfusion dependent patients [19, 20]. The developement of T_2^* mapping in real-time in this thesis starts with the evaluation of different T_2^* fitting models, in particular with regard to the large amount of acquired data. Furthermore, simulations are performed to evaluate the precision and accuracy of the different possible T_2^* fitting algorithms. The influence of motion on single- and multi-echo real-time acquisitions is investigated with the use of a motion phantom. Since the physics of MRI are well understood in the presence of motion, the observed effects are explained in detail. As a possible clinical tool cardiac T_2^* mapping in real-time and its potential relation to cardiac perfusion are investigated in preclinical applications.

Water-fat separation MRI allows to measure qualitatively and quantitatively the fat deposition in organs like liver, heart and muscles [21–23], where it must be considered for non-alcoholic fatty liver disease or diabetes. Furthermore, the current standards for fat quantification are magnetic resonance spectroscopy and biopsy, both are only local measurements neglecting a non-uniform fat distribution [22–24]. With MRI, water and fat images of the whole organ may be obtained and analysed, eliminating flaws from non-uniformity. The major challenge for water-fat separation is either the homogeneous suppression of water/fat [25] or the accurate estimation of the field inhomogeneity map for multi-echo separation methods [26, 27]. Additional challenges like motion and the processing of large amounts of data arise for water-fat separation in real-time. This thesis investigates many methods, including saturation methods, the Dixon methods [28–31] and advanced echo-time independent methods [32–34] for their suitability for water-fat separation in real-time. The limitations of the most promising water-fat separation method for real-time MRI are investigated with the parameter space of the NLINV image reconstruction. Knowledge of the confounding factors of fat quantification [22] allows their consideration and - if possible - implementation into the real-time water-fat separation methods. The saturation and echo-time independent water-fat separation methods are also investigated at a field strength of 7 T, facing much stronger field inhomogeneities, even larger data sets and prolonged T_1 values compared to a field strength of 3 T.

As a third method phase unwrapping is investigated, which is necessary for most applications deriving parameters from the phase of the complex images, e.g. phase-contrast flow MRI or field inhomogeneity mapping. Due to the periodicity of the complex exponential function, the phase values can only be determined within the range of $-\pi$ and π, which gives rise to phase wrapping. In general, phase unwrapping is a complicated task due to the presence of noise and fundamentally unwrappable phase poles [35]. Therefore, many phase unwrapping algorithms have been proposed, the most common classes are minimum norm and path integration methods [35]. Phase unwrapping in real-time faces the challenges of increased noise, the fundamental phase poles and the amount of data. These challenges are tackled with the use of a simple and fast path integration method [36] and the incorporation of prior knowledge arising from real-time water-fat separation and real-time phase-contrast flow MRI.

In summary, this thesis addresses the feasibility of a variety of conventional MRI techniques like T_2^* mapping, water-fat separation and phase-unwrapping in real-time MRI.

Chapter 2

Theory

The chapter develops the basic theory of magnetic resonance imaging, including the physics of signal generation and decay, spatial encoding and the difference between water and fat which can be used for separating both. Furthermore, sampling schemes and standard image reconstructions are presented. For more comprehensive information the reader is referred to the textbooks from Haacke [37], Slichter [38], Abragam [39], Lauterbur [40] and Bernstein [41].

2.1 Physics of Nuclear Magnetic Resonance

2.1.1 Single Spins in a Constant Magnetic Field

Consider a spin $\vec{s}$ in a constant magnetic field $\vec{B}$. According to quantum physics, the magnetic field splits the degenerated angular momentum quantum states into the allowed spin states, which is the Zeeman effect. Examples of elements usable for nuclear magnetic resonance (NMR) are given in table 2.1.

Nucleus	Spin	Magnetic Moment	Gyromagnetic Ratio in MHz/T	Abundance in human body
Hydrogen ^{1}H	1/2	2.793	42.58	88M
Deuterium ^{2}D	1	0.879	6.53	13mM
Sodium ^{23}Na	3/2	2.216	11.27	80mM
Phosphorous ^{31}P	1/2	1.131	17.25	75mM

Table 2.1: List of selected NMR usable elements and some of their properties.

The potential energy operator U of a spin in a magnetic field is given by

$$U = -\vec{\mu} \cdot \vec{B} \tag{2.1}$$

with the magnetic moment operator $\vec{\mu}$ and the magnetic field $\vec{B}$. The magnetic moment operator is defined as

$$\vec{\mu} = \gamma \vec{J} = \gamma \left(\vec{L} + \vec{S} \right) \tag{2.2}$$

with the angular momentum $\vec{J}$ composed of the orbital angular momentum $\vec{L}$ and the spin $\vec{S}$ and the gyromagnetic ratio γ.

The quantum mechanical equation of motion for a particle in a magnetic field is given by the Schrödinger equation with Hamiltonian operator $H = \frac{\vec{p}^2}{2M} + U$.

$$H\Psi = i\hbar \frac{\partial \Psi}{\partial t} \tag{2.3}$$

A general solution for a fixed angular momentum state j of the linear time-independent Schrödinger equation is

$$\Psi(\vec{r},t) = \sum_{m_j=-j}^{+j} C_{m_j}\psi_{j,m_j}(\vec{r})e^{-\frac{i}{\hbar}E_{m_j}t} \tag{2.4}$$

with the complex coefficients C_{m_j}, determined by the boundary conditions. The sum goes over the possible spin quantum states $m_j \in \{-j,\ldots,j\}$ and $\psi_{j,m_j}(\vec{r})$ is the corresponding wave function and E_{m_j} is the corresponding energy. The energy levels of a spin in a magnetic field are then

$$E_{m_j} = -\gamma m_j \hbar B_0 \tag{2.5}$$

and the energy difference between two adjacent magnetic spin states is $\Delta E = \omega_0\hbar$ with the Larmor frequency $\omega_0 = \gamma B_0$. To understand what happens over time with a stationary hydrogen spin in a constant magnetic field the expectation value of the magnetic moment operator $\vec{\mu}$ is calculated, yielding

$$\langle\mu_y\rangle = \frac{\gamma\hbar}{2}\sin\theta\sin(\phi_0-\omega_0 t) \tag{2.6}$$

$$\langle\mu_x\rangle = \frac{\gamma\hbar}{2}\sin\theta\cos(\phi_0-\omega_0 t) \tag{2.7}$$

$$\langle\mu_z\rangle = \frac{\gamma\hbar}{2}\cos\theta \tag{2.8}$$

These expectation values represent a vector precessing around the z-axis at the angle θ, which is given by the constants C_m, which in turn are determined from the initial values of the Schrödinger equation (as well as the initial phase ϕ_0).

The results for the expectation value of the magnetic moment match the classical results, obtained from the solution of the equation of motion:

$$\frac{d\vec{\mu}}{dt} = \gamma\vec{\mu}\times\vec{B} \tag{2.9}$$

2.1.2 Multiple Spins in a Magnetic Field

For an atom with spin 1/2 in a magnetic two energy levels are open, either parallel or anti-parallel to the magnetic field orientation and the probability to find an atom in one of the possible state at thermal equilibrium is given by the Boltzmann factor $P(E)$:

$$P(E) = \frac{e^{-E/k_BT}}{\sum_E e^{-E/k_BT}} \tag{2.10}$$

with the energy E, the Boltzmann constant k_B and the temperature T. In thermal equilibrium, the investigated system is in thermal contact with the background reservoir, which has a given temperature, as well as an energy state and is large compared to the system under investigation. Considering N spins in the volume V, the number of spins in one specific energy level is given by

$$N_E = NP(E) = NP(E(m_j)) = N_{m_j} \tag{2.11}$$

According to the previous section, the quantization axis is defined to be the z-axis. The expectation values of the magnetic moments of single spins in a magnetic field are already known.

However, the thermal equilibrium value of N spins in a magnetic field B_0 parallel to the z-axis has not yet been calculated. The thermal equilibrium value for $\vec{M}$ is the sum over the expectation value of all N spins

$$M_z = \underbrace{N\theta\frac{\hbar^2\gamma^2 j(j+1)}{3k_B T}B_0}_{:=M_0}\cos\theta = M_0\cos\theta \tag{2.12}$$

$$M_y = M_0\sin\theta\sin(\phi_0 - \omega t) \tag{2.13}$$

$$M_x = M_0\sin\theta\cos(\phi_0 - \omega t) \tag{2.14}$$

However, with the assumption that the initial phase for every spin is different, the net magnetization in the x-y-plane vanishes and only the magnetization along the z-axis remains.

2.1.3 Magnetization in a Time-Dependent Magnetic Field

The application of a circular polarized magnetic field rotates the magnetic moment μ into the transversal plane. To derive this result two coordinate systems are considered, the reference frame which is fixed and a rotating laboratory frame, the primed frame, denoted as (x', y', z'). The rotating frame rotates around the vector $\vec{\Omega}$ of the fixed coordinate system.
Any vector $\vec{C}$ in the static frame, which is not parallel to $\vec{\Omega}$ rotates in the rotating frame by

$$\frac{d\vec{C}}{dt} = \vec{\Omega}\times\vec{C} \tag{2.15}$$

The consideration of the $\frac{d\vec{C}}{dt}$ with respect to the rotating coordinate frame where the basis vectors also change with time leads to

$$\frac{d\vec{C}}{dt} = \sum_{i=1}^{3}\frac{dV_{i'}(t)}{dt}\vec{e}_{i'}(t) + \sum_{i=1}^{3}V_{i'}(t)\frac{d\vec{e}_{i'}(t)}{dt} \tag{2.16}$$

$$= \left(\frac{d\vec{C}}{dt}\right)' + \vec{\Omega}\times\vec{C} \tag{2.17}$$

Rearranging equation 2.17 after the time derivative in the primed coordinate frame gives for the magnetic moment

$$\left(\frac{d\vec{\mu}}{dt}\right)' = \frac{d\vec{\mu}}{dt} - \vec{\Omega}\times\vec{\mu} = \gamma\vec{\mu}\times\left(\vec{B} + \frac{\vec{\Omega}}{\gamma}\right) = \gamma\vec{\mu}\times\vec{B}_{\text{eff}} \tag{2.18}$$

Equation 2.18 means that the equation of motion does not change in the rotating frame, but the magnetic field responsible for the torque is an effective field given by $\vec{B}_{\text{eff}} = \vec{B} + 1/\gamma\cdot\vec{\Omega}$.

A left circular polarized magnetic field in the x-y plane of the laboratory frame is given by

$$\vec{B}_1 = B_1\left(\cos(\omega t)\,\vec{e}_x - \sin(\omega t)\vec{e}_y\right) \tag{2.19}$$

After transformation into the rotating frame, using the rotation matrix $R_z(\theta(t))$ the magnetic field becomes

$$R_z(\theta(t))\vec{B}_1 = \begin{bmatrix}\cos\theta(t) & -\sin\theta(t) & 0\\ \sin\theta(t) & \cos\theta(t) & 0\\ 0 & 0 & 1\end{bmatrix}\begin{bmatrix}\cos(\omega t)\\ -\sin(\omega t)\\ 0\end{bmatrix} = \begin{bmatrix}B_1\cos(\theta(t)-\omega t)\\ B_1\sin(\theta(t)-\omega t)\\ 0\end{bmatrix} \tag{2.20}$$

In equation 2.20 the resonance condition is visible. If the frequency ω of the circular polarized magnetic field matches the rotational frequency of the rotating frame (rotating around Ω with the angular frequency $\theta(t)$), a constant magnetic field vector is obtained in the rotational frame, exerting a maximum torque on the magnetic moment.

2.1.4 Spin-Lattice Interaction

The multiple spin system is in thermal equilibrium and in contact to the environment, which is very large providing a continuum of energy states with which spins exchange energy. The quantum mechanical probability of an operator A to change from one state ψ_α into an other state ψ_β is given by Fermi's Golden Rule.

$$W_{\alpha\beta} = \frac{2\pi}{\hbar} \left|\langle\psi_\alpha| A |\psi_\beta\rangle\right|^2 \tag{2.21}$$

Due to energy conservation each change of a state must be accompanied by the inverse change of states. The thermal equilibrium value of the z-magnetization is dominated by the population change of the different quantum states. In the previous section, a constant population of the quantum states was assumed.

$$\frac{dM_z(t)}{dt} = \gamma\hbar \sum_{m_j} m_j \frac{dN_{m_j}}{dt} \tag{2.22}$$

The rate of change of a population of an energy level is given by the master equation:

$$\frac{dP_\alpha}{dt} = \sum_\beta \left(W_{\alpha\beta} P_\beta - W_{\beta\alpha} P_\alpha\right) \tag{2.23}$$

If $P_\beta = P'_\beta - P^0_\beta$ and $P_\alpha = P'_\alpha - P^0_\alpha$ is inserted in equation 2.23, the equation describes the trend of a system to its thermal equilibrium values p^0_α and P^0_β.

$$\frac{dP_\alpha}{dt} = \sum_\beta \left[W_{\alpha\beta}\left(P'_\beta - P^0_\beta\right) - W_{\beta\alpha}\left(P'_\alpha - P^0_\alpha\right)\right] \tag{2.24}$$

For a spin 1/2-system with only two energy states and the same exchange rates $W_{+\frac{1}{2},-\frac{1}{2}} = W_{-\frac{1}{2},+\frac{1}{2}} = W$, it is

$$\frac{dP_{+\frac{1}{2}}}{dt} = W\left[\left(P'_{-\frac{1}{2}} - P^0_{-\frac{1}{2}}\right) - \left(P'_{+\frac{1}{2}} - P^0_{+\frac{1}{2}}\right)\right] \tag{2.25}$$

$$\frac{dP_{-\frac{1}{2}}}{dt} = W\left[\left(P'_{+\frac{1}{2}} - P^0_{+\frac{1}{2}}\right) - \left(P'_{-\frac{1}{2}} - P^0_{-\frac{1}{2}}\right)\right] \tag{2.26}$$

Inserting equations 2.25, 2.26 into equation 2.22 and evaluating the sum over the two states $m = -1/2$ and $m = +1/2$

$$\frac{dM_z(t)}{dt} = \gamma\hbar\left[-\frac{1}{2}N\frac{dP(-\frac{1}{2})}{dt} + \frac{1}{2}N\frac{P(+\frac{1}{2})}{dt}\right] \tag{2.27}$$

$$= -\frac{1}{2}\gamma\hbar\left[\frac{dN_{+\frac{1}{2}}}{dt} - \frac{dN_{-\frac{1}{2}}}{dt}\right] \tag{2.28}$$

$$= -W\left[\gamma\hbar N\left(P'_{+\frac{1}{2}} - P'_{-\frac{1}{2}}\right) - \gamma\hbar N\left(P^0_{+\frac{1}{2}} - P^0_{-\frac{1}{2}}\right)\right] \tag{2.29}$$

$$= -\frac{1}{T_1}\left[M_z(t) - M_0\right] \tag{2.30}$$

With the longitudinal relaxation time $T_1 = \frac{1}{W}$ and the longitudinal magnetization $M_z(t)$ at time t and at thermal equilibrium M_0:

$$M_z(t) = \gamma\hbar N\left(P'_{+\frac{1}{2}} - P'_{-\frac{1}{2}}\right) \tag{2.31}$$

$$M_0 = \gamma\hbar N\left(P^0_{+\frac{1}{2}} - P^0_{-\frac{1}{2}}\right) \tag{2.32}$$

2.1.5 Spin-Spin Interaction

The spin-spin interaction is purely quantum mechanical and may be derived from the equation of motion for the density matrix σ which describes the quantum mechanical system of spins and lattice.

$$\frac{d\sigma}{dt} = -i\left[\sigma, \mathcal{H}\right] \tag{2.33}$$

with the Hamiltonian $\mathcal{H} = \mathcal{H}_0 + \mathcal{F} + \mathcal{H}_1(t)$, consisting of the system Hamiltonian $\mathcal{H}_0$, the "lattice" Hamiltonian $\mathcal{F}$ and the interaction or perturbation Hamiltonian $\mathcal{H}_1(t)$. However, the exact calculation is quite complicated and lengthy, therefore only the macroscopic equation for the spins along the x-direction is presented.

$$\frac{d}{dt}\left\langle I_x + S_x\right\rangle = -\frac{1}{T_2}\left\langle I_x + S_x\right\rangle \tag{2.34}$$

where

$$\frac{1}{T_2} = \gamma^4\hbar^2 I(I+1)\left[\frac{3}{8}J^{(2)}(2\omega_I) + \frac{15}{4}J^{(1)}(\omega_I) + \frac{3}{8}J^{(0)}(0)\right] \tag{2.35}$$

A similar result is obtained for $\langle I_y + S_y\rangle$. The spin-spin interaction causes an exponential decay of the transverse magnetization. However, the T_2 relaxation was derived for only two spins, if more spins are considered, the single exponential decay is only approximately true. Additionally, the spin-spin interaction is not the only relaxation mechanism, so the single exponential decay remains only an approximation.

2.1.6 Bloch Equations

In 1946 Felix Bloch proposed the description of the magnetization in external fields based on simple equations derived from phenomenological arguments. The Bloch equations cannot explain every phenomena in detail, but showed quantitative accuracy in liquids. The assumptions are as follows:

1. The equation of motion for an ensemble of free spins with magnetization $\vec{M}$ in a homogeneous magnetic field B_0 is

$$\frac{d\vec{M}}{dt} = \gamma\vec{M} \times \vec{B}_0 \tag{2.36}$$

2. In a static magnetic field $\vec{B}_0 = B_0\vec{e}_z$, the trend of the magnetization M_z towards its equilibrium value M_0 is governed by

$$\frac{dM_z}{dt} = -\frac{M_z - M_0}{T_1} \tag{2.37}$$

with the longitudinal relaxation time T_1.

3. If the magnetization is given a transverse component, this magnetization relaxes with the transverse relaxation time T_2 due to interactions of the spins between themselves and their surroundings.

$$\frac{dM_x}{dt} = -\frac{M_x}{T_2} \tag{2.38}$$

$$\frac{dM_y}{dt} = -\frac{M_y}{T_2} \tag{2.39}$$

4. All the previous effects can be superimposed in the presence of a large constant magnetic field and a much smaller RF magnetic field yielding the Bloch Equation.

$$\frac{d\vec{M}}{dt} = \gamma\vec{M} \times \vec{B} - \frac{M_x\vec{e}_x + M_y\vec{e}_y}{T_2} - \frac{M_z - M_0}{T_1}\vec{e}_z \tag{2.40}$$

The magnetic field $\vec{B}$ consists of the homogeneous main magnetic field $\vec{B}_0$ and a left circular polarized, much smaller magnetic field $\vec{B}_1$. The left circular polarized magnetic field is at rest in the rotating coordinate system, which is denoted with a prime, e.g. $\vec{e}_{x'}$ and rotates around the z-axis. The effective magnetic field in the rotating frame is then

$$\vec{B}_{\text{eff}} = \left(B_0 - \frac{\omega}{\gamma}\right)\vec{e}_{z'} + B_1\vec{e}_{x'} \tag{2.41}$$

In an inhomogeneous magnetic field, where not only a single resonance component is present, but a spread of Larmor frequencies $\Delta\omega$ the steady state solution of the transverse magnetization decays faster. This faster T_2^* decay is composed of T_2 and an additional parameter T_2' which is determined by the spread $\Delta\omega$.

$$\frac{1}{T_2^*} = \frac{1}{T_2'} + \frac{1}{T_2} \tag{2.42}$$

A differential equation for the transverse magnetization, defined by $M_{\text{tranv}} = M_x + iM_y$, may be introduced:

$$\frac{dM_{\text{transv}}}{dt} = -\frac{M_{\text{transv}}}{T_2^*} \tag{2.43}$$

2.2 Magnetic Resonance

2.2.1 Signal Detection

The magnetic flux Φ generated by $\vec{M}(\vec{r},t)$ through a coil with a receive field $\vec{B}_{\text{rec}}(\vec{r})$ in the volume V is given by

$$\Phi(t) = \int_V \vec{B}_{\text{rec}}(\vec{r}) \cdot \vec{M}(\vec{r},t)dV \tag{2.44}$$

According to Faraday's Law, a change in the flux Φ induces a voltage U in the coil and this voltage is regarded as the raw NMR signal.

$$U(t) = \frac{d}{dt}\int_V \vec{B}_{\text{rec}}(\vec{r}) \cdot \vec{M}(\vec{r},t)dV \tag{2.45}$$

Inserting in the Bloch equations, interchanging the integration and the differentiation and neglecting M_z, since it varies much slower compared to the fast rotating transverse magnetization, the NMR signal is

$$\begin{aligned} U(t) = \int_V \Big[& B_{x,\text{rec}}(\vec{r})\frac{d}{dt}\left|M_{xy}(\vec{r},0)\right| e^{-t/T_2(\vec{r})}\cos\left(-\omega(\vec{r})t + \phi_e(\vec{r})\right) \\ & + B_{y,\text{rec}}(\vec{r})\frac{d}{dt}\left|M_{xy}(\vec{r},0)\right| e^{-t/T_2(\vec{r})}\sin\left(-\omega(\vec{r})t + \phi_e(\vec{r})\right)\Big] dV \end{aligned} \tag{2.46}$$

The change of coordinate systems for the Bloch equation were done with the exact rotation frequency (on-resonance), so that $\Delta\omega = 0$ and $\phi_e(\vec{r})$ is the initial phase of the transverse magnetization.

Performing the time derivative allows to neglect the terms proportional to $\frac{1}{T_2(\vec{r})}$, since $\omega(\vec{r}) \ll \frac{1}{T_2(\vec{r})}$

$$U(t) = \int_V -\omega(\vec{r}) \left[|B_{xy,\mathrm{rec}}(\vec{r})|\, |M_{xy}(\vec{r},0)|\, e^{-t/T_2(\vec{r})} \sin\left(-\omega(\vec{r})t + \phi_e(\vec{r}) - \phi_r(\vec{r})\right)\right] \tag{2.47}$$

With $B_{x,\mathrm{rec}}(r) = |B_{xy,\mathrm{rec}}(r)| \cos\phi_r(\vec{r})$ and $B_{y,\mathrm{rec}}(r) = |B_{xy,\mathrm{rec}}(r)| \sin\phi_r(\vec{r})$.
Equation 2.47 is the basic signal equation for the raw NMR signal and to simplify detection, the signal is demodulated with a demodulation frequency Ω. Demodulation means that the signal is multiplied by a reference signal $2\cos\Omega t$. After demodulation the signal is low-pass filtered.

$$F_{\mathrm{low}}\left[2V(t)\cos\Omega t\right] = \int_V \omega(\vec{r}) \left[|B_{xy,\mathrm{rec}}(\vec{r})|\, |M_{xy}(\vec{r},0)|\, e^{-t/T_2(\vec{r})} \cos\left(\left(\Omega - \omega(\vec{r})\right)t + \phi_e(\vec{r}) - \phi_r(\vec{r}) + \frac{\pi}{2}\right)\right] dV$$

The signal can be also demodulated with a sine-function and regarding the demodulated signals as orthogonal components, they can be combined to a complex signal. With the definition $\Delta\omega(\vec{r}) = \omega(\vec{r}) - \Omega$ and neglecting the term proportional to $\Delta\omega(\vec{r})$, since $\Delta\omega(\vec{r}) \ll \Omega$ the following signal equation is obtained.

$$S(t) = \int_V \Omega \left[|B_{xy,\mathrm{rec}}(\vec{r})|\, |M_{xy}(\vec{r},0)|\, e^{-t/T_2(\vec{r}) + i\left((-\Delta\omega(\vec{r}))t + \phi_e(\vec{r}) - \phi_r(\vec{r}) + \frac{\pi}{2}\right)}\right] dV \tag{2.48}$$

With the definition of $|B_{xy,\mathrm{rec}}(\vec{r})|\, e^{-i\phi_r(\vec{r})} = B^*_{\perp,\mathrm{rec}}(\vec{r})$ and $|M_{xy}(\vec{r},0)|\, e^{i\phi_e(\vec{r}) - t/T_2(\vec{r})} = M_\perp(\vec{r},0)e^{-t/T_2(\vec{r})} = M_\perp(\vec{r},t)$ the signal equation becomes

$$S(t) = \Omega e^{i\pi/2} \int_V \left[B^*_{\perp,\mathrm{rec}}(\vec{r}) M_\perp(\vec{r},t) e^{-i\Delta\omega(\vec{r})t}\right] dV \tag{2.49}$$

If the magnetic field changes with time, so does the Larmor frequency and $\Delta\omega(\vec{r})t$ needs to be replaced by an integral: $\int_0^t \Delta\omega(\vec{r},\tau)d\tau$.

2.2.2 Echoes

Due to the Spin-Spin interactions the NMR signal decays and dephases. The phase of the NMR signal is defined as

$$\phi(\vec{r},t) = -\left(\int_0^t \Delta\omega(\vec{r},\tau)d\tau + \phi_e(\vec{r}) - \phi_r(\vec{r})\right) \tag{2.50}$$

In the ideal case without spatial dependence, the phase depends only on time and is zero at $t_0 = 0$. In this ideal case the signal is maximal at time t_0 and decays with time but an echo can be formed if the phase is driven back to zero. The condition for forming an echo is therefore

$$\phi(\vec{r},t) = 0 \tag{2.51}$$

A common way to generate echoes is the use of magnetic gradient fields. With a gradient $G_x(t)$ along the x-direction, the phase of the NMR signal is

$$\phi(\vec{r},t) = -\int_0^t \Omega - \gamma\left(B_0 + G_x(t)x\right) dt \tag{2.52}$$

with the demodulation frequency Ω. If the gradient is switched constantly on during the time $[0, t_1]$ the accumulated phase at the demodulation frequency $\Omega = \gamma B_0 = \omega_0$ is

$$\phi(\vec{r}, t) = G_x x t, \qquad \text{for } 0 < t < t_1 \tag{2.53}$$

In equation 2.53 the NMR signal accumulates linearly phase with time and position and decays therefore much faster than predicted by T_2 or T_2^*. However, the dephasing can be reversed by inverting the gradient polarity from $+G_x \rightarrow -G_x$ for the time interval $[t_1, t_2]$.

$$\phi(\vec{r}, t) = G_x x t_1 - G_x x (t - t_1) = G_x x (2t_1 - t) \qquad \text{for } t_1 < t < t_2 \tag{2.54}$$

At $T_E = 2t_1$ the phase is zero and a gradient (recalled) or field echo forms. In accordance with the phase condition 2.51 a gradient echo is formed if the zeroth moment of the gradient vanishes.

$$\int_{t_0}^{t} G(\vec{t'}) dt' = 0 \tag{2.55}$$

Gradient echoes can be recalled as long as the transverse magnetization has not completely decayed, which is determined by T_2 and T_2^* for spin and gradient echoes, respectively.

2.2.3 Signal Localization

The NMR signal, as given by equation 2.48 measures a time dependent signal from a volume.

First, the excited signal is restricted to a slice, by the combination of a constant slice selective gradient, e.g. G_z and a slice or frequency selective excitation pulse like a sinc-pulse, which only excites frequencies in a defined interval, corresponding to z-positions in a defined interval.

Second, after the excitation of a slice, the signal is resolved in two dimensions using again the spatial dependence of the frequency in the presence of constant magnetic field gradients. If the G_y gradient is turned on for the time $t_1 < t < t_2$ the NMR signal gets a phase proportional to the length of the time interval, the gradient strength and the y position, which is called phase encoded. If then the G_x gradient is switched on for $t > t_2$, the signal oscillates with a frequency $f = \gamma G_x x$, which is called frequency encoded. The signal equation with phase and frequency encoded positions after slice selection is shown in equation 2.56.

$$S(t) = \Omega e^{i\pi/2} \int_A M_\perp(\vec{r}) e^{-i\gamma G_x x t + G_y y (t_2 - t_1)} dx dy \tag{2.56}$$

In the derivation of the signal equation, components along the z-axis were neglected under the assumption of a slice selective excitation. However, it is possible to excite a whole volume and to image a three dimensional volume, the signal equation is then the Fourier transform of the magnetization weighted with the receive coils.

$$S(t) = \Omega e^{i\pi/2} \int_V \vec{B}_{\text{rec}}(\vec{r}) \vec{M}(\vec{r}) e^{-i2\pi \vec{k}(t)\vec{r}} dV \tag{2.57}$$

The acquired data is k- or Fourier-space data and $\vec{k}(t)$ is the trajectory - controlled by the gradients - with which the data is acquired.

2.2.4 Phase-Contrast Flow Encoding

An isochromat moving inside the imaged volume has a time dependent position which changes according to the velocity $\vec{v}$

$$\vec{r}(t) = \vec{r}_0 + \vec{v}t \tag{2.58}$$

In the case of constant velocity and gradients the phase of an isochromat is

$$\phi(t) = -\gamma\vec{G}\vec{r}_0 t - \gamma\vec{G}\vec{v}\frac{1}{2}t^2 \qquad t \in [0,\tau] \tag{2.59}$$

The static spins generate a linear phase with time, which is used for position encoding at MRI, while flowing spins generate a phase which evolves quadratically with time. The dependence of the phase on velocity may be used to encode the velocity with bipolar gradients or to null the phase of the flowing spin, which is called flow compensation.

However, the phase evolution due to velocity causes signal loss due to the dephasing of the signal if the flow within a voxel is not uniform.

2.3 K-Space Sampling

In this section either constant or known magnetic receive fields are assumed, so that they can be absorbed into the magnetization. The Fourier transform operator $\mathcal{F}$ and its inverse $\mathcal{F}^{-1}$, as well as the trajectory operator P_k, which is a projection onto the k-space trajectory are used. The comb operator $\text{Ш}(k_x) = \Delta k \sum_{q=-\infty}^{+\infty} \delta(k_x - q\Delta k)$ represents the discrete sampling with spacing Δk of a continuous signal. The rectangular function $\text{rect}(x) = \Pi(x/W) = \Theta(x + W/2) \cdot \Theta(x - W/2)$ with the Heavyside function $\Theta(x)$ crops the data onto a symmetric interval of width W around zero. With the defined operators the imaging process of the magnetization $M(\vec{r})$ is

$$S(k) = P_k \mathcal{F}^{-1}\left[M(\vec{r})\right](k) \tag{2.60}$$

Common trajectories are Cartesian, Radial, Propeller, Rosette or Spiral, but in this work only Cartesian and radial trajectories are presented. Cartesian sampling because it is the most common and simplest sampling scheme and radial because it is used for the real-time data acquisition.

2.3.1 Cartesian Sampling

The trajectory operator for Cartesian sampling is

$$P_k(k_x, k_y) = \Pi(k_x/W)\ \text{Ш}(k_x)\ \Pi(k_y/W)\ \text{Ш}(k_y) \tag{2.61}$$

The data is sampled on a rectangular grid of width W and with spacing Δk. After an RF excitation either a single or multiple k-space lines are acquired. If multiple lines are acquired, either the same line may be repetitively acquired or with each echo another line may be acquired. The first acquisition scheme yield fully sampled k-spaces for each echo, while the second scheme yields only a single k-space consisting of multiple echoes with image contrast mainly determined by the central k-space line.

2.3.2 Radial Sampling

For radial sampling, the Cartesian sampling trajectory is transformed to polar coordinates $(x, y) \to (r, \theta)$.

$$P_k(r, \theta) = \Pi(r\cos(\theta)/W)\ \text{Ш}(r\cos(\theta))\ \Pi(r\sin(\theta)/W)\ \text{Ш}(r\sin(\theta)) \tag{2.62}$$

The signal equation is after coordinate transformation

$$S(k, \theta) = \int_V \rho(r, \phi) e^{-i2\pi k r\cos(\phi-\theta)} r dr d\phi \tag{2.63}$$

with the definitions

$$G = \sqrt{G_x^2 + G_y^2} \qquad \text{and} \qquad \theta = \arctan\left(\frac{G_y}{G_x}\right) \tag{2.64}$$

$$G_x = G\cos\theta \qquad \text{and} \qquad G_y = G\sin\theta \tag{2.65}$$

for the gradients and similar for the k-space vectors.

The radial sampling according to equation 2.63 allows to use an arbitrary number of lines, or spokes. Enforcing the Shannon Sampling theorem (as derived in the next section), a radial fully sampled dataset requires more spokes than the corresponding Cartesian data set. However, radial sampling is more tolerant to undersampling compared to Cartesian sampling [42]. Furthermore, since the k-space center is sampled with each spoke, radial sampling is more robust to motion compared to Cartesian sampling [42]. Moreover, each spoke has equal information content, perfectly suited for continuous sampling.

2.3.3 The Sampling Theorem

The Shannon sampling theorem states that a bandlimited function can be reconstructed perfectly from its sampled values taken uniformly at an interval not exceeding the reciprocal of twice the signal bandwidth [40]. For a bandlimited function with bandlimit $f_{\max}$ the sampling theorem requires that the sampling frequency f_s is

$$\frac{1}{f_s} = \Delta t \leq \frac{1}{2f_{\max}} \tag{2.66}$$

For a space limited object with limits L_x and L_y along the x- and y-direction, the sampling theorem requires to sample with

$$\Delta k_x = \frac{1}{L_x} \qquad \text{and} \qquad \Delta k_y = \frac{1}{L_y} \tag{2.67}$$

for Cartesian sampling. This means that the field of view (FOV) mus be at least L_x and L_y because the FOV along each direction is given by the product of k-space sampling points and the voxel size.

The distance between the k-space sampling points for a Cartesian trajectory is

$$\Delta k_x = \frac{\gamma}{2\pi} |G_x| \, \Delta t \tag{2.68}$$

$$\Delta k_y = \frac{\gamma}{2\pi} \Delta G_y T_{\mathrm{pe}} \tag{2.69}$$

with the sampling interval Δt, read-out gradient strength G_x and the duration of each phase encoding step T_{pe} and the increment of the phase encoding gradient ΔG_y. Substituting equations 2.67 into equations 2.68, 2.69 the conditions for the timing for frequency encoding and the gradient amplitude for the phase encoding are obtained.

$$\Delta t \leq \frac{2\pi}{\gamma \, |G_x| \, L_x} \tag{2.70}$$

$$\Delta G_y \leq \frac{2\pi}{\gamma T_{\mathrm{pe}} L_y} \tag{2.71}$$

For the radial sampling trajectory a space and frequency limited object is considered. The object is limited by radius R and R_k in image and in frequency space, respectively. The sampling

conditions for Δk and $\Delta\phi$ are

$$\Delta k = \frac{\gamma}{2\pi} G \Delta t \leq \frac{1}{2R} \tag{2.72}$$

$$\Delta\phi \leq \frac{2\pi}{2\left(2\pi R R_k + 1\right) + 1} \tag{2.73}$$

The radial sampling condition is similar to the Cartesian sampling condition. The azimuthal sampling condition is simplified if the number of samples per line N_k and their relation to the number of spokes N_ϕ is considered.

$$N_\phi \approx \frac{\pi}{2} N_k \tag{2.74}$$

E.g. for 256 k-space samples per line, a radial fully sampled data requires 403 spokes, which is actually more than in the Cartesian case.

2.3.4 Image Resolution and Bandwidth

The image resolution in MRI is determined by the point spread function from the filters which are applied to the measured the data. Both, the sampling and the truncation of the data are considered as filters. Their associated point spread function is the inverse Fourier transform of the filter.

$$h_w(x) = \mathcal{F}^{-1}\left[\mathrm{rect}(k/W)\right] = W \mathrm{sinc}\left(\pi W x\right) \tag{2.75}$$

If the data is only truncated but sampled continuously, each data point is spread by a sinc-function of width $1/(\pi W)$.

Secondly, the point spread function of the sampling is

$$h_s(x) = \mathcal{F}^{-1}\left[\text{Ш}(k_x)\right] = \Delta k \sum_{q=-\infty}^{+\infty} e^{-2\pi i q \Delta k r_x} \tag{2.76}$$

which is an infinite sum of repeated copies with distance Δk between them. The combination of both filters is obtained by either calculating the Fourier transform of the combined filters or simply by restricting the infinite sum in 2.76 to a finite sum, yielding

$$h_{ws}(x) = \Delta k \sum_{q=-n}^{n-1} e^{-2\pi i q \Delta k r_x} = W \frac{\mathrm{sinc}\left(\pi W r_x\right)}{\mathrm{sinc}\left(\pi \Delta k r_x\right)} e^{-i\pi \Delta k r_x} \tag{2.77}$$

The resolution in MRI is defined as the blur of the imaging filters, yielding that the achievable resolution Δx_{MRI} is limited by the sampling range W in k-space.

$$\Delta x_{\mathrm{MRI}} = \frac{1}{h_{ws}(0)} \int_{-W/2}^{W/2} h_{ws}(x) dx = \frac{1}{2n\Delta k} = \frac{1}{W} \tag{2.78}$$

Equation 2.78 gives the image resolution for equidistant sampling in one dimension. For Cartesian imaging, the point spread function is the same for x- and y-direction, yielding the same resolution for each direction.

$$h_{\mathrm{Cartesian}}(x, y) = h_{ws}(x) \cdot h_{ws}(y) \tag{2.79}$$

In case of radial imaging, the point-spread function for continuous radial sampling with a limited number of projections N_θ has been calculated and is given in equation 2.80 [43].

$$\mathrm{PSF}_{\mathrm{radial}}(r,\theta) = 2\Delta K_\theta \sum_{n=0}^{N_\theta-1} \left(\frac{\cos(a_n(r,\theta)k_R) + a_n(r,\theta)k_R \sin(a_n(r,\theta)k_R) - 1}{a_n^2(r,\theta)} \right) \tag{2.80}$$

with $a_n(r,\theta) = 2\pi r\cos(n\Delta k_\theta - \theta)$, k_R the maximum sampled radial k-space point and $\Delta k_\theta = 2\pi/N_\theta$ the angular increment depending on the maximum number N_θ of projections. The analytical exact blur has not yet been calculated. Azimuthal undersampling produces the well known streak artefacts which do not necessarily lead to a reduction in image resolution [43]. However, image details may be obscured by streaking artefacts cutting through the object.

2.4 Image Reconstruction

2.4.1 Cartesian Image Reconstruction

The product of magnetization and magnetic receive field is related to the spin density ρ and can be obtained by a Fourier transform of the measured signal.

$$\hat{\rho}(\vec{r}) = \int_k S(\vec{k}(t)) e^{2\pi i \vec{k}\vec{r}} d^3k \tag{2.81}$$

In case of Cartesian sampling, the discrete Fourier transform yields directly the spin density ρ.

2.4.2 Non-Cartesian Image Reconstruction

The data acquired on non-Cartesian trajectories is interpolated onto a rectangular grid on which the discrete Fourier transform is applied, yielding the desired spin density. Instead of the ideal sinc-kernel, an approximation by the Kaiser-Bessel kernel with compact support is used as interpolation kernel.

$$K_{\mathrm{KB}}(d) = \begin{cases} \frac{1}{L} I_0(\beta\sqrt{1-(2d/L)^2}) & |d| \le \frac{L}{2} \\ 0 & |d| > \frac{L}{2} \end{cases} \tag{2.82}$$

with I_0 the zero-order modified Bessel function, L the desired kernel width and the shape factor β. The measured samples are convolved with the interpolation kernel and evaluated at the "smeared" desired k-space positions. Due to the interpolation with a finite size interpolation kernel, the image exhibits an undesired modulation with the Fourier transform of the kernel, which is called roll-off effect. The roll-off effect is removed by dividing the image by the Fourier transform of the Kaiser-Bessel window, which is called roll-off correction.

$$\mathcal{F}\{K_{\mathrm{KB}}\}(x) \approx M_{\mathrm{KB}}(x) = \frac{\sin\sqrt{(\pi L x)^2 - \beta^2}}{\sqrt{(\pi L x^2) - \beta^2}} \tag{2.83}$$

Due to the use of a finite size interpolation kernel and the discrete sampling, aliasing happens. To avoid aliasing, the interpolation is performed with increased resolution, shifting the aliased copies further away from the center. Usually an increase of factor two is sufficient. Afterwards the image is cropped to the original size. Further a density compensation is necessary, since the center is sampled more densely than the outer regions. For the radial trajectory the density compensation function is a Ram-Lak filter

$$D_{\mathrm{RL}}(k) = \begin{cases} \left|\vec{k}\right| / n_s & |k| \neq 0 \\ 1/(2n_s) & |k| = 0 \end{cases} \tag{2.84}$$

Thus the gridded data is obtained by

$$\mathrm{GRD}\, S(\vec{k}) = \left(M_{\mathrm{KB}}^{-1} \cdot \mathcal{F}^{-1} \cdot \text{Ш} \cdot K_{\mathrm{KB}} * D_{\mathrm{RL}} \cdot P_k\right) S(k) \tag{2.85}$$

with the convolution denoted as $*$, the projection on the trajectory P_k, the density correction D_{RL}, the interpolation with the Kaiser-Bessel function K_{KB}, the sampling Ш, the inverse Fourier transform $\mathcal{F}^{-1}$ and the roll-off correction M_{KB}^{-1}.

Chapter 3

Materials and Methods

3.1 MRI System

All measurements were performed on commercially available MRI scanners, which are described in the following sections. Most of the measurements were done on the TimTrio scanner, including the measurements for water-fat separation, T_2^* estimations and flow measurements for phase unwrapping. Additional water-fat separation measurements were performed in Magdeburg at the 7T scanner of the Leibniz Institute for Neurobiology. The gradient delay correction for asymmetric echoes and multiple echoes was investigated using data from the Prisma MRI system.

3.1.1 TimTrio

The used TimTrio system (MAGNETOM, TimTrio System, Siemens AG, Erlangen, Germnay) has a bore length of 142 cm and an inner diameter of 60 cm with a possible Field of View (FOV) of 50 cm around the isocenter. The main magnet is helium cooled and superconducting with a field strength of $B_0 = 2.89\,\mathrm{T}$. The TimTrio system contains a single channel body coil for RF excitation and reception as well as a gradient system with a maximum gradient strength of $G_{\max} = 38\,\mathrm{mT/m}$ for each physical axis. The raster time of the gradients is $10\,\mu\mathrm{s}$ and the maximum slew rate is $170\,\mathrm{T\,m^{-1}\,s^{-1}}$. The volunteer measurements were performed with anatomically matched receive coil arrays and the phantom measurements were performed with the 32 channel (ch) head coil due to superior signal-to-noise ratio (SNR).

3.1.2 Prisma

With the beginning of the year 2014 our MRI system was upgraded from the TimTrio system to the Prisma system (MAGNETOM, Prisma System, Siemens AG, Erlangen, Germnay). Except for the magnet everything else was exchanged. The Prisma system has XR gradients which have the same raster time but an increased maximum amplitude of $G_{\max} = 80\,\mathrm{mT/m}$ and an increased maximum slew rate of $200\,\mathrm{T\,m^{-1}\,s^{-1}}$. Also the body coil has changed from a single to a two-channel excitation and reception coil. Only the 32 and 64 channel head coils haven been used for the measurement with the Prisma MRI system.

3.1.3 7T

The 7 T high-field MRI system in Magdeburg was used to investigate the water-fat separation in real-time. The 7 T MRI system is manufactured from Siemens (Siemens AG, Erlangen, Germnay), has a bore size of 60 cm and is equipped with SC 72 gradients which provide a maximum amplitude of $G_{\max} = 70\,\mathrm{mT/m}$ and a maximum slew rate of $200\,\mathrm{T\,m^{-1}\ s^{-1}}$. The

measurements were performed with a 28-channel knee coil which provides only limited space for motion of the leg.

3.2 MRI Data Acquisition

In this section the fast low-angle shot (FLASH) MRI sequence [44, 45] and the used k-space trajectory are described. Although many other sequences and variation of the k-space trajectory exist, only the FLASH sequence with a radial trajectory is used throughout this work.

3.2.1 FLASH Sequence

The FLASH sequence is a fast imaging sequence which allows for short echo and repetition times, both in the order of milliseconds. Depending on the echo time, flip angle and repetition time different contrasts can be achieved with varying SNR and contrast-to-noise ratios (CNR) [46]. Due to the build-up of transverse coherences [47] the transverse magnetization are eliminated by RF spoiling before the next RF excitation.

The FLASH sequence allows for single-echo and multi-echo acquisition schemes as presented in figure 3.1. Both acquisition schemes show the acquisition of a single spoke where data is acquired during the flat-top time of the logical x- and y-gradients. Multi-echo gradient sequences may be used for T_2^* mapping [48–50] while single echo sequences may be used for imaging with T_1 or T_2^* contrast.

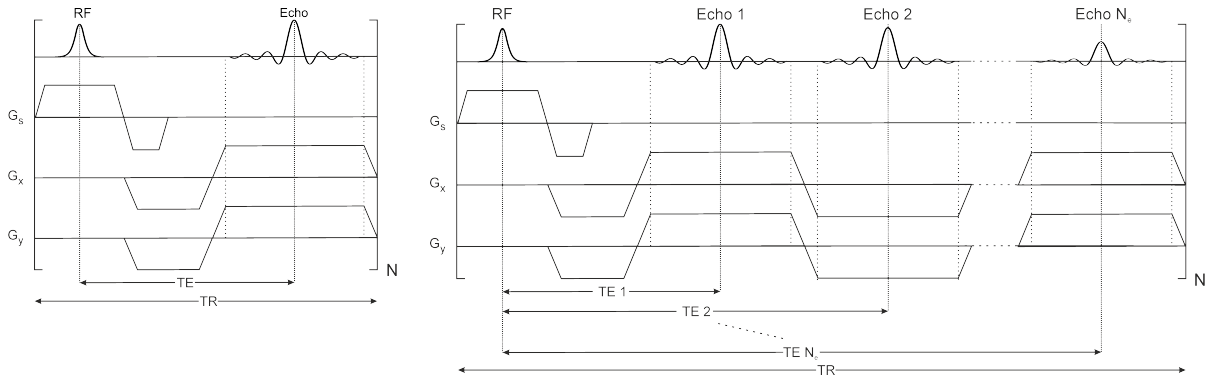

Figure 3.1: Gradient switching schemes for single (left) and multi-echo (right) FLASH sequence.

Furthermore, the FLASH sequence allows to encode velocity into the phase of an image [51, 52]. The used phase-contrast sequence acquires two images, one with and one without velocity encoding from which the velocity can be calculated [53]. The velocity-encoding gradients are switched before the read-out gradient, here a bipolar encoding gradient is used. The sequence diagram is shown in figure 3.2.

The reduction of the prephasing and read-out gradients as shown in figure 3.2 leads to asymmetric echoes. Asymmetric echoes allows for even shorter echo and repetition times at the cost of reduced SNR .

3.2.2 K-Space Trajectory

The data acquisition in this thesis uses a FLASH sequence in combination with a radial trajectory [54], which is optimally suited for real-time imaging due to the following four facts [42]:

1. Oversampling of k-space center: Each encoding line crosses the k-space center, therefore each line (or spoke) contains equally important information.

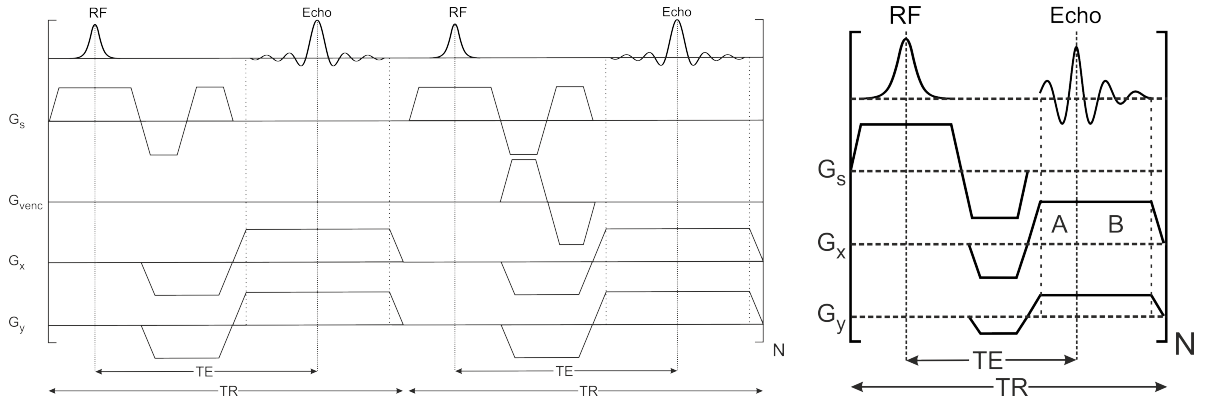

Figure 3.2: Schematic flow sequence without and with bipolar velocity encoding gradient (left) and asymmetric echo sequence (right).

2. Tolerance to undersampling: According to Nyquist a fully sampled radial k-space contains $N_\phi = \pi/2\ N_k$ spokes with N_k samples on the spoke. However, even with standard gridding reconstruction a certain reduction of spokes is possible without losing too much image quality.

3. Continuous data acquisition: New data with equally important amount of information can be acquired continuously by using a turn based acquisition scheme as shown in figure 3.3 or with a golden angle acquisition.

4. Gradient Delay correction: The logical and physical gradient delays can be obtained directly from the measured data without any calibration measurement.

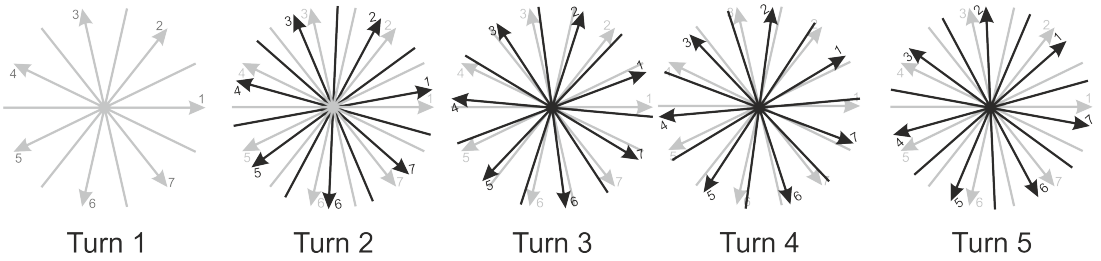

Figure 3.3: Radial acquisition scheme with 5 turns.

A typical radial acquisition with $N_t = 5$ turns is shown in figure 3.3. With each turn each acquired spoke is rotated by $\beta = 360/N_s/N_t$ with N_s the number of spokes, until after N_t the turns are repeated.

The k-space trajectory of a single line contains an even number N_k of sampling points and the gradients are switched in a way that the echo is sampled at the $N_k/2 + 1$ sample point for the odd echoes and at $N_k/2 - 1$ for the even echoes.

3.3 Image Reconstruction

Image reconstruction for data measured with a Cartesian acquisition scheme may be done by applying the Fourier transform to the data. With the advent of non-Cartesian trajectories the data must be gridded onto a rectangular grid before Fourier transformation. State of the art image reconstructions like SENSE [3], GRAPPA [4, 55] and NLINV [6, 8] for undersampled real-time data acquisitions are available.

3.3.1 NLINV

A detailed and mathematical description of the regularized non-linear inversion (NLINV) is presented in the thesis of Martin Uecker [7] and his publications [6, 8, 10], here only a short summary is presented.

In equation 2.57 the signal for only a single receive coil is presented, however, using multiple coils, multiple signals are available containing the same underlying spin density. Switching to inverse problems, the measured data y is the result of the forward operator F applied onto the generalized spin density ρ and the receive coil sensitivities c_j.

$$F : x \mapsto \begin{pmatrix} P_k \mathcal{F}(\rho c_1) \\ \vdots \\ P_k \mathcal{F}(\rho c_N) \end{pmatrix} = y \qquad \text{with} \qquad x = \begin{pmatrix} \rho \\ c_1 \\ \vdots \\ c_N \end{pmatrix} \tag{3.1}$$

Equation 3.1 is expanded using the Taylor expansion around x_n with the Jacobian $DF(x_n)$ and linearized.

$$DF(x_n)dx + F(x_n) = y \tag{3.2}$$

The lineaized problem is symmetrized by multiplication with the adjoint of the derivative and solved subsequently using a conjugate gradient algorithm. Regularization is added to counterbalance the bad conditioning of the lineaized equation, yielding the Levenberg-Marquardt algorithm. To improve the stability the regularization is changed from the update, to the result of the update. Reformulating the Gauss-Newton method into a functional, whose minimum is exactly the solution of the Gauss-Newton method yields

$$\left\| DF(x_n)dx - (y - F(x_n)) \right\|^2 + \alpha_n \left\| x_n + dx - x_0 \right\|^2 \tag{3.3}$$

The problem in equation 3.1 is highly underdetermined, as can be seen by multiplying ρ with any complex functions g and dividing the coil sensitivities by the same function g which gives another solution but has the same signal y. Therefore the algorithm can shift information between the image ρ and the coil sensitivities c_j. The prior knowledge of smooth coil sensitivities profiles allows to restrict the solution space and is incorporated into NLINV by a preconditioning matrix W

$$\hat{x} = W^{-1}x = \begin{pmatrix} I & & & \\ & \left(1 + s\left\|\vec{k}\right\|^2\right)^{l/2} \mathcal{F} & & \\ & & \ddots & \\ & & & \left(1 + s\left\|\vec{k}\right\|^2\right)^{l/2} \mathcal{F} \end{pmatrix} \begin{pmatrix} \rho \\ c_1 \\ \vdots \\ c_N \end{pmatrix} \tag{3.4}$$

leading to a redefinition of the forward operator F as $F_1\hat{x} = FW\hat{x}$. The new functional to solve is

$$\left\| DF_1(\hat{x}_n)d\hat{x} - (y - F_1(\hat{x}_n)) \right\|^2 + \alpha_n \left\| \hat{x}_n + d\hat{x} - \hat{x}_0 \right\|^2 \tag{3.5}$$

For quantitative imaging, not only the spin density, but also the coil profiles must be evaluated, therefore the final image is the following combination

$$\rho_{\text{final}} = \rho \sqrt{\sum_{i=1}^{N} \|c_i\|^2} \tag{3.6}$$

Multi-echo acquisitions require an adaptation of the NLINV algorithm. The spin density and coil sensitivities are estimated for the first echo, all following echoes use the coil sensitivities from the first echo to estimated the spin density, which reduces to a linear problem for known coil sensitivities. The temporal regularization is applied only to the first echoes.

For the phase-contrast data, first two image series ρ_0 and ρ_1 are calculated with J coil profiles c_{0j} and c_{1j}, where the index 0 and 1 refer to the velocity encodings. Weighted images $\rho_{i,j}$ are calculated

$$\rho_{i,j} = \frac{\rho_i c_{ij}}{\sqrt{\sum_{k=1}^{J} c_{ik}\bar{c}_{ik}}} \qquad i \in \{0,1\} \text{ and } j \in \{1,\ldots,J\} \tag{3.7}$$

and used for derivation of a phase difference image $\hat{\rho_{\mathrm{pc}}}$.

$$\hat{\rho}_{\mathrm{pc}} = \sum_{j=1}^{J} \rho_{0j}\bar{\rho}_{1j} \tag{3.8}$$

In order to deal with the enormous amount of data from real-time acquisitions, the data is compressed using principal component analysis (PCA) [56, 57] before image reconstruction. The image reconstruction is speeded up to the acquisition frame rate by using graphic processing units (GPU) and specialized software [9, 58] which unleash the full parallel power of the GPUs.

All further processing of the data, like T_2^* mapping, water-fat separation or phase unwrapping is performed directly on the reconstructed spin densities and coil sensitivities.

3.4 Real-Time MRI

Real-time MRI refers to the continuous data acquisition and image reconstruction of moving objects in real time. However, MRI is an intrinsic slow technique due to the large number of excitations needed to acquire a fully sampled k-space. Undersampled data is acquired faster but complexity of and computational demand for the image reconstruction increases. The complexity of the reconstruction is reflected in the non-linear nature of the image reconstruction problem, which is properly treated by NLINV, yielding even for highly undersampled data high quality images [6, 7]. The computational demand for the image reconstruction is taken care of by 2x4 GPUs (sysGen/TYAN Octuple-GPU, 2x Intel Westmere E5620 processor, 48GB RAM, Sysgen, Bremen, Germany) and an optimized version of NLINV [9, 58]. The whole process is fully integrated into the reconstruction pipeline of the commercial MRI system.

Using the radial FLASH sequence, movies with a temporal resolution of 20 to 30 ms can be acquired and reconstructed at frame rates of about 11 frames per second [9, 54]. Although the frame rate of the reconstruction is lower than the image acquisition rate, the integration into the commercial MRI system allows for online display of the acquired data, allowing real-time MRI.

The limits of the real-time data acquisition and a post processing median filter have been evaluated by Jens Frahm, the author and others within the research group [59]. The application of the median filter keeps edges but smooths peaks out [60, 61]. For the phase of the phase-contrast data, water-fat separation, phase unwrapping and T_2^* mapping the median filter is deactivated and may be applied after the respective operation. The reconstructed images can further be improved if a motion estimation is applied during the reconstruction [62].

In this thesis, real-time MRI refers primarily to the data acquisition and only secondly to the image reconstruction and display in real time. The image reconstruction and display in real time is a huge engineering task which may only be solved after robust image reconstructions at reduced frame rates have been developed. Furthermore, T_2^*, water/fat maps and phase-contrast flow analyses of real-time MRI data are usually performed offline after the image acquisition and reconstruction.

3.5 Software

3.5.1 In-house Software

The NLINV image reconstruction as developed by Martin Uecker and speeded up by Sebastian Schaetz was used extensively and extended to multi-echo data. The reconstruction is written in C/C++ and CUDA, depending on which hardware it is supposed to run. A Matlab version of NLINV was written by Housen Li, which was used to test and change the image reconstruction. Due to the slow reconstruction speed of the Matlab NLINV, the Matlab NLINV was soon replaced by a Matlab callable GPU version of NLINV.

The ArrayShow software is developed by Tilman Sumpf [63, 64] and was used to display the multidimensional MRI data. Many features like displaying the phase as an overlay, switching between magnitude, complex, real, imaginary and phase visualization, ROI evaluation simplify the development of new techniques.

The improvement of the gradient delay correction requires access to the raw data which is provided by dat2coo. dat2coo was initially written by Martin Uecker and converts the raw data as stored in the dat-file into a Matlab readable coo. Aaron Niebergall and myself rewrote dat2coo so that no input arguments except the dat-file are needed.

A simple software for the measurement of the rotation velocity of the motion phantom using a webcam and the MRI manufacturers video surveillance camera was written by Sebastian Schaetz and myself [9, 59, 65]. The software uses either one or two red dots on the rotating disk and by extracting the number of red pixels from the webcam data, which in turn captured the images from the manufacturers video surveillance screen, intensity curves were created. Using either the peak position or the rise time the repetition frequency of the red dot(s) can be determined using the cameras frame rate. Verification of this method was performed using phase-contrast measurements.

3.5.2 Out-house Software

The major work of this thesis was done in Matlab (MathWorks, Natick, NA) due to its enormous functionality and simplicity. If speed becomes an increasingly important factor, Matlab offers mex-files, which provide an interface faster C/C++ binaries. Some mex-files have been produced to replace time-consuming Matlab code.

Another important software is the CAIPI (Integrated Processing of Multimodal Cardiac Image Data) software [66], which was used for the analysis for the phase-contrast data and the ROI segmentation for the phase unwrapping.

3.5.3 Exponential Fitting

An exponential function of the form

$$y(x) = Ae^{Bx} \tag{3.9}$$

is easily lineaized by taking the logarithm

$$\log y(x) = \log A + Bx \tag{3.10}$$

and directly fitted in a least-square sense. However, the solution in equation 3.10 gives greater weight to small y values and to weight the points equally the following function must be minimized [67]

$$f(a,b) = \sum_{i=1}^{n} y(x_i) \left(\log(y(x_i)) - a - bx_i\right)^2 \tag{3.11}$$

The least-squares solution is

$$a = \frac{\sum_{i=1}^{n}\left(x_i^2 y_i\right)\sum_{i=1}^{n}\left(y(x_i)\log(y(x_i))\right) - \sum_{i=1}^{n}\left(x_i y(x_i)\right)\sum_{i=1}^{n}\left(x_i y(x_i)\log y(x_i)\right)}{\sum_{i=1}^{n} y(x_i)\sum_{i=1}^{n}\left(x_i^2 y(x_i)\right) - \left(\sum_{i=1}^{n} x_i y(x_i)\right)^2} \tag{3.12}$$

$$b = \frac{\sum_{i=1}^{n} y(x_i)\sum_{i=1}^{n}\left(x_i y(x_i)\log y(x_i)\right) - \sum_{i=1}^{n}\left(x_i y(x_i)\right)\sum_{i=1}^{n}\left(y(x_i)\log(y(x_i))\right)}{\sum_{i=1}^{n} y(x_i)\sum_{i=1}^{n}\left(x_i^2 y(x_i)\right) - \left(\sum_{i=1}^{n} x_i y(x_i)\right)^2} \tag{3.13}$$

with $b = B$ and $A = \exp a$.

3.6 Phantoms and Volunteers

3.6.1 T_2^* Phantoms

The T_2^* phantoms were produced using agarose in different concentrations doped with $CuSO_4$. Usually, 2% agarose gives a T_2 value around 50ms, which may be shortened further [68–71]. However, the production of T_2^* phantoms is not well investigated because T_2^* depends on the magnetic field as well as the shape and structure of the phantom and its interfaces. The T_2^* phantoms were produced similarly as describe in [72]. Due to the evaporating water from the agarose fluid the containers must be sealed airtight to keep their properties for at least 12 months [72].

3.6.2 Motion Phantom

The motion phantom has been developed by Aaron Niebergall, Sebastian Schaetz and myself in order to analyse the capabilities of our image acquisition and reconstruction [59, 65, 73]. The motion phantom is a low-cost phantom, consisting of a rotating disk which is driven by air pressure, see figure 3.4. The measurement of the rotational velocity is described in 3.5.1 and in [73]. The phantom has two different interchangeable plastic disks, one disk for small vials and another disk for petri dishes. The petri dishes can be filled e.g. with agarose containing holes. Besides the evaluation of our real-time framework the phantom was used to investigate the effects of motion onto T_2^* and the signal intensity, see chapter 5.

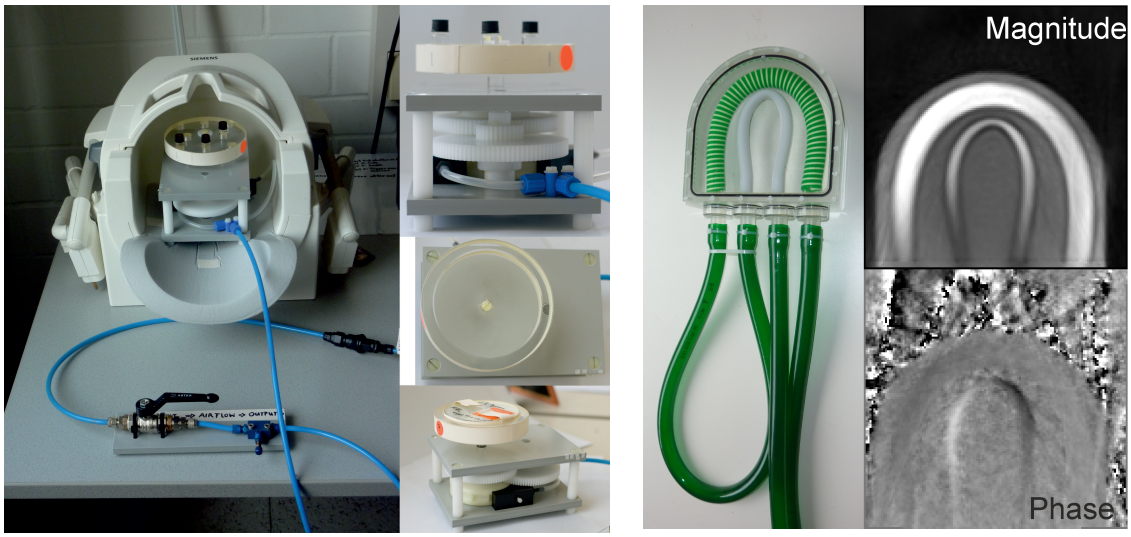

Figure 3.4: Motion Phantom with its different specimen holder and the experimental setup (left) and the flow phantom (right).

3.6.3 Flow Phantom

The flow phantom has been developed by Arun Joseph and described in detail in his thesis, various publications and conference contributions [53, 74–76]. In short, a voltage controlled pump allows to produce pulsatile flow at different duty cycles and velocities. The fluid is pumped through a long tube that enters a water filled half disk and exits it after a u-turn and enters it again but with a reduced diameter, performs another u-turn and exits the phantom, see figure 3.4. The tubes continue within the half disk, so that the flowing fluid cannot mix with the static fluid. The flow phantom was used for the real-time flow phase unwrapping investigations, see chapter 7.

3.6.4 Numerical Phantoms

Numerical flow phantoms were produced from measured data with a velocity encoding (VENC) where no phase wraps occurred. Simulated phase wraps were generated by retrospectively reducing the phase interval from $[-\pi, \pi]$ to $[-\pi/2, \pi/2]$. Values above $\pi/2$ (below $-\pi/2$) were added (subtracted) by π, while all values within $[-\pi/2, \pi/2]$ remained unchanged. To obtain wrapped phase data within $[-\pi, \pi]$ all values were subsequently multiplied by two. The corresponding datasets with artificially decreased VENC were unwrapped and analyzed the same way as applied for the original data and the results were compared to the evaluations of the original data without phase wraps (ground truth). An example is shown in figure 3.5.

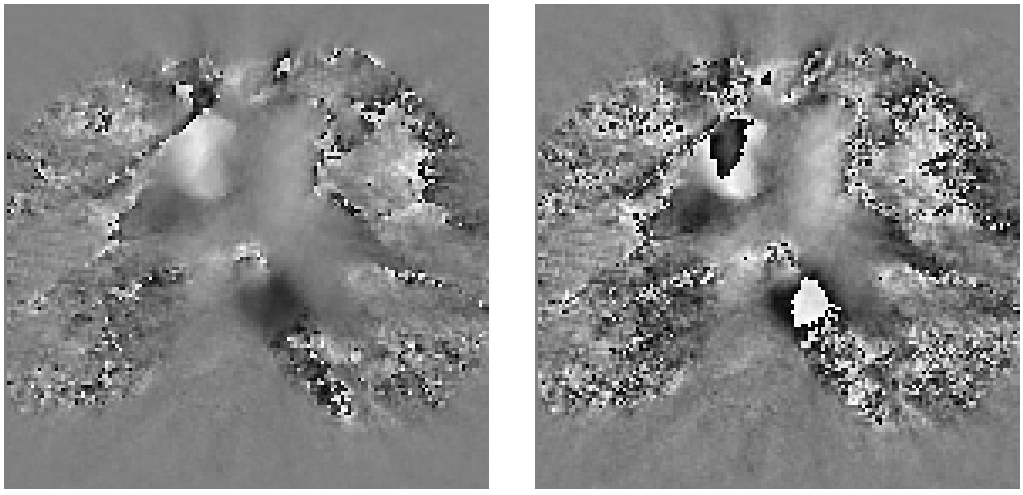

(a) original data (b) simulated wrapped data

Figure 3.5: Simulated phase (wrapped) data in and the respective original phase data.

A numerical gradient delay phantom was developed based on the theory for gradient delay [77] and the Shepp-Logan phantom [78]. The ideal gradient switching for all three gradients is simulated in the logical gradient system, according to our radial FLASH sequence (see figure 3.1). The RF pulse is assumed to be a δ-pulse for simplicity and because the trajectory can only be influenced if any MR signal has been excited. Knowing the gradients in the logical gradient system they are transformed according to the slice orientation into the physical gradients where the actual delay takes place. The simulation implements any slice orientation and individual delays for each physical gradient axis. After the physical gradients are delayed they are transformed back into the logical gradient system to generate the delayed trajectory. The delayed trajectory can be used with the analytical k-space Shepp-Logan phantom[78] to generate delayed k-space data.

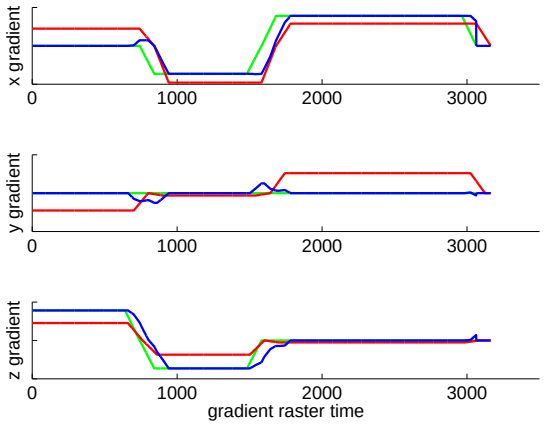

(a) Gradients

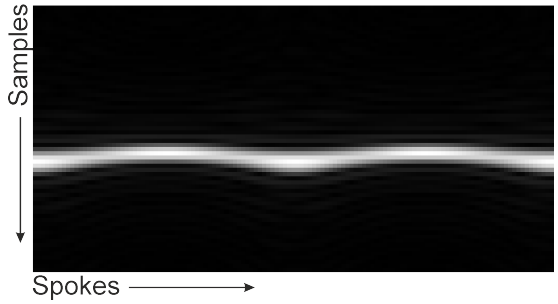

(b) k-Space (magnitude)

Figure 3.6: Gradient Delay Phantom with ideal logical gradients (green), delayed physical gradients (red), delayed logical gradients (blue) and delays $[\Delta G_x\ \Delta G_y\ \Delta G_z] = [5\ 3\ 1]$ (in k-space points) for an oblique slice orientation.

3.6.5 Volunteers

Humans without known illness and contraindications for MRI were recruited as volunteers. Each measurement was approved by the institutional review board and written informed consent was obtained from each subject before MRI.

Chapter 4

Gradient Delay Correction

Gradient delays are the temporal deviations of the actual gradients from the ideal gradients. Gradient delays are common in MRI acquisition and produce artifacts degrading the image quality. Possible causes include eddy currents in the MRI coils [79] (main bore, gradient and shim coils and RF coils) and timing errors caused by system imperfections [80]. However, all these effects can be modeled as gradient delays [77] and gradient amplitude alterations. The delayed gradient waveform is shifted by a time delay t_d and distorted in the amplitude with respect to the ideal or intended gradient waveform. The shift of the gradient waveform leads to a shifted k-space trajectory (see figure 4.1), which is in general not a problem for Cartesian imaging unless multi-echo sequences like EPI are considered [80]. For non-Cartesian imaging the trajectory shift poses a major problem [77, 81].

Modern MRI systems are equipped with two main systems in order to prevent gradient delays [41]. The first protection mechanism are shielding coils, which produce an additional field opposed to the main coil and reduce the field outside of these two coils, preventing eddy currents in other conducting structures. The second protection mechanism is the gradient waveform preemphasis. The gradient waveform is distorted prior to the input to the gradient coil, giving an outputted gradient waveform which is closer to the ideal waveform. Calculating the preemphasized waveform requires accurate knowledge of the eddy currents (magnitude and decay time) and is generated by adding a high-pass filter to the gradient amplifier input [41]. These two main systems reduce the shifts in the k-space trajectory largely but are not able to correct the shifts completely [82] and therefore trajectory or gradient delay corrections before the reconstruction must be applied in radial imaging.

The gradient delay correction using three almost antiparallel asymmetric echoes acquired in real-time phase-contrast flow MRI, as presented in this chapter, has been published by the author [12].

The chapter starts with a theory section for the gradient delay of radial trajectories as developed by Peters [77]. The theory section explains in detail the logical gradient delay estimation from Block and Uecker [11] as well as the newly developed physical gradient delay estimation. Tolerance to radial and azimuthal undersampling and noise based on a numerical gradient delay phantom is evaluated and presented in the results section. The influence of motion, temporal changes of the gradient delays and consequences for multiple echo measurements are presented. The chapter closes with a discussion of the results and a conclusion.

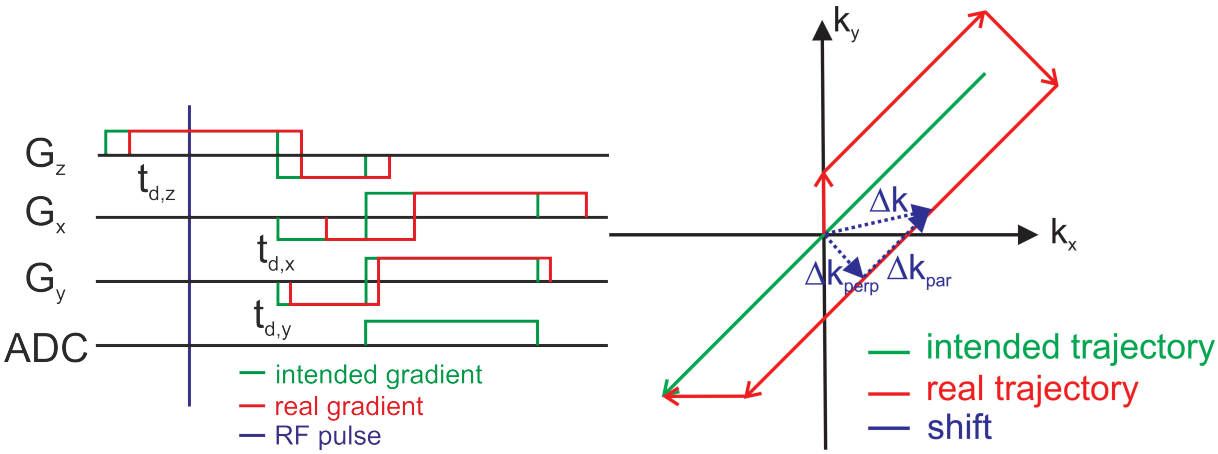

(a) Sequence gradient delay (b) Delayed trajectory

Figure 4.1: Sequence gradient delays for a single spoke from a slice perpendicular to the z-axis and the corresponding trajectory.

4.1 Theory and Results

4.1.1 Radial Gradient Delay Model

According to Peters [77] the radial gradient delay in the logical coordinate system is

$$G_{\log}^{\text{del}} = R^T T[RG_{\log}] \tag{4.1}$$

with the ideal gradients $G_{\log}$, the rotation matrix R and its transposed R^T defined by the slice orientation and the time delay operator T. The error between the ideal and delayed trajectory is calculated as the difference between the ideal and delayed trajectory.

$$\Delta k(\tau) = \frac{\gamma}{2\pi}\int_0^\tau G_{\log}^{\text{del}}(t)dt - \frac{\gamma}{2\pi}\int_0^\tau G_{\log}(t)dt \tag{4.2}$$

The shifts Δk of the delayed trajectory with respect to the ideal trajectory in the logical coordinate system are in terms of perpendicular, parallel and z-shift

$$\Delta k_{\parallel}(\theta) = G_{\text{read}}\frac{\gamma}{2\pi}\left[\cos^2(\theta)t_{g1} + \sin^2(\theta)t_{g2} + 2\cos(\theta)\sin(\theta)t_{g3}\right] - G_{\text{slice}}\frac{\gamma}{2\pi}\left[\cos(\theta)t_{g4} + \sin(\theta)t_{g5}\right] \tag{4.3}$$

$$\Delta k_{\perp}(\theta) = G_{\text{read}}\frac{\gamma}{2\pi}\left[\cos^2(\theta)t_{g3} - \sin^2(\theta)t_{g3} + \cos(\theta)\sin(\theta)t_{g6}\right] - G_{\text{slice}}\frac{\gamma}{2\pi}\left[\cos(\theta)t_{g5} - \sin(\theta)t_{g4}\right] \tag{4.4}$$

$$\Delta k_3(\theta) = G_{\text{read}}\frac{\gamma}{2\pi}\left[\cos(\theta)t_{g1} + \sin(\theta)t_{g3}\right] - G_{\text{slice}}\frac{\gamma}{2\pi}\left[t_{g7}\right] \tag{4.5}$$

with the spokes angle θ, the read gradient G_{read}, the slice gradient G_{slice} and the global delays t_{g1}, ..., t_{g7}.

$$t_{g1} = t_x R_{11}^2 + t_y R_{21}^2 + t_z R_{31}^2 \tag{4.6}$$
$$t_{g2} = t_x R_{12}^2 + t_y R_{22}^2 + t_z R_{32}^2 \tag{4.7}$$
$$t_{g3} = t_x R_{11} R_{12} + t_y R_{22} R_{21} + t_z R_{32} R_{31} \tag{4.8}$$
$$t_{g4} = t_x R_{11} R_{13} + t_y R_{21} R_{23} + t_z R_{31} R_{33} \tag{4.9}$$
$$t_{g5} = t_x R_{12} R_{13} + t_y R_{22} R_{23} + t_z R_{32} R_{33} \tag{4.10}$$
$$t_{g6} = t_x R_{12}^2 + t_y R_{22}^2 + t_z R_{32}^2 - t_x R_{11}^2 - t_y R_{21}^2 - t_z R_{31}^2 \tag{4.11}$$
$$t_{g7} = t_x R_{13}^2 + t_y R_{23}^2 + t_z R_{33}^2 \tag{4.12}$$

For an exact derivation of these shifts see A.1.

4.1.2 Two-Spokes Estimation

Block and Uecker presented a simple method for the gradient delay estimation parallel to the spoke as given in equation 4.3 [11]. The antiparallel spokes must be inverted to generate consistent data, because the antiparallel spoke is in reverse order to reference spoke, see figure 4.2.

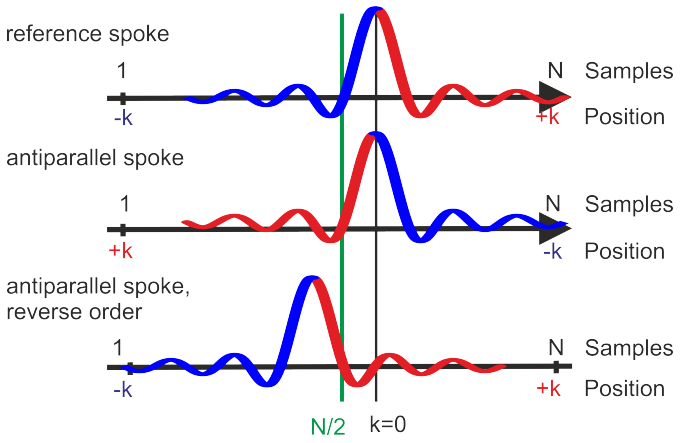

Figure 4.2: Illustration for the generation of data consistency by flipping the second, or the almost antiparallel spoke.

The shift between two antiparallel measured spokes is calculated from their cross correlation, which gives an accuracy of integral sampling points. However, using the translation property of the Fourier transform, subpixel accurate shifts from the phase can be calculated. The Fourier transform of the correlation $C(S_{\theta_1}, S_{\theta_2})$ between the spoke S_{θ_1} with shift α_1 from the reference spoke S_0 and the antiparallel spoke S_{θ_2} with shift α_2 is called g and is:

$$g[k] = \omega^{(\alpha_1+\alpha_2)k} \mathcal{F}[S_0][k] \overline{\mathcal{F}[S_0][k]} \tag{4.13}$$

with the unit root ω^{jk} as used for the discrete Fourier transform. In this simple example the phase of the g-function depends only on the shift of the spokes. The phase of the g-function is fitted by a weighted fit to a linear function without offset $f(k) = mk$ and from the slope m and the definition of ω^{ik} the shift is extracted.

$$\text{Shift} = \alpha_1 + \alpha_2 = -\frac{mN}{2\pi} \tag{4.14}$$

The shift estimation is even in the presence of noise very exact as demonstrated in figure 4.3. The calculation of this shift can be done for multiple spokes at different angles. The parallel shift of two antiparallel spokes is:

$$\left(\Delta k_{\parallel}(\theta) + \Delta k_{\parallel}(\theta+\pi)\right) = 2G_{\text{Read}}\frac{\gamma}{2\pi}\left[\cos^2(\theta)t_{g1} + \sin^2(\theta)t_{g2} + 2\cos(\theta)\sin(\theta)t_{g3}\right] \tag{4.15}$$

Equation 4.15 shows that the three global delays t_{g1}, ..., t_{g3} influence the result of the gradient delay estimation between two antiparallel spokes. In figure 4.3 the excellent performance of the shift estimation even in the presence of noise is demonstrated.

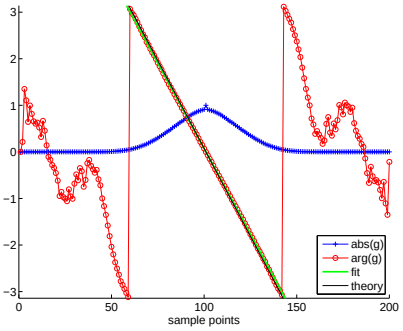

Figure 4.3: Magnitude, phase and fit to the phase of the g-function from two antiparallel spokes with different noise levels. The magnitude has been scaled to 1.

4.1.3 Three-Spokes Estimation

In [11] an extension to the case where exactly antiparallel spokes are not available is mentioned. This extension is explained here in more detail.

Figure 4.4: Reference spoke and its nearest neighbor spokes used for estimation of the gradient delay.

Considering three spokes for the shift estimation, then two almost antiparallel spokes S_{θ_1} and S_{θ_2} at angles θ_1 and θ_2 which encompass the reference spoke S_θ at angle θ as illustrated in figure 4.4 are used. The Fourier transforms of the cross correlations $C(S_\theta, S_{\theta_1})[k]$ and $C(S_\theta, S_{\theta_2})[k]$ are calculated and added subsequently, yielding with some approximations the following shift

$$\Delta k_{\text{theory}} = 4\left(t_{g1}\cos^2\theta + t_{g2}\sin^2\theta + 2t_{g3}\sin\theta\cos\theta\right) \tag{4.16}$$

Equation 4.16 is the theoretical model, which the estimated shift from three spokes follows and allows to fit the three global delays t_{g1}, t_{g2}, t_{g3} from the estimated shifts of all spokes.
However, during the previous calculations two weaknesses of the presented method appeared: first the angular separation between the reference spoke and the two almost antiparallel spokes must be small. And second, it was assumed that all, the shifted reference and the shifted almost antiparallel spokes have the exact same shape determined by S_0, which is in general not true. For the general case the g-function is

$$g[k] = \mathcal{F}[S_0][k]\overline{\mathcal{F}[S_{\theta+1}][k]}\left[\omega^{(\alpha+\alpha_1)k}\right] + \mathcal{F}[S_0][k]\overline{\mathcal{F}[S_{\theta+2}][k]}\left[\omega^{(\alpha+\alpha_2)k}\right] \tag{4.17}$$

which does not allow a straight forward calculation of the shift between the spokes. However, if the angular separation between the spokes is small, simulations show that the shift can be estimated correctly. For the simulation, a reference spoke at angle $\theta = 0$ and two antiparallel spokes S_{θ_1} and S_{θ_2} with an angular difference to the reference spoke ranging from $0 - 90°$ were selected from the numerical gradient delay phantom. The result is shown in figure 4.5, where the change of the estimated parallel gradient delay depending on the angular separation to the reference spokes is plotted.

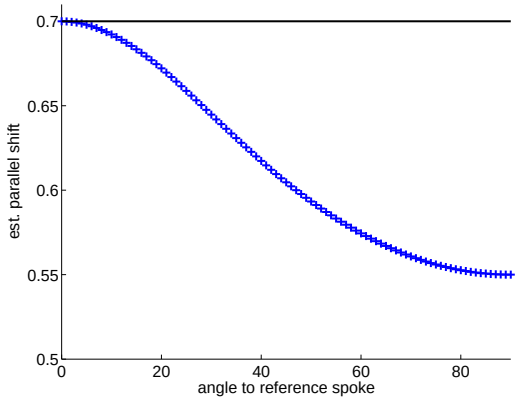

Figure 4.5: Dependence of the parallel shift estimation on the angular separation. Blue crosses represent the estimated delays at these angle deviations from the reference spoke and the black line is the reference.

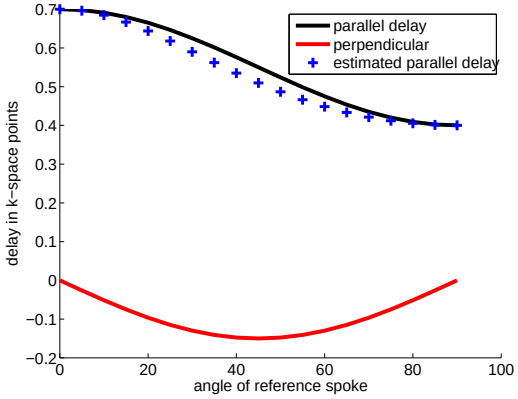

Figure 4.6: Influence of the perpendicular shift to the estimation of the parallel shift.

4.1.4 Physical Gradient Delay Estimation

The parallel shift is not enough to fully describe the gradient delay. In figure 4.6 the shift is estimated from a noiseless phantom using three spokes without angular separation. Clearly for the x- and y-axis the correct parallel delay is estimated, but if the perpendicular shift increases, the parallel shift cannot be longer estimated accurately. However, if the slice orientation with respect to the physical coordinate system is known, then the physical gradient delays can be calculated by using only the first three equations from 4.6 - 4.12, rewritten in matrix formulation.

$$\begin{bmatrix} t_{g1} \\ t_{g2} \\ t_{g3} \end{bmatrix} = \begin{bmatrix} R_{11}^2 & R_{21}^2 & R_{31}^2 \\ R_{12}^2 & R_{22}^2 & R_{23}^2 \\ R_{11}R_{12} & R_{22}R_{21} & R_{32}R_{31} \end{bmatrix} \qquad \begin{bmatrix} t_x \\ t_y \\ t_z \end{bmatrix} = A \qquad \begin{bmatrix} t_x \\ t_y \\ t_z \end{bmatrix} \tag{4.18}$$

By inverting A, the physical delays t_x, t_y, t_z can be calculated, allowing the calculation of all global delays using equations 4.6 - 4.12.

$$\begin{bmatrix} t_x \\ t_y \\ t_z \end{bmatrix} = \begin{bmatrix} R_{11}^2 & R_{21}^2 & R_{31}^2 \\ R_{12}^2 & R_{22}^2 & R_{23}^2 \\ R_{11}R_{12} & R_{22}R_{21} & R_{32}R_{31} \end{bmatrix}^{-1} \qquad \begin{bmatrix} t_{g1} \\ t_{g2} \\ t_{g3} \end{bmatrix} = A^{-1} \qquad \begin{bmatrix} t_{g1} \\ t_{g2} \\ t_{g3} \end{bmatrix} \tag{4.19}$$

To further improve the estimation of the physical delays, the perpendicular shift is calculated and then the parallel shift is refitted with a weighting function from the perpendicular shift. The used weighting function is

$$f_w(\Delta k_\perp) = \exp\left\{ -\left(s \frac{|\Delta k_\perp - \Delta k_{\perp,\min}|}{|\Delta k_{\perp,\max} - \Delta k_{\perp,\min}|} \right)^p \right\} \tag{4.20}$$

and produces a weighting between zero and one and the two parameters s and p determine the weighting of the perpendicular delay. The behavior of the weighting function is presented in figure 4.7 based on simulations of the gradient delay phantom. The parameters for the weighting function can be selected from figure 4.8, e.g. $s = 1.5$ and $p = 5$. The trajectories calculated with the physical gradient delay correction and the parallel gradient delay correction are shown in figure 4.9. The physical gradient delay correction estimates a trajectory almost identical to the ideal trajectory, whereas the parallel gradient delay correction estimates a trajectory with minor deviations.

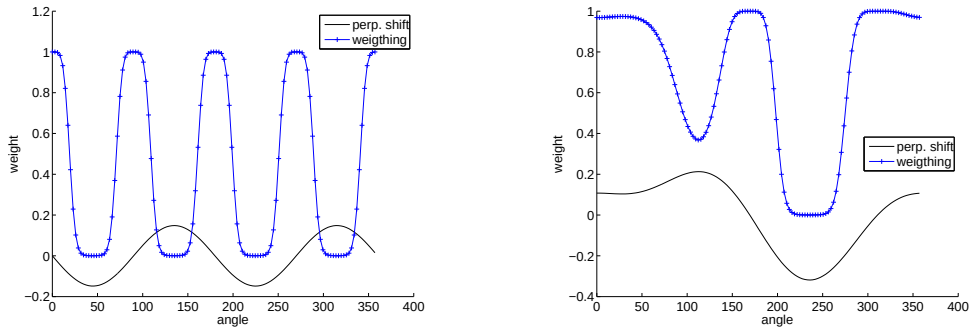

(a) axial slice orientation (b) oblique slice orientation

Figure 4.7: Weighting function for an axial and oblique slice orientation with parameters $s = 1.5$ and $p = 5$.

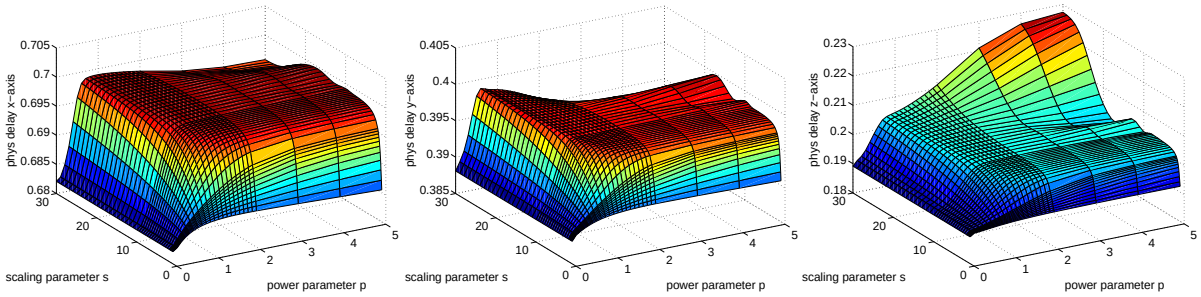

(a) x-axis physical delay (b) y-axis physical delay (c) z-axis physical delay

Figure 4.8: Estimated physical gradient delay values depending on the weighting function parameter s and p. Reference values are $[\Delta G_x\ \Delta G_y\ \Delta G_z] = [0.7\ 0.4\ 0.2]$

4.1.5 g-Function Calculation

The g-function can be calculated using either the complex values, magnitude values or squared magnitude values of the spoke. With the complex values of the spokes, the real and imaginary parts are separately correlated. This might be problematic because the phase influences the real and imaginary parts and in MRI not only the spatial location but many other effects may be encoded unintentionally into the phase.

The different g-function calculations were compared based on data generated from the numerical gradient delay phantom.

A comparison of the different calculation methods is presented in figure 4.10 and table 4.1 for the x-y-slice and in figure 4.11 and table 4.2 for an oblique slice orientation. The complex and the

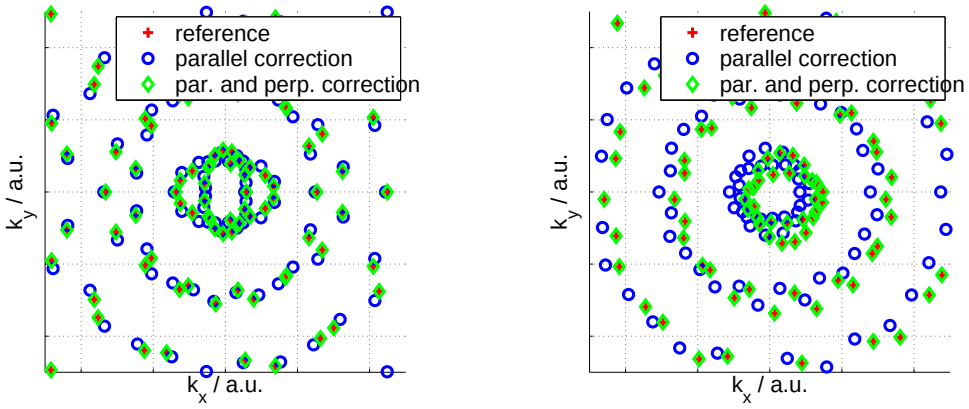

(a) axial slice orientation (b) oblique slice orientation

Figure 4.9: Trajectory deviations and possible corrections with the proposed method for an axial and oblique slice.

squared magnitude calculation accurately reproduced the input delays for both slice orientations as shown in tables 4.1 and 4.2. In the presence of noise the squared magnitude calculation is superior to the complex calculation of the g-function in terms of the reduced scattering of the individual estimated shifts per spoke, see figures 4.10, 4.11. The reduced scattering indicates that the squared magnitude estimation is more robust for higher radial undersampling factors. The exact determination of the shift for any given spoke in a slice with oblique orientation requires the knowledge of almost all global delays, however the presented shift estimation for the individual spokes is only able to estimate the first three global delays. The estimated shifts of the individual spokes follow the theoretical shift given only by the first three global delays quite accurately (red crosses in figures 4.10, 4.11) which is in case of an oblique slice orientation incorrect. The usage of the physical gradient delay estimations allows for calculation of all global delays and a correct estimation of the individual spoke shifts (red line in figures 4.10, 4.11). The estimation of the physical gradient delay of the slice selection gradient is not possible for axial slices, because the slice selection gradient is not used during the data acquisition and only the first three global delays are needed.

Method	ΔG_x	ΔG_y	ΔG_z
Complex	0.713	0.442	0
Magnitude	0.597	0.354	0
Sq. Magnitude	0.713	0.387	0
Reference	0.7	0.4	0.2

Table 4.1: Physical gradient delay from the three different calculation methods for a slice in the x-y-plane.

Method	ΔG_x	ΔG_y	ΔG_z
Complex	0.732	0.403	0.167
Magnitude	-0.072	0.090	1.632
Sq. Magnitude	0.690	0.392	0.225
Reference	0.7	0.4	0.2

Table 4.2: Physical gradient delay from the three different calculation methods for an oblique slice orientation.

4.1.6 Gradient Delay Correction for Asymmetric Echoes

Asymmetric echo data is not symmetric around the echo center and contains fewer samples than a symmetric echo acquisition with the same nominal in-plane resolution. The asymmetric echo data is cropped to a reduced but symmetric echo on which the gradient delay is estimated. The

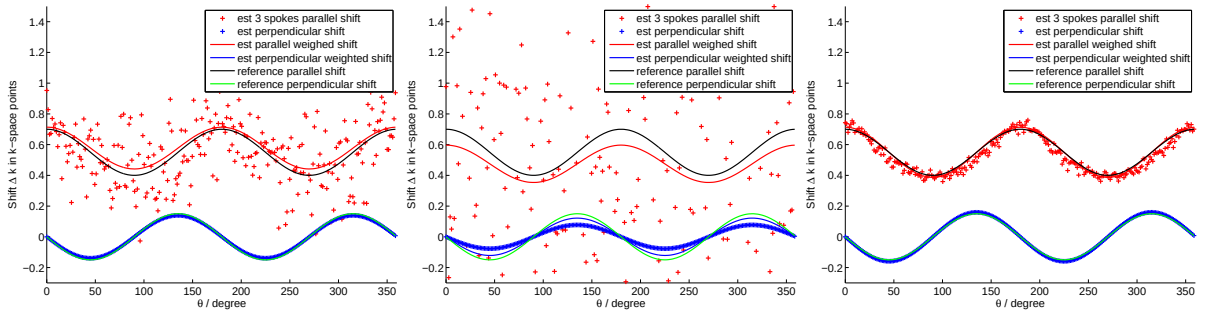

(a) complex calculation of g (b) magnitude calculation of g (c) squared magnitude calculation of g

Figure 4.10: Comparison of the shift and fits for the parallel and perpendicular delay obtained from three spokes in the presence of 10% noise with a total of 255 spokes for a slice in the x-y-plane.

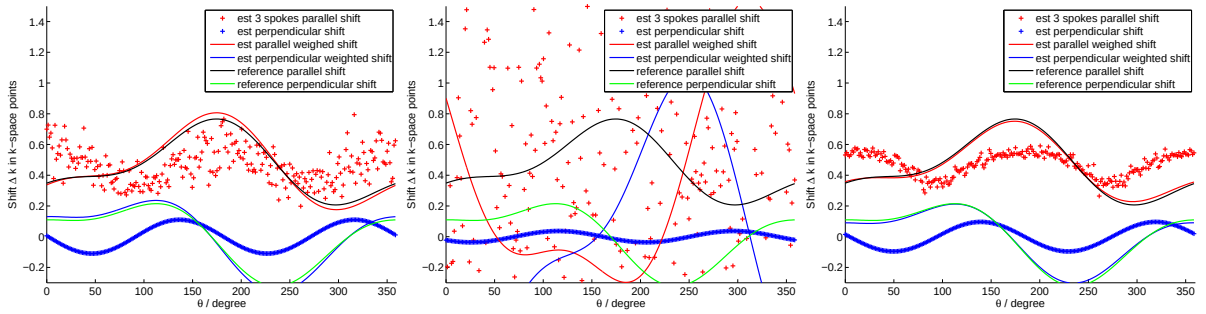

(a) complex calculation of g (b) magnitude calculation of g (c) squared magnitude calculation of g

Figure 4.11: Comparison of the shift and fits for the parallel and perpendicular delay obtained from three spokes in the presence of 10% noise with a total of 255 spokes for an oblique slice orientation.

asymmetry factor a is defined as

$$a = \frac{N_A}{2N_B} \tag{4.21}$$

with N_A and N_B the sampling points before and after the echo, with the sampling point of the echo center belonging to N_B. With this definition 50% asymmetry corresponds to a symmetric echo, while 0% represents a half-echo acquisition. The robustness with respect to reducing the number of sampling points was evaluated from the numerical gradient delay phantom. The estimation of the physical delays is very robust as demonstrated in figure 4.12. The estimated global delays from measured asymmetric data with different asymmetry factors are shown in figure 4.13. The change in the delays with increasing asymmetry is unknown and subject to further research. The quality of the reconstructed images improved with the application of the gradient delay correction, see figure 4.14. The arising spurious signal intensity outside the object was successfully removed.

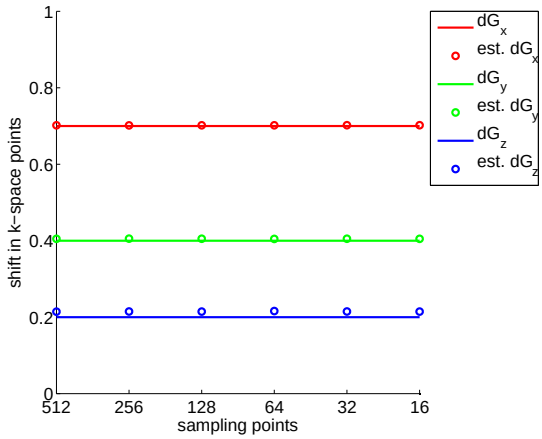

Figure 4.12: Gradient delay estimation with different number of sampling points. The estimation is very stable, even for a low number of sampling points. The k-space data consisted of 75 spokes with a noise level of 0.1%.

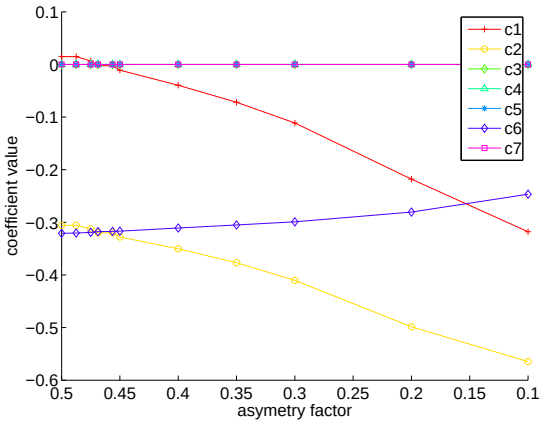

Figure 4.13: Estimation of the global delay for different asymmetric sampled echoes.

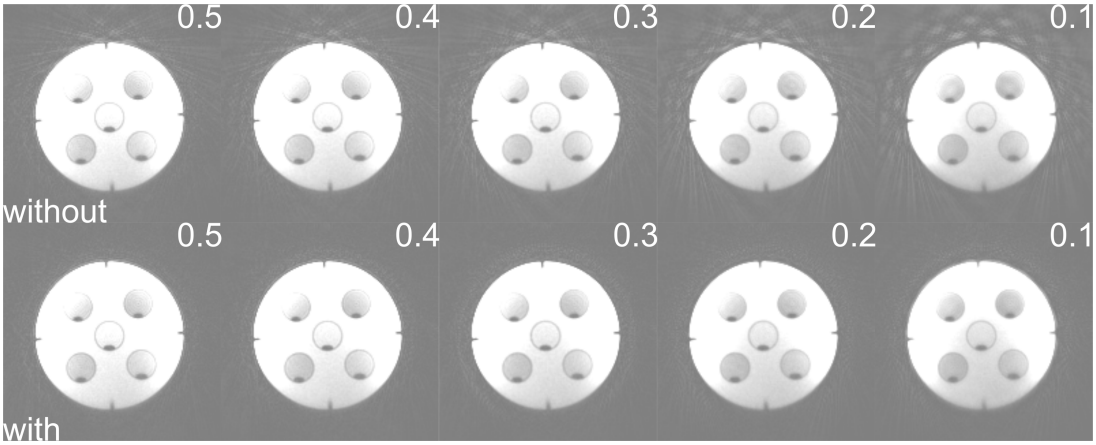

Figure 4.14: Effect of the gradient delay correction on the reconstruction for different asymmetry factors (upper right corner). The top row shows image reconstructions without any gradient delay correction and the bottom row shows the image reconstructions with gradient delay correction.

4.1.7 Simulations

Simulations were performed to evaluate the influence of noise and effects of azimuthal undersampling on the gradient delay phantom In figure 4.15 the gradient delay estimation for different noise levels and number of spokes is shown. The gradient delay estimation is very robust with respect to noise and degree of undersampling, i.e. the number of spokes available. In figure 4.16 reconstructions of the gradient delay phantom with different gradient delay correction methods are presented. The full gradient delay correction is close to the perfect gradient delay correction.

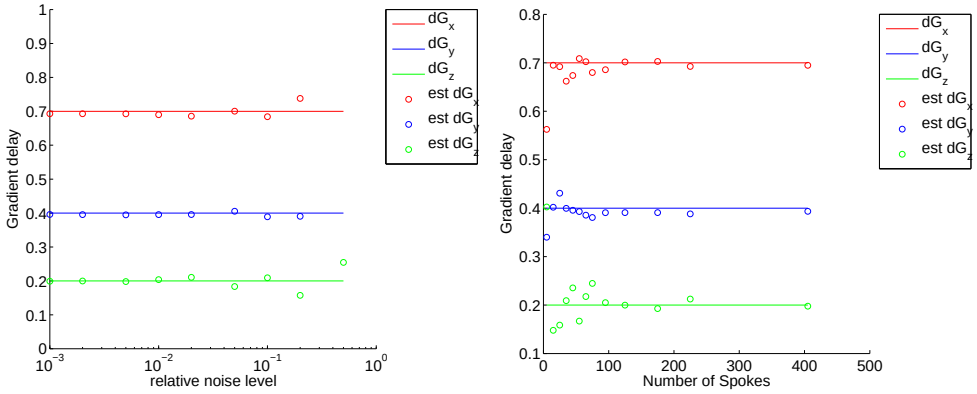

(a) 75 Spokes (b) 5% noise level

Figure 4.15: Estimated Physical Gradient Delay values for 75 spokes and different noise levels (4.15a) and with respect to the available number of spokes and for noise level of 5% (4.15b).

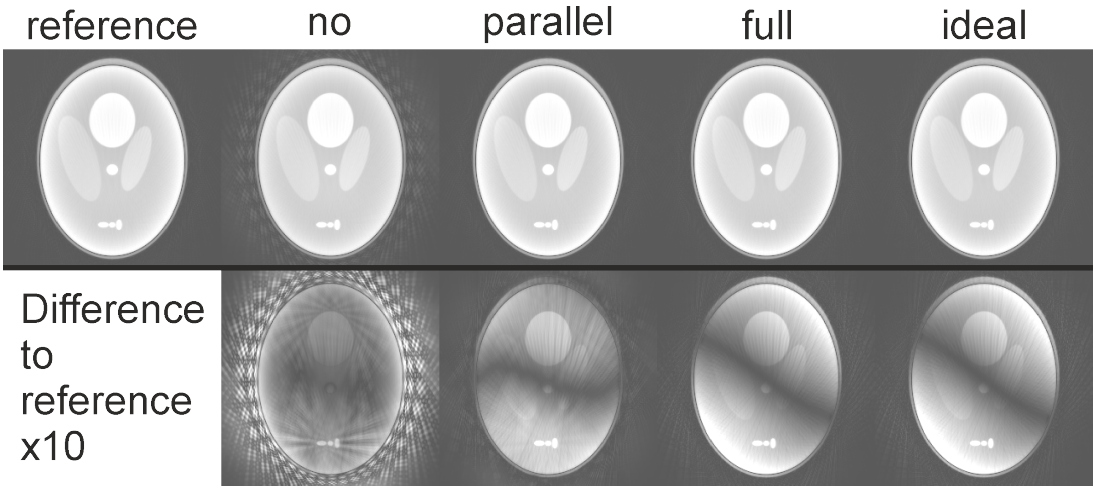

Figure 4.16: NLINV image reconstruction with different gradient delay corrections from data of the gradient delay phantom with 19 spokes, no noise. Top row shows the reconstructed data for different correction methods (from left to right: reference, no correction, parallel correction, parallel and perpendicular correction, ideal correction). In the bottom row the difference to the reference for the respective correction method is displayed.

4.1.8 Time Evolution

Temperature changes in the gradient coils may causes the gradient delay to vary over time [83]. Therefore, measurement of 60 seconds duration of an axial slice was performed to investigate gradient delay variation over time. The results for the physical gradient delays are shown in figure 4.17, but due to the axial slice orientation the z-axis delay cannot be estimated. However, the z-axis delay is not expected to vary significantly stronger than the x- and y-gradient delays [84]. The relative change over the time is for the x-axis 11% and 4% for the y-axis, which seem quite a lot but the absolute change is one order of magnitude smaller than the delay. Due to the small absolute changes in the gradient delay, it is sufficient to estimate the gradient delay at the beginning of the measurement and the same correction to all succeeding frames, at least for the next 60 seconds.

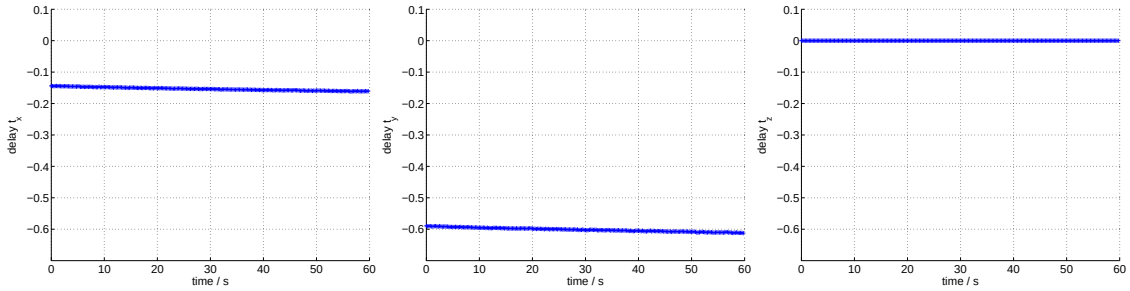

(a) physical delay t_x (b) physical delay t_y (c) physical delay t_z

Figure 4.17: Estimated physical delays over a time of 60 seconds. The z-delay cannot be estimated because the slice is axial oriented.

4.1.9 Multi-Echo Measurements

Mutli-echo measurements were acquired to investigate the possible differences of the gradient delays between succeeding echoes. Applying the gradient delay estimation to different echoes yields a different gradient delay between the odd and even echoes as summarized table 4.3. The different gradient delays between odd and even echoes generates a need for an individual gradient delay correction for each echo. The individual gradient delay correction does indeed improve the even echoes as demonstrated in figure 4.18. The *identical* mutli-echo gradient delay correction uses the estimated delays from the first echo for all echoes while with the *individual* correction each echo is individually corrected. Both methods take advantage of the complementary turns for gradient delay estimation.

Echo	t_x	t_y	t_z
1	-0.14	-0.70	0
2	-0.06	0.42	0
3	-0.13	-0.70	0
4	-0.08	0.40	0
5	-0.18	-0.73	0

Table 4.3: Estimated physical gradient from an axial slice.

With increased undersampling the gradient delay estimation becomes more difficult, because fewer spokes are available for the estimation as well as the angular separation between the spokes increases. In figure 4.18 the effect of undersampling for the gradient delay estimation with odd and even echoes is presented, the number in the upper right represents the spokes per turn. NLINV reconstructions with 41 spokes and more spokes show no artifacts independently of the used multi-echo gradient delay correction method. Image reconstructions with the identical gradient delay correction method and fewer then 21 spokes show artefacts for the even echoes, which are successfully reduced with the individual gradient delay correction. Using only 7 spokes per turn for image reconstruction and 35 spoke for gradient delay estimation is at the lower limit of what is possible and challenging to both image reconstruction and gradient delay estimation. The difference of the gradient delay between the odd and even echoes does not have physical reason but is caused by the different trajectories between the echoes. The reconstruction however, uses the same trajectory for odd and even echoes, which leads to differences in the estimated gradient delay values. The inclusion of an individual gradient delay correction is a possible way to compensate for the wrong trajectory used in the reconstruction for the even echoes. Because

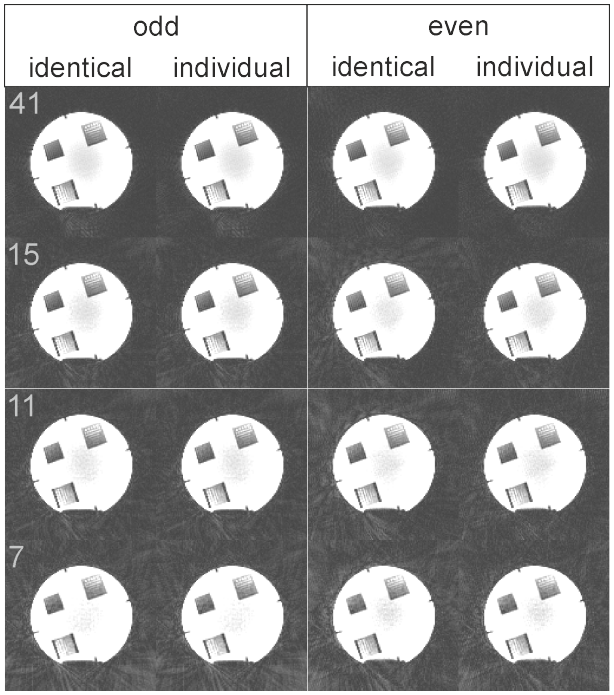

Figure 4.18: Comparison of image reconstructions with different gradient delay correction methods for representative odd and even echoes. The upper left number represents the number of spokes from which the image is reconstructed. Note the increasing streaking artifacts for the even echo.

the physical gradient delays should not change between the echoes, the trajectory for even echoes should be corrected in the reconstruction.

4.1.10 Motion

Motion influences the estimation of the gradient delay, as displayed in figure 4.19 where the delay is estimated from the individual frames of a moving object. The change of the gradient delays is caused by the correlation of different projections, breaking the assumption that the spokes are alike. Similar to the angular separation effect small differences are not a problem, but large differences significantly alter the gradient delay estimation and produce image artifacts. However, the induced changes in the gradient delay values do not reflect an actual change of the gradient delay. The changes are merely a motion artifact. In order to obtain the best possible image quality, the gradient delay should be estimated from data containing enough spokes and only negligible motion.

4.2 Discussion

In this chapter the gradient delay model [77] with respect to the parallel, perpendicular and z-shift was presented. Based on the estimation of the parallel delay [11] it was shown that the physical delays and all global delays can be calculated. The improved accuracy of the trajectory calculation, as well as the improvement in image quality was demonstrated in a numerical gradient delay phantom and in real data. Multi-echo acquisitions have different trajectories for the odd and even echoes which is not considered during the gradient delay estimation, leading to different gradient delay values for odd and even echoes which required individual correction of each echo.

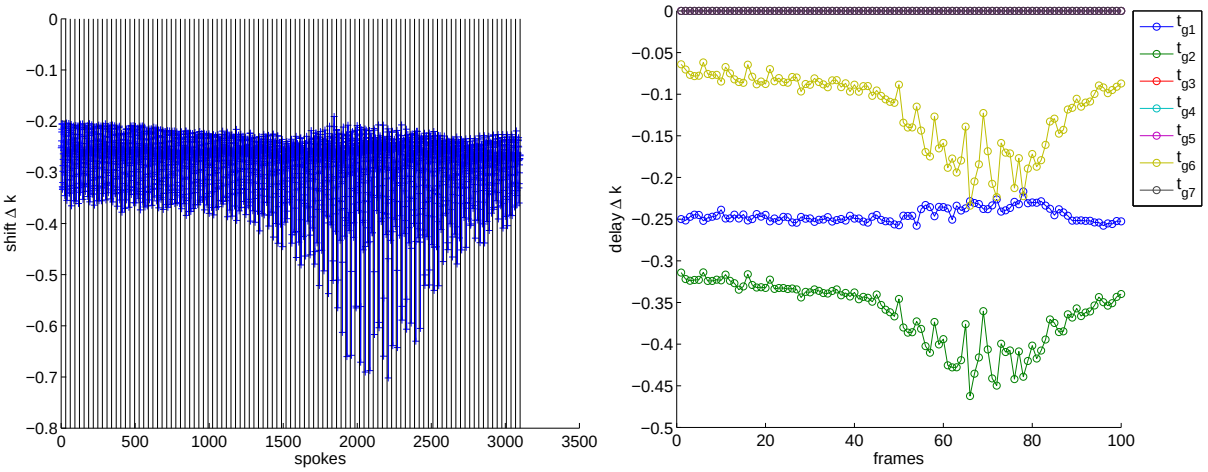

(a) shifts of individual spokes

(b) global delays

Figure 4.19: Shifts of the spokes and the estimated global delays for a knee measurement where the knee moves. The global delays are estimated from the spokes of each frame. The black lines mark the beginning of a new frame.

Also the effects of undersampling along the radial and azimuthal direction, of asymmetric echo sampling, of noise and of motion were investigated. The presented method is very robust with respect to radial and azimuthal undersampling, asymmetric echo sampling and noise. Motion during the data acquisition interferes with the gradient delay estimation and possibly wrong values are estimated. The influence of the perpendicular shift is negligible for an angular spacing of spokes of up to 5° and increases afterwards.

The presented method is computationally very efficient but calculation of physical delays requires knowledge about the slice orientation. Other trajectory correction methods estimate the physical delays from calibration measurements [84, 85] or measure the trajectory directly [86–89]. While calibration measurements and trajectory measurements can probably estimate the physical gradient delays as well as the trajectory with greater accuracy than the presented method, an extra measurement is usually not desired. Recently, an iterative gradient delay correction was proposed [90] which shifts the data from individual projections until all inconsistencies are removed. The iterative gradient delay correction is effective but computationally intense. Ianni et al. [91] included the gradient delay into the model of a model-based reconstructions and obtained improved images, at the expense of long computation time.

The temporal constant gradient delay is estimated from initial data and used for trajectory correction throughout the measurement. Such initial data could be replaced by measurements along the physical gradient axes from which each physical gradient delay may be estimated directly [11].

Apart from the displayed improvements in image quality by reducing streaking artifacts, a correct gradient delay estimation becomes necessary for quantitative and off-axis non-Cartesian measurements [92–95].

With only some minor technical changes the presented gradient delay correction may be applied to radial echo-planar imaging as presented by Silva [96]. However, care has to be taken that the shape of the correlated echoes is not to different, preventing erroneous calculation.

4.3 Conclusion

The presented method allows for a gradient delay correction for arbitrary slice orientations almost independent of radial and azimuthal sampling. This improves the image quality buy reduction of artefacts. The proposed method also behaves robustly in the presence of noise and little motion and can be applied to multiple echoes.

Chapter 5

Real-Time T_2^* Mapping

In gradient echo imaging the transverse magnetization decays with T_2^*, which depends on the tissue specific parameter T_2 and the magnetic field inhomogeneity. Because T_2^* depends on the magnetic field inhomogeneity, T_2-weighted imaging is more widespread than T_2^* imaging. However, T_2-weighted imaging requires longer acquisition times for single frames.

Similar to T_2, T_2^* represents normal or abnormal microstrucures [13–15] and already serves as a biomarker for liver iron concentration to guide chelation therapy in transfusion dependent patients [19, 20]. Moreover, T_2^* provides access to the relative oxygenation of blood [16, 17, 97–99] and in consequence to the perfusion of the tissue, which is used for functional MRI [18].

Myocardial perfusion measurements have been tried for rabbits in vivo and ex vivo using T_2 changes and/or the BOLD effect [99–101]. Previous attempts to measure myocardial perfusion in humans determined T_2^* or the BOLD effect [102, 103]. Wendland was able to detect changes in myocardial signal during breath hold [104], suggesting a dependence of myocardial signal intensity on the oxygenation level of blood. Li determined the T_2^* of arterial and venous blood to be 199 ± 8 ms and 108 ± 6 ms, respectively [97, 98]. However, the oxygenation of blood is not the only parameter that may determine cardiac perfusion. The vessel volume changes due to the contraction of the heart as Judd and Levy found from arrested and dissected hearts during diastole and systole [105].

Cardiac perfusion measurements using real-time T_2^* mapping has not yet been tried, because it poses major difficulties for data acquisition and image reconstruction. A sufficient number of echoes to estimate T_2^* must be acquired in short time, so that the cardiac cycle is sampled accurately. Both is possible with a radial FLASH sequence with extreme undersampling in combination with an advanced image reconstruction method such as NLINV.

The first section of the chapter presents possible decay and fitting methods and discusses their suitability for real-time T_2^* mapping. Simulations are performed for a T_2^* decay model to evaluate the precision and accuracy of the fit. In the 'Motion Phantom' section, single-echo and multi-echo measurements are presented and discussed. The following sections present the results of the real-time T_2^* mapping of the human heart and possible interpretations.

5.1 T_2^* Models and Fitting Methods

Depending on the imaged material and its structure, not only a single but multiple decay components appear within a voxel [106–109]. However, such multi-exponential decays are usually approximated by a single exponential decay, which is justified, because if the multiple decay parameters are similar, a weighted average with an effective T_2^* decay is fitted. Additionally, if only few echoes are acquired, the estimation of multiple parameters using non-linear fitting becomes increasingly difficult. The common T_2^* decay fitting models are [48, 49]:

- Simple Exponential Model (S-Exp):

$$S(t) = S_0 \exp\{-\frac{1}{T_2^*}t\} \tag{5.1}$$

with the initial signal intensity S_0 at time $t = 0$ and the decay time T_2^* .

- Exponential model with constant (C-Exp):

$$S(t) = S_0 \exp\{-\frac{1}{T_2^*}t\} + C \tag{5.2}$$

with the same definitions as for the S-Exp model plus the offset C.

- Bi-exponential model (Bi-Exp):

$$S(t) = S_{0,1} \exp\{-\frac{1}{T_{2,1}^*}t\} + S_{0,2} \exp\{-\frac{1}{T_{2,2}^*}t\} \tag{5.3}$$

with the two signal intensities $S_{0,1}$ and $S_{0,2}$ at time $t = 0$ and the two decay parameters $T_{2,1}^*$ and $T_{2,2}^*$. For fitting the myocardium, 90% percent of the initial signal intensity is accounted to the myocardium ($S_{0,1} = 0.9S_0$) and 10% to the blood in the myocardium ($S_{0,2} = 0.1S_0$) due to the vascularization of the heart [104].

While nonlinear fitting algorithms are capable to fit all of the presented fitting models, the S-Exp model and after subtraction of C the C-Exp model can be linearized and fitted with the linear least-squares routine presented in chapter 3.5.3. The bi-exponential model can only be fitted non-linearly and the fit resulted in inconclusive or unrealistic results given the acquired data. Therefore and due to the long duration of the non-linear fitting procedure this model was discarded. Fitting times for a complete frame are below 0.2 seconds using the least squares fit.

T_2^* results with high precision and accuracy are obtained by calculating the squared magnitude of each measurement point, subtracting the mean noise level from each measurement point and fit the data with a nonlinear mono-exponential algorithm with initial values from a linear fit [110]. However, the long calculation period of the nonlinear fitting routine favors the linear fitting routine for large data sets as measured in real-time T_2^* mapping. The linear fitting results correlate with the nonlinear fitting results [111, 112] yielding, however, reduced precision and accuracy [110].

Advantages and disadvantages between pixelwise or ROI analyses have been investigated, yielding a strong correlation between ROI fitting and pixelwise fitting [111, 113]. However, the pixel-based fitting approach produces less variation than ROI fitting, because the mono-exponential model matches better to pixelwise data.

In conclusion, for real-time T_2^* mapping the linear least-squares fitting approach must be used. However, if the analysis is restricted to a ROI, the nonlinear fitting approach may be applicable.

5.2 Simulations

Simulations to test the accuracy and precision of the least-squares T_2^* fit in the presence of noise and different echo train lengths were performed. Data were simulated using the S-Exp model with $S_0 = 1$ and T_2^* ranging from 10-60 ms. Gaussian noise with zero mean and peak amplitudes of 0.05 (5% noise level) and 0.1 (10% noise level) was added to the data. The signal decay was simulated for $N_{\text{Echo}} \in \{5, 9, 13, 19, 25\}$ echoes with an echo spacing of $\Delta\text{TE} = 0.96\,\text{ms}$. The simulation

last TE / ms	Number TEs	T_2^* reference / ms	T_2^* fit with 10% noise / ms	T_2^* fit with 5% noise / ms
5.20	5	10	10.2 ± 1.5	10.1 ± 0.7
5.20	5	20	21.2 ± 5.3	20.2 ± 2.4
5.20	5	30	33.9 ± 14.8	30.8 ± 5.1
5.20	5	40	48.1 ± 146.8	41.8 ± 9.9
5.20	5	50	59.1 ± 774.5	54.2 ± 17.3
5.20	5	60	199.6 ± 4530.0	68.4 ± 28.8
9.04	9	10	10.0 ± 1.0	10.0 ± 0.4
9.04	9	20	20.2 ± 3.0	20.0 ± 1.0
9.04	9	30	30.6 ± 4.4	30.1 ± 2.1
9.04	9	40	41.1 ± 7.5	40.3 ± 3.7
9.04	9	50	52.3 ± 13.3	50.5 ± 5.7
9.04	9	60	65.0 ± 24.9	51.3 ± 8.2
18.64	19	10	9.9 ± 0.5	10.0 ± 0.3
18.64	19	20	19.9 ± 1.0	20.0 ± 0.5
18.64	19	30	30.1 ± 1.7	30.0 ± 0.9
18.64	19	40	40.1 ± 2.6	40.0 ± 1.4
18.64	19	50	50.2 ± 3.9	50.1 ± 2.0
18.64	19	60	60.7 ± 5.6	60.2 ± 2.7

Table 5.1: Simulation results for different echo train lengths fitted to decays following the S-Exp model with different reference T_2^* value and two noise levels.

was executed 1000 times for each reference T_2^* value, adding different noise for each run. Each simulated decay was fitted linearly and the average and standard deviation of the obtained T_2^* and S_0 values were calculated. The results are given in table 5.1 as mean $\pm$ standard deviation.

The results of the linear T_2^* fit are generally accurate and increase in accuracy and precision with increasing echo train length. If the last echo time $\mathrm{TE}_N > \frac{1}{3} T_{2,\mathrm{ref}}^*$ the standard deviations are below 5% and the fit is considered to be precise. The results in table 5.1 show an overestimation of T_2^* values for $\mathrm{TE}_N < T_{2,\mathrm{ref}}^*$ and an underestimation for $\mathrm{TE}_N \gtrapprox T_{2,\mathrm{ref}}^*$.

In conclusion, fitting results with $T_2^* < 3 \cdot \mathrm{TE}_N$ have an accuracy below 2 ms and precision of 5 ms, while fitting results with $T_2^* > 3 \cdot \mathrm{TE}_N$ may be accurate but are not very precise. Furthermore, the reliability of the fitted T_2^* values increases with increasing echo train length or for shorter true T_2^* values.

5.3 Motion Phantom Measurements

The motion phantom with a petri-dish of 9 cm diameter as described in section 3.6.2 is used for the measurements presented in this section.

The NLINV image reconstruction jointly estimates spin density and coil profiles [6, 7]. A quantitative comparison between two NLINV reconstructions requires the multiplication of the spin density with the coil profiles, otherwise the difference may not only be attributed to differences in the data but to differences in the image reconstruction. The multi-channel data obtained after multiplication may be combined using the root sums of squares over the channels which is SNR optimal [114]. Furthermore, the quantitative comparison between two real-time series requires removal of the physical coil weighting, which is possible with an intensity correction. The intensity correction is performed on all measurements before the data is analysed.

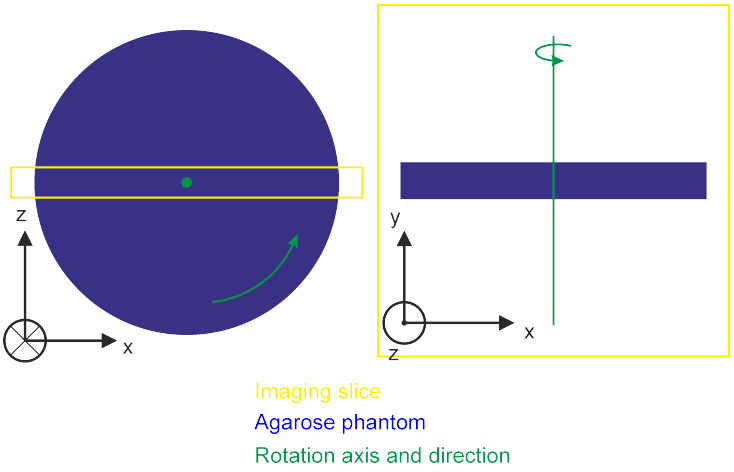

Figure 5.1: Two views of the phantom with the imaging slice.

5.3.1 Single-Echo Measurements

The experimental setup of the agarose disk in the motion phantom is sketched in figure 5.1. The imaging slice is oriented parallel to the rotation axis yielding a through plane rotation of the agarose disk. This through plane motion is analysed.

The isochromats within a radius of half the slice thickness stay inside the slice during rotation, while the other isochromats leave and re-enter the slice. This leads to the definition of two regions, the inner region $R_{\text{in}} := \{\text{Isochromats with distance to rotataion axis } \leq \text{Slice Thickness}/2\}$ and the outer region $R_{\text{out}} := \{\text{Isochromats with distance to rotation axis } > \text{Slice Thickness}/2\}$.

Temporally and spatially averaged signal intensity profiles of the agarose disk for five different velocities are displayed in figure 5.2. The measurements show a low signal intensity in the center of the profile and increasing signal intensity towards the outer parts of the disk. A comparison between the signal intensity profiles for the rotating and for the static phantom is shown in figure 5.3.

The spatial variations of the signal intensity displayed in figures 5.2 and 5.3 are caused by the competitive effects of inflow and motion dephasing of the isochromats. The isochromats move along the x- and z-direction (see figure 5.1) and dephase during the slice select gradient. A possible dephasing during the read-out gradient would be rephased with a second echo. The performed dual-echo measurements did not show such a rephasing. After the isochromats have left the slice the longitudinal magnetization recovers, producing higher signal intensity as the isochromats re-enter the slice on the other side of the rotation axis. The time an isochromat spends in the slice is given by $t_1 = \frac{s}{\omega r}$ with the slice thickness s, the rotational velocity ω and the distance from the rotation center r. The phase ϕ an isochromat acquires due to the rotational motion approximated as linear motion through the slice is for constant gradients G

$$\phi(t_1) = \frac{1}{2} G\omega r \cdot \frac{s^2}{\omega^2 r^2} = \frac{1}{2}\frac{Gs^2}{\omega r}. \tag{5.4}$$

Therefore the dephasing scales with $\propto \frac{1}{\omega r}$ and is less at the outer parts of the disk for a given rotational velocity, as demonstrated in figure 5.2. However, due to the approximation of a constant linear velocity, equation 5.4 may break down close to the rotational axis.

The signal intensity dependence of the parameters slice thickness, repetition time and flip angle was analyzed, giving consistent results, explained by inflow and dephasing. With an increased slice thickness the 'dip' increases in width since the area in which the isochromats experience no inflow is increased, see figure 5.3. A longer TR increases the incoherent steady

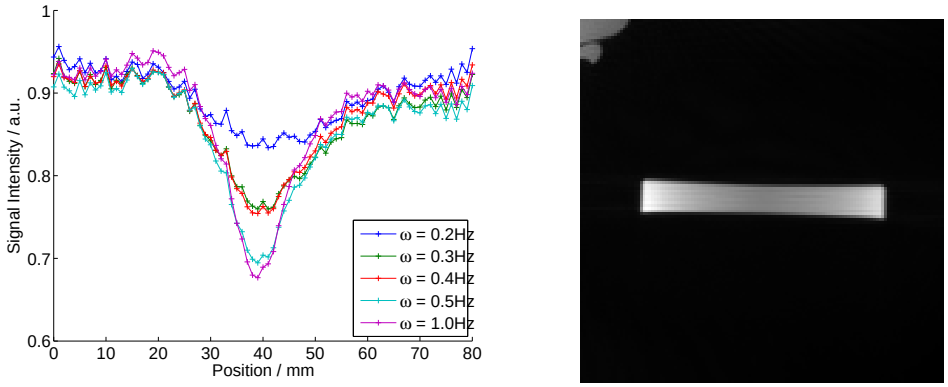

Figure 5.2: Velocity dependence of the signal intensity (left) and a representative image frame (right).

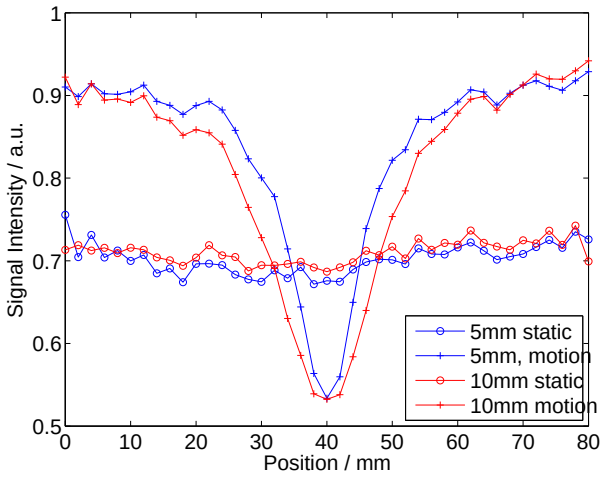

Figure 5.3: Intensity corrected column of a frame with and without rotating disk for two different slice thicknesses.

state signal, while the dephasing remains unchanged, leading to an apparent reduction of the dip in the normalized images, compare to figure 5.4. The flip angle changes the influence of the T_1-weighting of the inflow effect. Up to the Ernst angle, the signal increases, since the incoherent steady state increases, as seen in comparison with the static data, but not visible in the normalized static or dynamic data. Instead of the signal increase in the outer region, the 'dip' becomes deeper, see figure 5.5. With extremely low flip angles the T_1-weighting and therefore the inflow effect vanishes, yielding identical signal intensities for the static and dynamic case, see figure 5.5.

5.3.2 Multi-Echo Measurements

The influence of motion on multi-echo measurements was investigated with dynamic (disk is rotating) and static (disk is not rotating) measurements. Each measurement was acquired with 81 spokes per frame, to ensure that no undersampling artefacts contaminate the signal decay after image reconstruction. A measurement with slice orientation perpendicular to the y-axis, gives the T_2^* distribution inside the disk, see figure 5.6.

The asymmetry of T_2^* values along the x- (sagittal) and z-axis (transversal) is due to the inhomogeneous magnetic field. None of the tested shim versions could improve the homogeneity

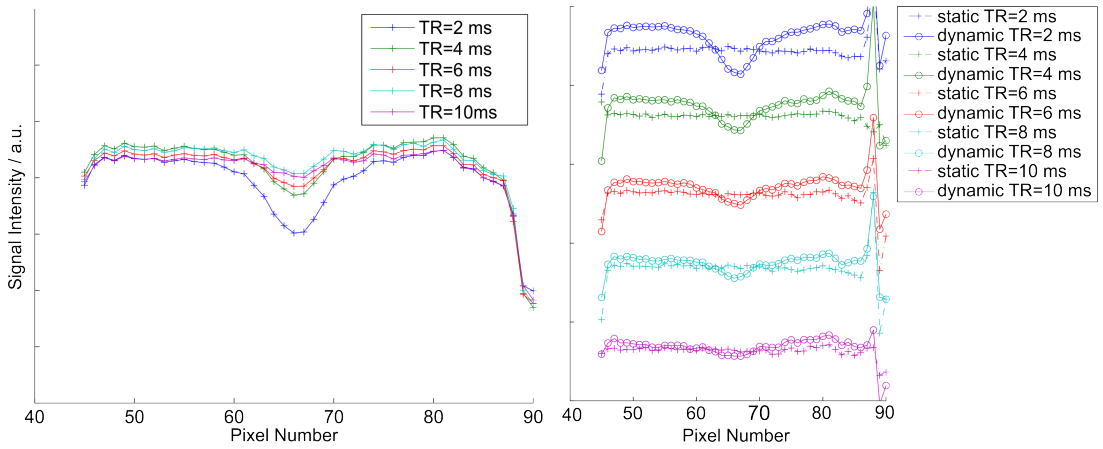

Figure 5.4: TR influence on the dip (left) in comparison to the static steady state (right).

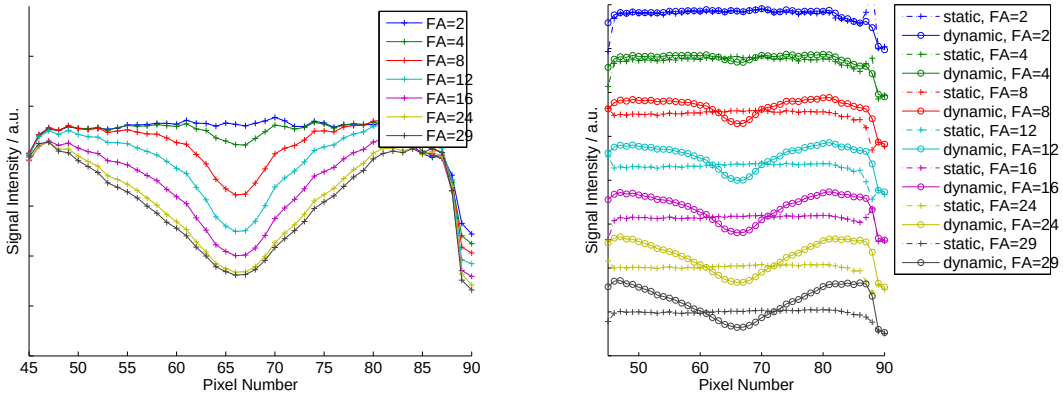

Figure 5.5: Flip angle measurements. Left are the different flip angles compared between each other and on the right side with respect to their static signal intensity.

of the magnetic field inside the disk. The T_2^* measurements of the static and rotating disk have been performed with a sagittal slice orientation (y-z-plane in figure 5.6). For each of the rotational frequencies (0.24, 0.82, 1.25 Hz) 20 frames have been acquired and the T_2^* has been estimated for each frame and subsequently averaged for better SNR. The spatial dependence of the averaged T_2^* values for each rotational velocity is shown in figure 5.7, where a shortening of T_2^* in the outer parts of the disc with increasing rotational velocity is visible. The major reduction of T_2^* is caused by the motion of the isochromats through the inhomogeneous magnetic field, as demonstrated in figure 5.7. A minor reduction of T_2^* is caused by dephasing due to motion along the read-out gradients, which is also visible in figure 5.7 as further shortening of T_2^* with increasing rotational velocity. Furthermore, the T_2^* reduces with increasing distance from the rotational axis, because the velocity increases, see figure 5.7. As the isochromats move from the slice outwards, the velocity component along the x-axis increases and so does the dephasing, leading to a loss of signal. Consequently, longer echo trains will produce even more shortened T_2^* values.

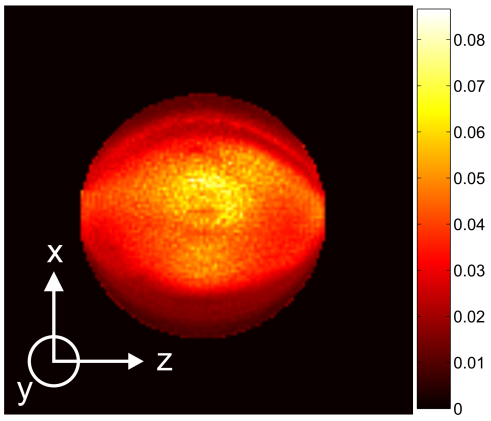

Figure 5.6: T_2^* distribution inside the disk for the motion phantom (static).

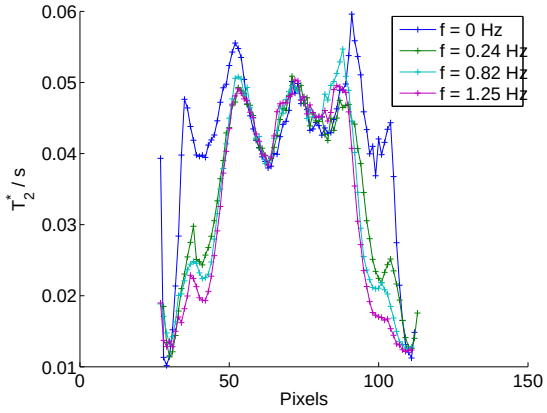

Figure 5.7: T_2^* profiles through the agarose disk of the motion phantom at different rotational velocities.

5.4 Cardiac Measurements

Although many researchers studied cardiac T_2^* values, no methodological standard for T_2^* mapping has been developed. Furthermore, Positano showed that variations of T_2^* exist along the circumference of the myocardium as well as from base to apex [49]. However, he found a correlation of mid-ventricular T_2^* values with the global T_2^* , which was confirmed by Yamamura [115], suggesting the septum in a mid-ventricular short-axis slice as an indicator for global cardiac T_2^* values. Besides the correlation of septal T_2^* with the global T_2^*, the motion of the septum due to the heartbeat and breathing is smaller than in other cardiac regions. The septal motion is further reduced during breathhold measurements allowing easy ROI positioning and analysis without complicated pixel tracking algorithm in cardiac real-time T_2^* mapping. These factors render the septum as an optimal choice for cardiac T_2^* measurement and analysis.

Literature T_2^* values for the septum in a mid-ventricular slice are given in table 5.2. Most of them represent healthy subjects. A cut-off at 20 ms is used to distinguish between healthy subjects and subjects with iron overload [116].

Reference	Pathology	Field Strength	Cardiac T_2^*
Reeder 1998, [117]	none	1.5 T	26-41 ms
O'Regan 2008, [118]	none	3.0 T	27.3 $\pm$ 6.4 ms
Anderson 2001, [119]	ventricular dysfunction	1.5 T	$<$ 20 ms
Anderson 2001, [119]	none	1.5 T	52 $\pm$ 16 ms
Pepe 2006, [120]	none	1.5 T	36.4 $\pm$ 6.7 ms
Di Tucci 2008, [121]	anemia	1.5 T	5.6 - 58.7 ms
Positano 2007, [49]	none	1.5 T	38.6 $\pm$ 7.2 ms
Smith 2011, [122]	thalassaemia major	1.5 T	4.5 - 43.8 ms

Table 5.2: Cardiac T_2^* values from different studies.

As presented in section 5.2, depending on the sampling length of the decay, only a certain range of T_2^* values can be reliably estimated. The desired long echo train contrasts the high temporal resolution required to resolve the cardiac phases properly [8]. A possible balance between both requirements is achieved by strong undersampling, which, however, reduces the SNR of the acquired data.

A region of interest with fixed position and small size to stay within the myocardium is

selected for analysis, see figure 5.8a. Keeping the ROI small and distant to the myocardial borders, reduces the influence of the magnetic susceptibility changes from the blood pool to the myocardium on T_2^* estimation. The slice thickness for multi-echo measurements has been increased to 8 mm to improve the SNR of each echo and therefore the T_2^* estimation. The measurement parameters are summarized in table 5.3.

Parameter	Single Echo	Multi-Echo
Resolution / mm^2	2.0 x 2.0	2.0 x 2.0
Slice Thickness / mm	6	8
TE 1 / ms	1.29	1.29
ΔTE / ms		0.96
TR /ms	2.00	5.96, 9.68, 9.68, 11.60
Number of Echoes	1	5,7,9,11
Number of Spokes	15	9,9,7,7
Temporal Resolution / ms	30	53.64, 87.12, 67.76, 81.20
Flip Angle / degree	8	15,17
Bandwidth / Hz·Px^{-1}	1953	1953
FoV / mm	256 x 256	256 x 256
Breathhold	yes	yes

Table 5.3: Measurement parameters for the human heart.

After data acquisition a reordering of image frames according to their ECG time stamp may be performed, yielding an 'artificial heart cycle' with extremely high temporal resolution, up to 2.5 ms. Images with the same ECG time stamp are averaged during the artificial heart cycle construction.

Binning and subsequent averaging of the artificial heart cycle yields an increase in SNR at the drawback of reduced apparent temporal resolution. The binning yields a temporal resolution corresponding to the width of the bins and inherently assumes that the cardiac cycles are similar. The increase in SNR is required to compensate for the small ROI and the strongly undersampled data.

5.4.1 Single-Echo Measurements

A representative temporal course of the signal intensity within a ROI of a single-echo measurement is shown in figure 5.8a. The signal intensity executes a periodic pattern with frequency of the heartbeat, see figure 5.8b. An example for an artificial heart cycles is displayed in figure 5.8c, where the signal intensity of the ROI is displayed. The outliers are due to the too short preparation scans where the magnetization has not reached the steady state when the image acquisition starts. The signal increase during systole is because the heart contracts and simultaneously moves up, bringing unsaturated isochromats into the imaging slice. Afterwards, during diastole relaxes the heart and the partly saturated isochromats move back into the original position within the imaging slice.

5.4.2 Multi-Echo Measurements

Representative T_2^* maps of a full cardiac cycle obtained by pixelwise linear least squared fit to the S-Exp model from a measured dataset with 9 echoes, 7 spokes and further parameters as given in table 5.3 are shown in figure 5.9. To increase the fitting performance, a mask is calculated using Otsu's method [123] on the root sum of squares of all echoes. After fitting, the range of

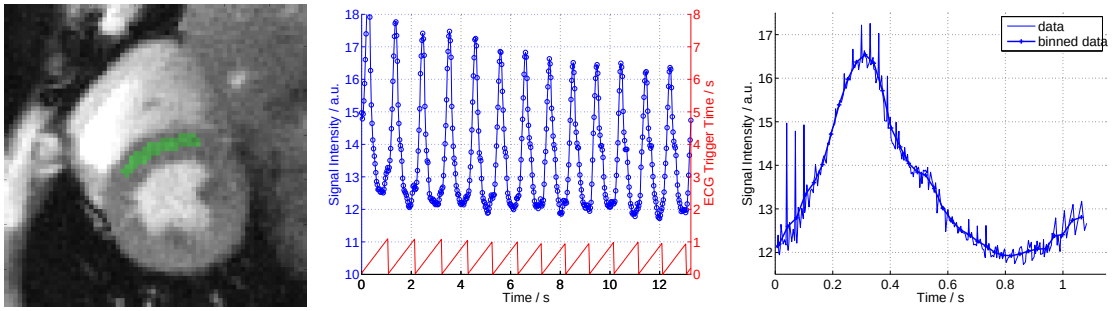

(a) ROI (b) Signal intensity (c) Binned signal intensity

Figure 5.8: ROI (a) and signal intensity of the ROI over time (b). In (c) the data is sorted according to the ECG time stamp into an artificial heart cycle and binned with a bin size of 30 ms.

the fitted T_2^* values is restricted to the interval $[0, 100]$ ms excluding values with low accuracy and precision.

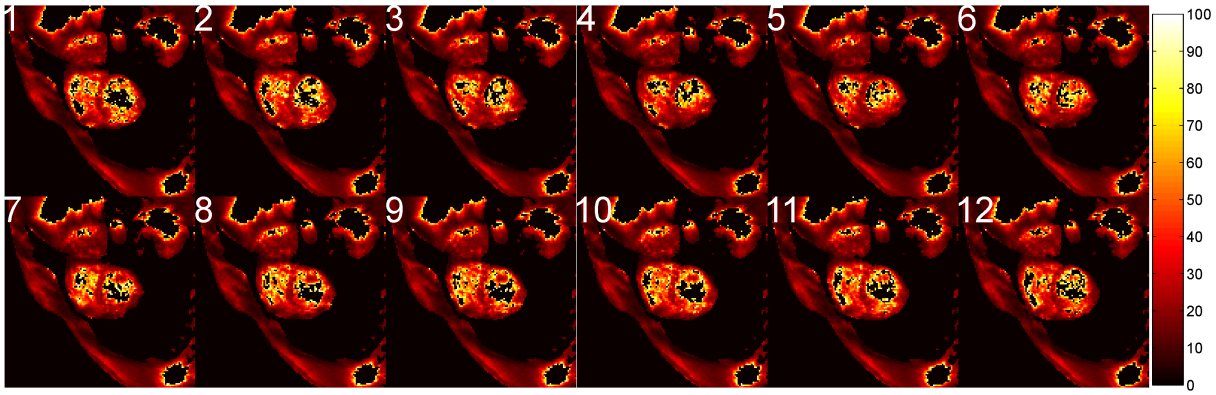

Figure 5.9: T_2^* maps of a full cardiac cycle from a volunteer measurement. Temporal resolution is 67.76 ms per frame and the colorbar represents the T_2^* values in milliseconds.

Quantitative results for a manually selected ROI (see figure 5.10a) in the septum are presented in figure 5.10. The pixel values in the ROI were averaged yielding only a single exponential decay, which allows the use of the more accurate non-linear fitting algorithms. Subfigures 5.10b, 5.10d, 5.10c and 5.10e show the fitting results for S_0, T_2^* and their Fourier transforms, respectively. The spectrum of the signal intensity shows a peak at around $f = 1.1$ Hz, representing the average heart beat. The T_2^* time series does not show such a clear modulation as the signal intensity, however, a modulation is visible. The spectrum of the T_2^* time series shows a peak at the average heartbeat frequency as obtained from the signal intensity spectrum, showing that periodically T_2^* changes exist within the ROI.

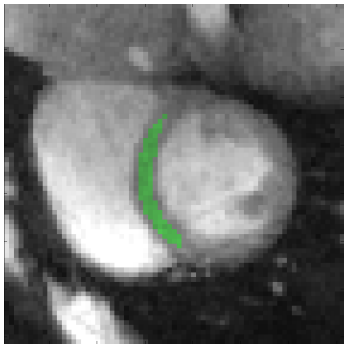

(a) ROI

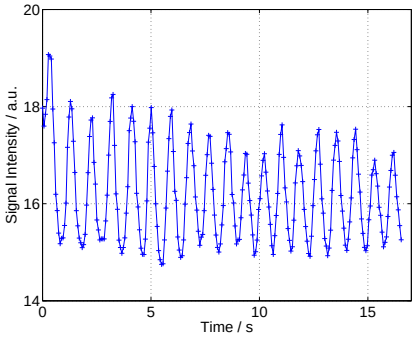

(b) Fitted S_0

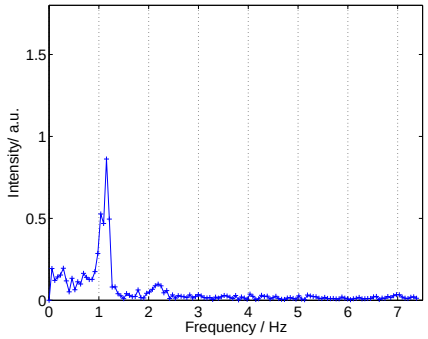

(c) Fourier transform of the S_0 time series

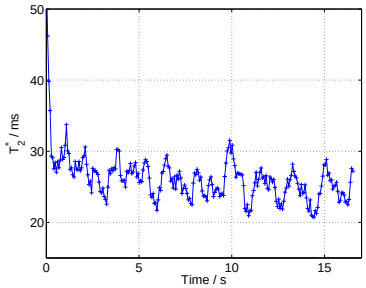

(d) Fitted T_2^*

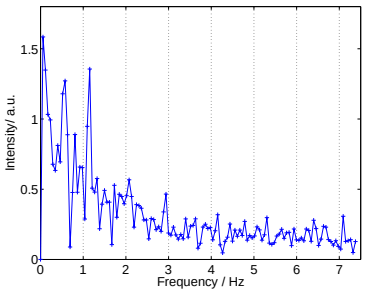

(e) Fourier transform of the T_2^* time series

Figure 5.10: Fitting results of the ROI in 5.10a and their Fourier transforms.

5.4.3 Fourier Analysis

Around 160 measurements from 12 volunteers with the parameters given in table 5.3 have been performed. For each measurement a ROI was manually selected and fitted nonlinearly to the S-Exp model. The Fourier transforms of the S_0 and T_2^* time series are displayed in figure 5.11. All S_0 and T_2^* spectra are normalized to 1 for better comparison. Since S_0 changes periodically with the heart beat, a strong peak in the S_0 spectrum representing the heart rate is visible, see figure 5.11. The spectrum of T_2^* has multiple peaks of different amplitudes but shows also a peak at the same frequency as the heartbeat. The peaks are observed at the same position independent of the measured volunteer, the number of echoes or the acquisition time, see figure 5.11. The measurements show that cardiac T_2^* is modulated with the heartbeat.

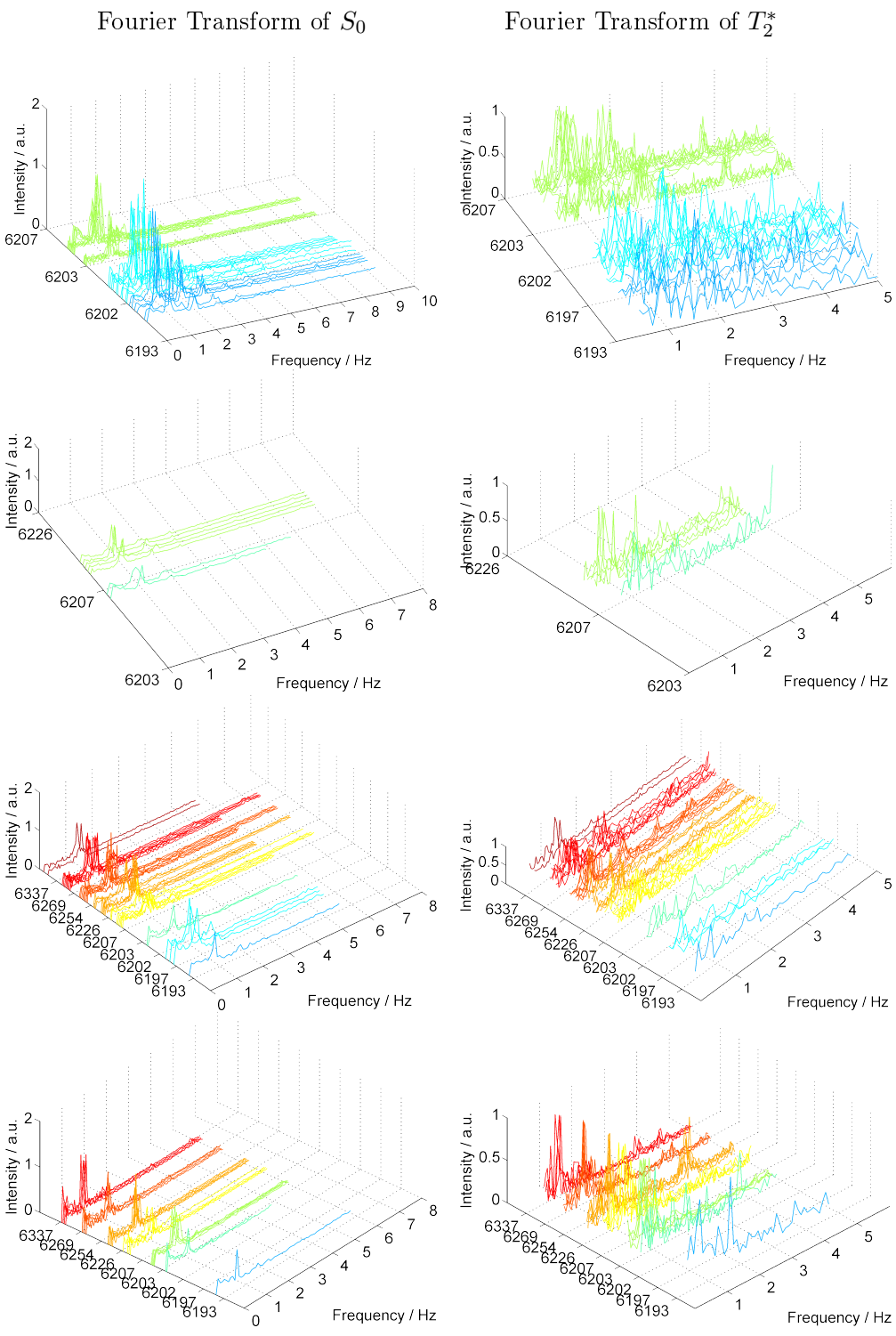

Figure 5.11: Spectra of the fitted signal intensity S_0 and the T_2^* decay for 12 volunteers. The data acquisition parameters are 5 echoes / 9 spokes (top row), 7 echoes / 9 spokes (second row), 9 echoes, 7 spokes (third row), 11 echoes , 7 spokes (bottom row). Both, S_0 and T_2^* have a peak at the same frequency around the typical heartbeat frequency of 1 Hz.

5.4.4 Binning

Although the temporal resolution of the cardiac T_2^* measurements is already between 50 and 100 ms, the temporal resolution is not high enough to clearly resolve cardiac T_2^* variations above noise. An even higher temporal resolution is achieved by sorting the fitted T_2^* values into an artificial heart cycles. The following binning with a width of 50 ms increases the SNR of the artificial heart cycle but reduces the temporal resolution. The results are presented in figure 5.12.

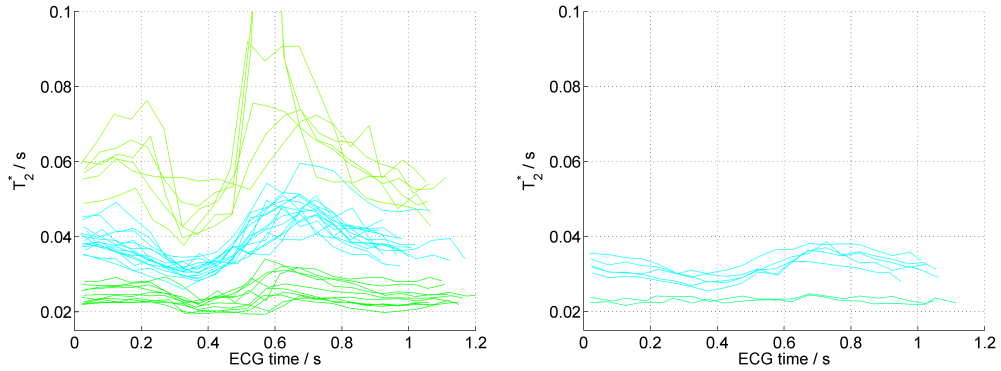

(a) 5 echoes

(b) 7 echoes

(c) 9 echoes

(d) 11 echoes

Figure 5.12: Binned T_2^* values over the artificial heart cycle. Each color represents a different volunteer with multiple measurements.

The interpretation of the binned data is difficult, because all estimated T_2^* values larger than 50 ms are unreliable due to the short sampling of the decay, especially with only 5 echoes. However, the measurements with 5 echoes exhibit the highest temporal resolution and thereby yield the most accurate resolution of cardiac phases. The T_2^* variation during the artificial heart cycles are highly reproducible and independent of the volunteer. The estimations from the measurements with 5 echoes show a clear variation of T_2^* . The same variation is also visible in measurements with more echoes but the reduced temporal resolution smooths the curves. However, some binned artificial heart cycles show only minor variations of T_2^* , which may be attributed to noise.

5.5 Discussion

Methods, confounding factors and results for cardiac T_2^* mapping in real-time were presented. Linear least-squares fitting is advantageous over nonlinear fitting for real-time T_2^* mapping because the fitting is fast, avoids problems with the initial guess and avoids convergence into local minima. The reduction in precision and accuracy is acceptable, due to only minor differences to the nonlinear fitting [111, 112]. The accuracy and precision of the linear least-squares fitting were evaluated with a simulated mono-exponential decay. The simulations showed that up to three times the last echo time the T_2^* estimation is accurate within 2 ms and precise to 5 ms. However, up to four times the last echo time, the accuracy is still below 2 ms, while the precision has reached an almost unacceptable level of about 16%. Therefore, four times the last echo time is considered as the maximum T_2^* value which can be estimated.

Single and multi-echo measurements with the motion phantom have been performed to evaluate the influence of motion on the signal. The single-echo measurements of the phantom showed a signal increase caused by the T_1-weighted inflow effect as well as signal decrease due to dephasing during the slice selection gradient. Both effects influence the final signal intensity of the measurement and the strength of each effect depends on the distance from the rotational axis, which determines the velocity and time outside the imaging slice.

The static T_2^* measurements of the agarose disk showed an inhomogeneous T_2^* distribution, which could not be homogenized by the shim. T_2^* decreases in the outer regions of the agarose disk with increasing rotational velocity. The reduction has been qualitatively identified as dephasing by motion through inhomogeneous magnetic fields as well as dephasing during the read-out gradient caused by the motion along the x-gradient. The dephasing by motion through inhomogeneous magnetic fields is stronger than dephasing produced by motion along the gradients.

The cardiac single-echo measurements showed a through-plane motion of the heart, which allows an average heart beat determination from the acquired real-time data. The septum has been selected as ROI for analysis in the cardiac multi-echo measurements because the septal T_2^* correlates with the global cardiac T_2^* [49, 115]. Furthermore, the motion of the septum is reduced during breathhold measurements, therefore being an optimal ROI for cardiac T_2^* analysis. The inherently low SNR of the cardiac multi-echo real-time acquisitions is increased with a ROI analysis. Furthermore, the fitted T_2^* are sorted into an artificial heart cycle with extremely high temporal resolution and binned to improve the SNR even further.

The measured T_2^* values in the septum are in general agreement with the literature. The acquired data shows changes in the estimated T_2^* with the periodicity of the heartbeat and differences of T_2^* between the post-systole and the end phase of the (artificial) cardiac cycle. These results suggest an influence from blood volume and blood oxygen level. However, temporal resolution, SNR and accuracy of the cardiac T_2^* measurements and fits are not high enough to exactly determine cardiac T_2^* variations. Furthermore, the T_2^* estimation may be biased by cardiac motion, as demonstrated with the motion phantom.

5.6 Conclusion

Real-time T_2^* measurements with a temporal resolution below 100 ms are possible. However, care has to be taken that the signal decay is sampled long enough and that motion does not induce a T_2^* shortening. Cardiac T_2^* measurements show T_2^* changes with the periodicity of the cardiac cycle. These changes in T_2^* may be attributed to blood oxygenation and volume changes as well as to cardiac motion. However, the exact cause is not yet determined. To investigate cardiac T_2^* further, faster acquisition methods like a multi-echo multi-spokes acquisition, higher field strengths or model-based approaches are needed. Furthermore, a more detailed analysis of

cardiac motion and its influence on T_2^* is also needed.

Other applications, where the T_2^* changes happen on a slower time scale are feasible. Such studies include brain T_2^* changes to blood oxygenation and volume or cartilage T_2^* measurements in the knee [13, 124] or calf muscles [125, 126] at rest and during motion.

Chapter 6

Water-Fat Separation in Real-Time MRI

Water-fat separation or suppression is common in clinical routine, because fat looks very bright on T_1-weighted images and can obscure pathologies. While MRI examinations usually require the absence of motion due to Cartesian sampling, Siemens recently presented radial data acquisitions which are more robust with respect to motion [127]. However, the advent of real-time MRI triggers the investigation of water-fat separation with respect to imaging of moving objects. The investigation includes the use of saturation pulses, the Dixon and other multi-echo methods as well as single-echo water-fat separation.

The first section starts with a review of the chemical shift theory and its effects on MR images. In the second section, the application of a saturation pulse is presented, followed by a novel water-fat separation approach using repetitive saturation pulses and a correlation analysis. The next section presents the classical Dixon method applied to real-time data, before the suitability of echo-time independent multi-echo water-fat separation methods for real-time MRI is investigated. The chapter proceeds with some single-echo water-fat separation methods and the presentation of the confounding factors for fat quantification. The following two sections explore the spatial and temporal resolution limits as well as water-fat separation at 7 T.

6.1 Theory

The separation of water and fat is possible because of slightly different resonance frequencies of hydrogen protons bound in water and fat molecules. The electronic shielding produced by moving electrons reduces the effective magnetic field at the hydrogen nucleus producing a different resonance frequency. Each chemical environment with a different number of electrons and covalent bindings leads to a different electronic shielding of the nuclei, called chemical shift.

The lipid spectrum is complicated and consists of numerous resonance peaks which correspond to the different chemical groups found in lipids [128, 129].

In the early days of water-fat separation only the major peak from the $-CH_2$ groups of lipids was considered [28, 29]. The frequency difference Δf_{fw} is given by the Larmor frequencies of the hydrogen protons in fat f_f and water f_w:

$$\Delta f_{\mathrm{fw}} = f_f - f_w = -\sigma_{\mathrm{fw}} \frac{\gamma}{2\pi} B_0 \tag{6.1}$$

with γ the gyromagnetic ratio for hydrogen and B_0 the magnetic field. The chemical shift between water and the major fat peak is expressed either as a dimensionless quantity $\sigma_{\mathrm{fw}} = 3.35 - 3.5\,\mathrm{ppm}$

or as frequency shift Δf_{fw}, which at $B_0 = 2.89\,\mathrm{T}$ is $\Delta f_{\mathrm{fw}} = 412 - 430\,\mathrm{Hz}$. Below, the water/fat-signal is meant as the signal from the hydrogen protons in water or fat molecules.

Since the resonance frequencies are used to encode the position of the resonating hydrogen atoms, misregistration artifacts appear after the image reconstruction for objects containing water and fat [37]. The resonance frequency for the location of the object is given by

$$f(r) = \frac{\gamma}{2\pi}\vec{G}\vec{r} + \Delta f_{\mathrm{fw}}(\vec{r}) \tag{6.2}$$

with imaging gradient $\vec{G}$ and location $\vec{r}$. Equation 6.2 shows that the misregistration shift in the image is determined by the chemical shift frequency and the imaging gradient, which depends on the bandwidth per voxel $\mathrm{BW_{vx}}$. With position of water r_w and fat r_f, the misregistration shift in terms of the voxel size Δr is

$$\Delta r_{\mathrm{shift}} = r_w - r_f = \frac{\Delta f_{\mathrm{fw}}}{\frac{\gamma}{2\pi}G} = \frac{\Delta f_{\mathrm{fw}}}{\mathrm{BW_{vx}}}\Delta r \tag{6.3}$$

Thus, the signal intensity of fat is shifted by $\Delta r_{\mathrm{shift}}$, with reference to the signal intensity from water which remains at its position. The misregistration effect can be minimized by acquiring data with a very high bandwidth per voxel. The misregistration effect occurs also for the slice excitation and is minimized if the slice is excited with maximum gradient strength. Both conditions are usually fulfilled in real-time MRI, because image acquisition time is minimized using maximum gradient strength.

In Cartesian imaging the signal is shifted along the direction of the read-out gradient, shifting all voxels in the same direction. For radial imaging this effect leads to blurring, because the read-out gradient changes its direction for each measured spoke.

Another effect is the different phase accumulation due to the differing resonance frequencies. Today, the temporal signal evolution in the image domain is modeled as

$$S(t) = \left(W e^{-R^*_{2,w}t} + \sum_{j=1}^{M} F_j e^{(2\pi i \Delta f_{\mathrm{w,f}_j} - R^*_{2,f_j})t} \right) e^{2\pi i \psi t} \tag{6.4}$$

with the water component W, its relaxation $R^*_{2,w} = 1/T^*_{2,w}$, the fat magnitude of the respective fat peak F_j, $j \in \{1, ..., M\}$, its phase $2\pi i \Delta f_{\mathrm{w,f}_j} t$ at time t with frequency shift $\Delta f_{\mathrm{w,f}_j}$, relaxation component $R^*_{2,f_j} = 1/T^*_{2,f_j}$ and the phase introduced by the field inhomogeneity ψ. The model in equation 6.4 is a very general model and several simplifications are possible [130] and used for different water-fat separation methods. Depending on the model $W, F_j \in \mathbb{C}$ (without initial phase) or $W, F_j \in \mathbb{R}$. The signal is measured at discrete time points t_n with typical $n \in \{1, 2, 3, 6\}$.

In the ideal case of a single fat peak and no relaxation of the water and fat signals, equation 6.4 reduces to

$$S(t) = \left(W + F e^{2\pi i \Delta f_{\mathrm{fw}} t} \right) e^{2\pi i \psi t} \tag{6.5}$$

where only three parameters need to be determined.

6.2 Saturation Methods

Saturation pulses are usually applied before the excitation of each k-space line, which ensures the suppression of unwanted signal during the data acquisition. Saturation pulses are spectrally selective and therefore have a prolonged duration [41], which exceeds multiple TRs of a typical

real-time acquisition. However, utilizing the speed of the real-time acquisition, a complete image without the saturated chemical species can be acquired after a single saturation pulse. A more homogeneous field improves the saturation of unwanted signals as shown in figure 6.1, where images from a water saturated real-time series are shown. The shim was performed in resting position, as shown by the top row of figure 6.1. Note the improvement from no shim (tune up) over standard shim (single 3D excitation and optimization) to advanced shim (3x 3D excitation and optimization) for the resting leg as well as during motion as depicted in the lower row of figure 6.1.

Tissue	T_1 / ms	T_2 / ms
Gray Matter	1820	99
White Matter	1084	69
Muscle	1412	50
Fat	366-429	53-133
Blood	1932	275

Table 6.1: T_1 and T_2 values at 3 T for different tissues [131–133].

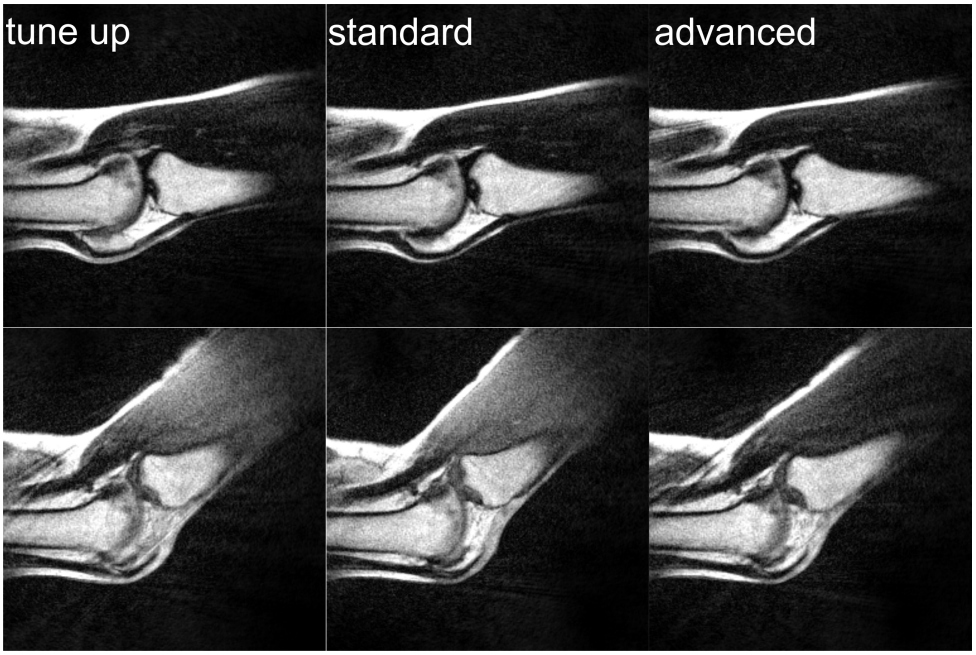

Figure 6.1: Water saturated images from real-time acquisitions of a knee with different shims.

Due to the short T_1 of fat (see table 6.1), the transverse magnetization from fat recovers fast, leading to incomplete fat suppression for longer acquisition times, see figure 6.2.

Selected frames from a representative real-time water and fat saturation time series with a saturation pulse between each frame are visible in figures 6.3. The data was acquired with standard shim, leaving residual magnetization in the water saturation time series. The remaining signal in the fat saturation time series is due to the standard shim and relatively long acquisition time of 146.7 ms per frame.

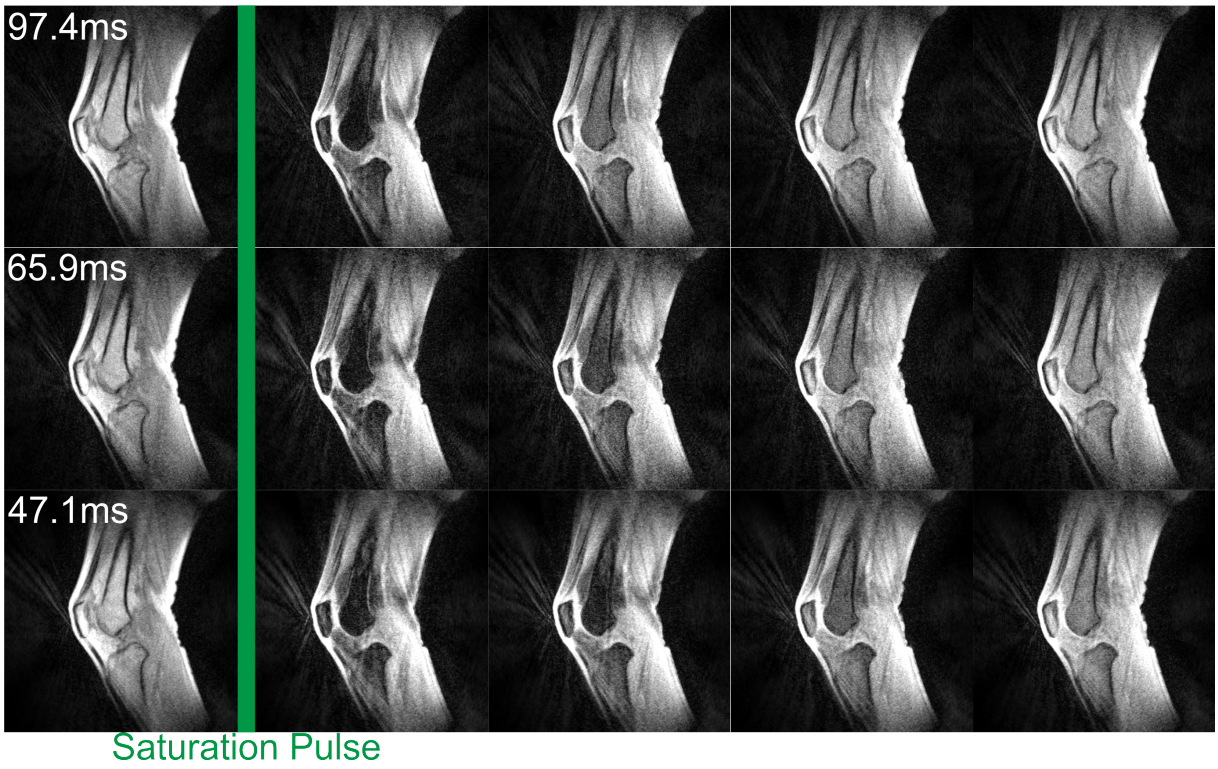

Figure 6.2: Signal increase after fat saturation pulse (green line) applied after the first frame of the image series for different temporal resolution as given in the upper left corner of each series. With shorter temporal resolution the fat saturation persist over more images, as visible in the lower row.

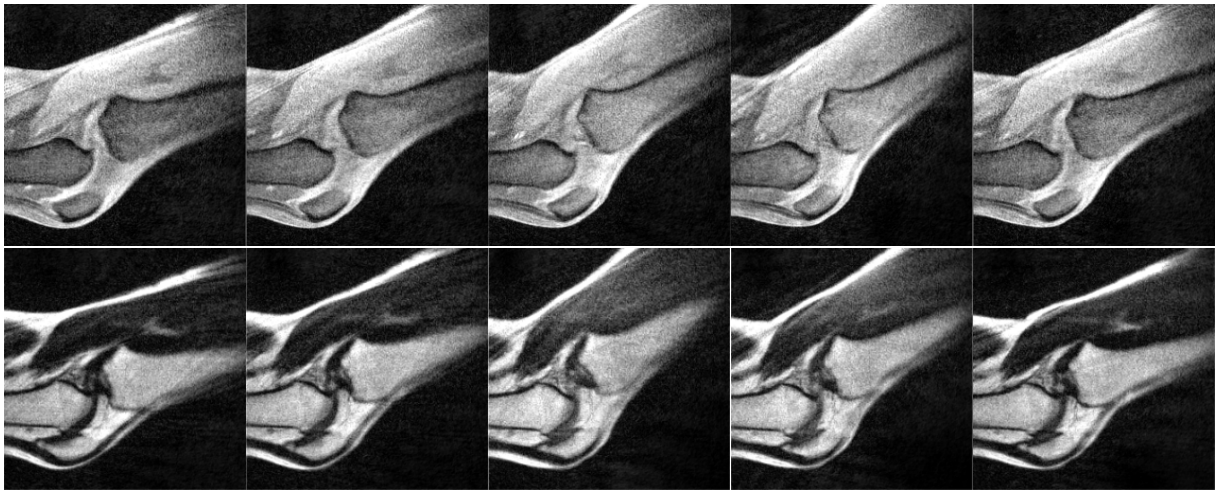

Figure 6.3: Selected frames from a real-time data set with fat (top row) and water (bottom row) saturation pulses applied between each frame (146.7 ms/45 spokes).

6.2.1 Correlation Water-Fat Separation

A water-fat separation method that uses repetitively applied saturation pulses was developed by the author [134]. The principle is similar to functional MRI, where the activation of the brain is correlated with an applied paradigm. In the correlation water-fat separation method saturation pulses are applied repetitively, e.g. every 10th frame, according to a given paradigm. The measured data is then pixelwise correlated with the paradigm. Here, the paradigm is calculated from all pixels using the L2-norm of each image. An example of the paradigm is displayed in figure 6.4. Following the fMRI approach, each pixel time series is correlated with the paradigm using the Pearson linear correlation coefficient c. The p-value using a student's t-distribution is also calculated. If the correlation is significant ($p < 0.05$) and positive ($c > 0$), then the magnitude of the logarithm of p is assigned to that pixel, otherwise the pixel value remains zero. The logarithm reduces the large range of correlation values. The whole procedure is outlined in figure 6.4.

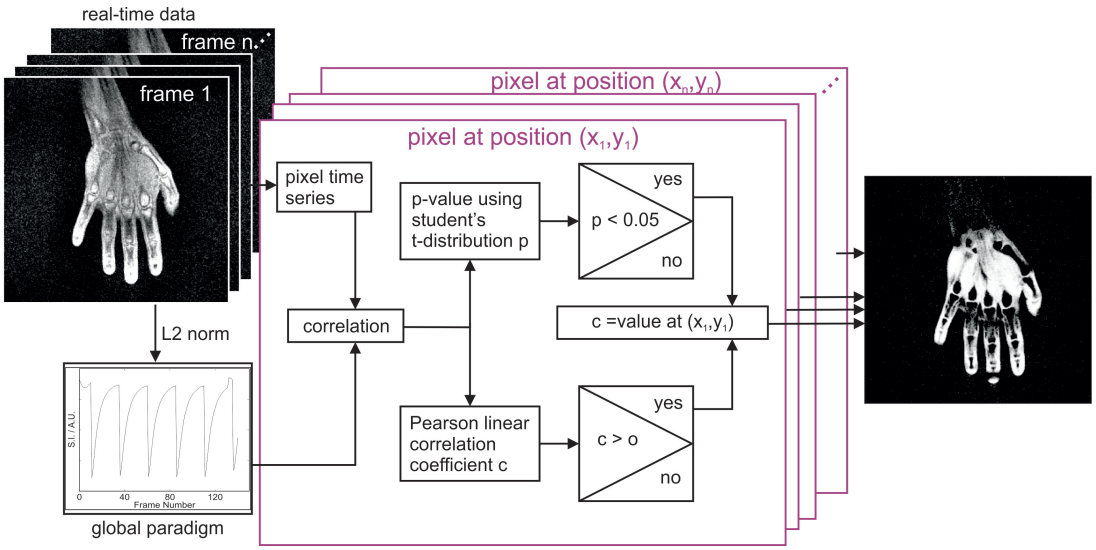

Figure 6.4: Outline of the correlation separation scheme, for detail see text.

Some representative results are presented in figure 6.5, showing that the method works quite well. However, the quality of the images corresponds to the quality of the saturation pulses. For the hand, the head and the knee the saturation is very good and homogeneous, whereas for the abdomen the saturation is inhomogeneous and noisy. The inhomogeneous saturation is caused by an inhomogeneous B_1 excitation. The noise in the water or fat images depends on the quality of the correlation, which is influenced by motion and the duration of the measurement. Short measurements combined with motion produce noisier maps than long measurements without motion.

Although the correlation separation method works quite well on static objects it is not superior to conventional saturation or water-fat separation methods. A drawback is that although a fast real-time data acquisition is used the imaged object must be static or a motion tracking or correction algorithm has to be applied, rendering it unsuitable for real-time water-fat separation of moving objects.

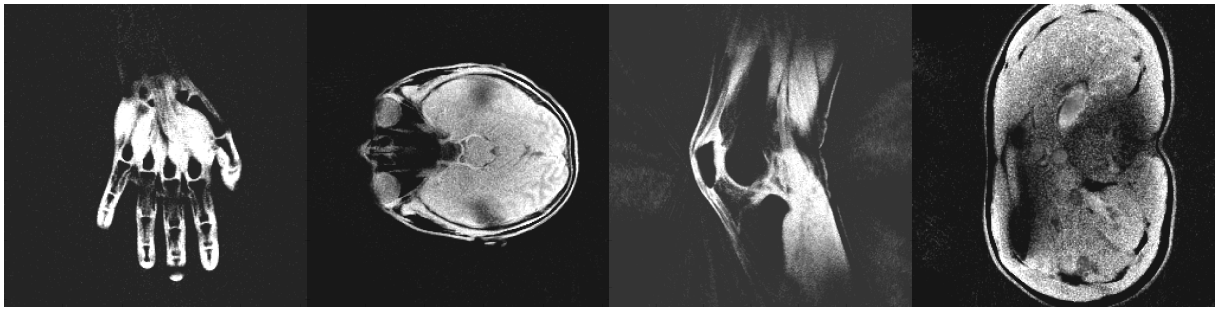

(a) Water, Hand (b) Water, Head (c) Water, Knee (d) Water, Abdomen

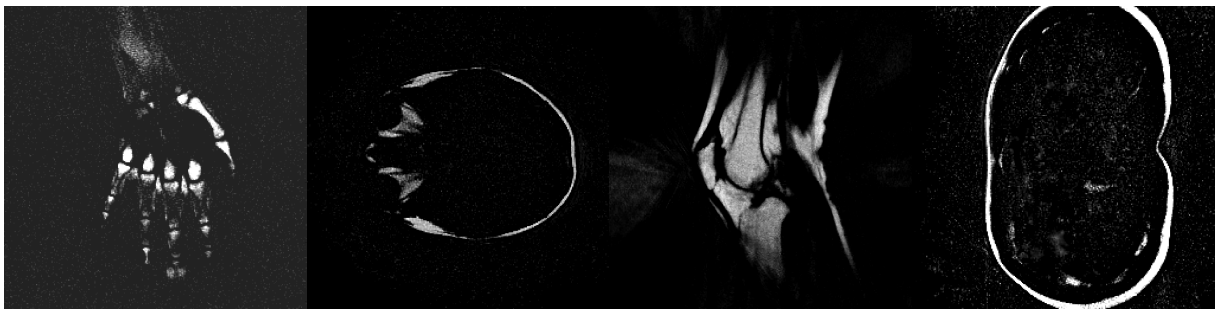

(e) Fat, Hand (f) Fat, Head (g) Fat, Knee (h) Fat, Abdomen

Figure 6.5: Representative results of the correlation water-fat separation.

6.3 Dixon Methods

All Dixon water-fat separation methods investigated in the following sections use the same measured data set with three echoes, allowing a comparison between the methods. For the two-point and extended two-point Dixon method the third echo was discarded. The measurement parameters are summarized in table 6.2 and the results are displayed in the respective sections.

Resolution /mm^2	1.00 x 1.00	
Slice Thickness /mm	5.00	
Base Resolution	256	
RepetitionTime /ms	6.00	
Echo Times / ms	2.42, 3.63, 4.84	
Bandwidth per Pixel / Hz	930	
Flip Angle / degree	8	
Field of View / mm	256	
Acquisition time per water/fat map	# Spokes	Time / ms
	25	150.00
Separation Method	Dixon	
Newton Steps	6	

Table 6.2: Measurement parameters for the data used by the Dixon water-fat separation methods.

6.3.1 Two-Point Dixon Method

The original idea was proposed by Dixon in 1984 [28]. He modeled fat as a single methylene peak with a chemical shift of $\sigma_f = 3.35\,\text{ppm}$ (with respect to water) and suggested to acquire only two images. One of the two images is acquired at 'in-phase' conditions and the other at 'opposed phase' conditions. At in-phase conditions water and fat components have the same phase, whereas at opposed phase conditions, they have a phase difference of π. The influence of the field inhomogeneity was neglected ($\psi = 0$), and the signal equations derived from equation 6.5 are

$$S(t_1) = W + F \qquad \text{in-phase} \tag{6.6}$$

$$S(t_2) = W - F \qquad \text{opposed phase} \tag{6.7}$$

From these two images, water and fat separated images can be easily calculated on a pixelwise basis:

$$W = \frac{1}{2}\left(S(t_1) + S(t_2)\right) \tag{6.8}$$

$$F = \frac{1}{2}\left(S(t_1) - S(t_2)\right) \tag{6.9}$$

Typical results for a moving object measured with real-time water-fat separation using the two-point Dixon method are shown in figure 6.6. As visible in figure 6.6, the field inhomogeneity can not be neglected, leading to the extended two-point Dixon method proposed by Skinner [31] and Coombs [135]. The field inhomogeneity is estimated using the argument of $S(t_2)^2$ [31] or from $\arg\left(S(t_1)S(t_2)\right)^2$ [135] with $S(t_2) = (W - F)\exp\left(2\pi i \psi t_2\right)$. In both cases spatial phase unwrapping might be necessary to obtain a correct field map. After the phase unwrapping, the field inhomogeneity is removed and improved water-fat separation is obtained.

Results of the extended two-point Dixon water-fat separation without phase unwrapping are shown in figure 6.7. The water-fat separation is improved compared to the two-point Dixon method, but the field map is not estimated correctly for every frame leading to water-fat swaps.

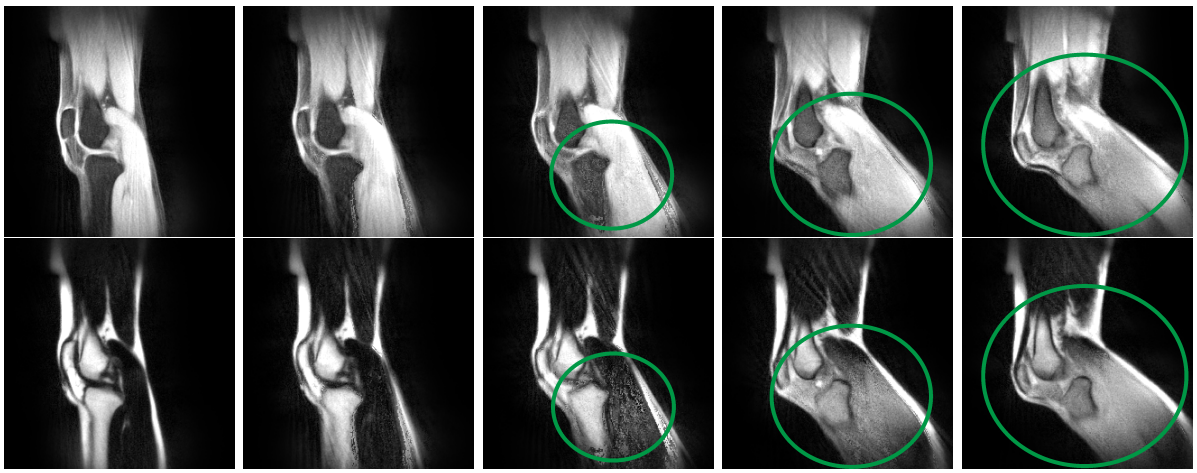

Figure 6.6: Real-time Water-Fat separation with the two-point Dixon method. Top row shows the water images and the bottom row shows the fat images. Water-fat swaps are indicated by a green circle.

In conclusion, both methods deliver real-time water-fat separated images with a negligible reconstruction time. However, in the presence of motion the disregard of the field map or its

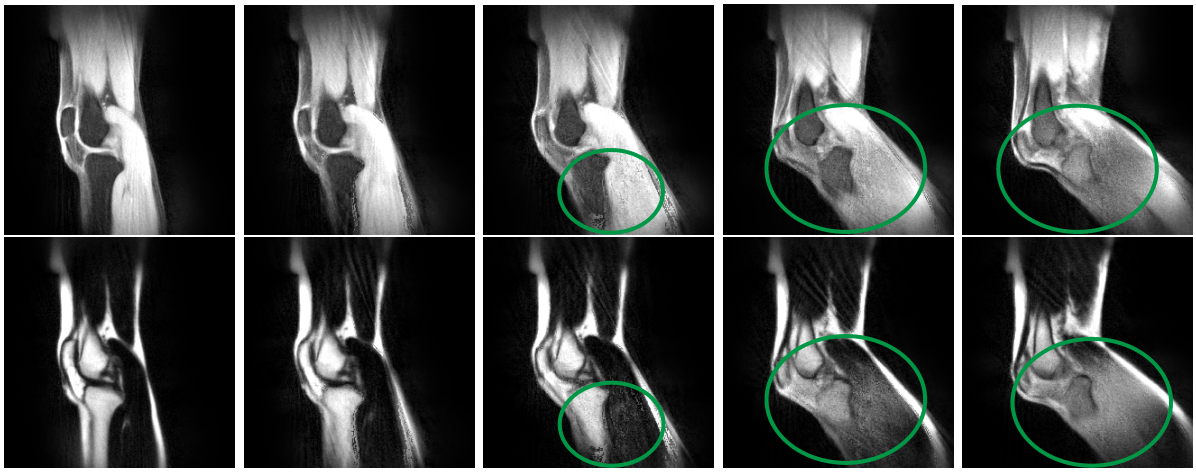

Figure 6.7: Real-time water-fat separation with the extended two-point Dixon method. Top row shows water images and the bottom row shows fat images. Water-fat swaps are indicated by a green circle.

incorrect determination produces water-fat swaps, which may be resolved with phase unwrapping or better field map estimations.

Besides these two-point water-fat separation method, many other methods for two-point water-fat separation have been proposed [136–139]. Their main difference is how the field inhomogeneity map is estimated and the restrictions of the echo times to in-phase/opposed-phase conditions. The algorithms presented by Eggers [136] and Berglund [139] were implemented, but they did not produce good water-fat separated images.

6.3.2 Three-Point Dixon Method

The three-point Dixon method was developed by Glover in 1991 [29]. It assumes as the original two-point Dixon method only a single fat peak and acquires three images at in-, opposed- and in-phase conditions. The phase $\phi_k = 2\pi i \Delta f_{\mathrm{fw}} t_k$, $k \in \{1, 2, 3\}$ in equation 6.5 between water and fat depends on the echo time t_k and is set for in-phase acquisitions to $\phi_3 \in 2\pi\mathbb{N}_0$. At opposed phase conditions the echo time t_2 is selected so that $\phi_2 \in \{x : x = (2n+1)\pi, n \in \mathbb{N}\}$ yielding for the signal equations

$$S_1 = (W + F)\exp(i\phi_0) \qquad j \in \{1, ..., N\} \tag{6.10}$$

$$S_2 = (W - F)\exp(i\phi_0)\exp(i\psi) \tag{6.11}$$

$$S_3 = (W + F)\exp(i\phi_0)\exp(i2\psi) \tag{6.12}$$

with W and F the magnitude of water and fat signals, ϕ_0 as phase offset for both components and ψ is the phase from magnetic field inhomogeneity for frame j of which N frames are measured. With the switch function p_c

$$p_c = \cos(\arg(S_2 \exp(-i\phi))) \tag{6.13}$$

the fat-water separated images are

$$I_{\mathrm{f}} = \frac{1}{2}\left(\sqrt{|S_1'|\,|S_3''|} - p_c\,|S_2'|\right) \tag{6.14}$$

$$I_{\mathrm{w}} = \frac{1}{2}\left(\sqrt{|S_1'|\,|S_3''|} + p_c\,|S_2'|\right) \tag{6.15}$$

Representative results are displayed in figure 6.8. The field map estimation is much better than with the two-point Dixon water-fat separation methods, yielding less frames with water-fat swaps and improved separation of pure water and fat voxels, e.g. the signal void in the only-fat and only-water containing voxels is much darker than compared to the two-point Dixon separation. However, the echo times are fixed, which imposes undesired restrictions to the image acquisition. Moreover that water-fat swap free images are still out of reach with this approach.

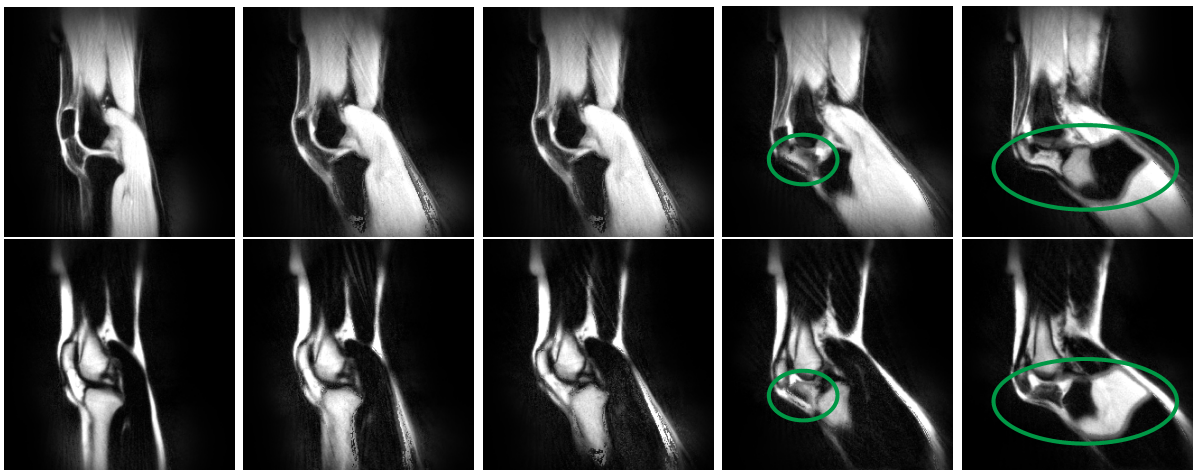

Figure 6.8: Real-time water-fat separation with the three-point Dixon method. Top row shows water images and the bottom row shows fat images. Water-fat swaps are indicated by a green circle.

6.3.3 Temporal Phase Unwrapping

Temporal Phase Unwrapping suggested by the author is an extension to the three-point Dixon (3PD) method, because the field map estimation suffers from phase wrapping along the time dimension of the real-time series. Each pixel time series was unwrapped using Itoh's method [36], which adds the phase differences between temporally adjacent voxels to the initial voxel. Because in real-time imaging motion may be encountered, each pixel time series is splitted into regions of noise and signal and phase unwrapping is restricted to signal regions. Temporal phase unwrapping fails in the presence of spatial phase wraps at the initial frame. These cases require additional spatial phase unwrapping. Temporal phase unwrapping improves the water-fat separation of the 3PD method further as shown in figure 6.9. However, the approach of temporal phase unwrapping must be extended to consider spatial phase in a local neighborhood to improve phase unwrapping robustness.

6.4 Multi-Echo Methods

In this section results and extensions to real-time imaging of the multi-echo water-fat separation methods 'Direct Phase Encoding' (DPE), 'Analytical water/fat separation with a safest-first region-growing scheme' (ASR), 'Iterative Decomposition of water and fat with Echo Asymmetry and Least-squares' (IDEAL) are presented. These water-fat separation methods relax the echo time restrictions from in- and opposed-phase times to (almost) arbitrary echo times, providing higher flexibility on the choice of acquisition parameters. A single data set was used for all water-fat separation methods with acquisition parameters summarized in table 6.3.

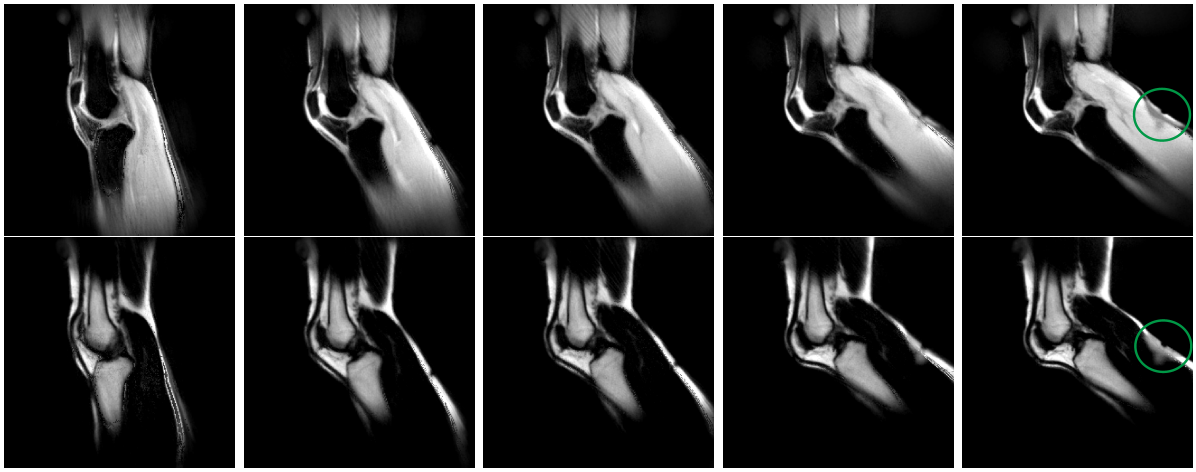

Figure 6.9: Real-time water-fat separation with the extended three-point Dixon method and phase unwrapping of the field map. Top row shows water images and bottom row shows fat images. Note the water-fat swap in the last frame from the incorrect phase unwrapping indicated by the green circle.

Resolution /mm^2	1.00 x 1.00	
Slice Thickness /mm	5.00	
Base Resolution	256	
RepetitionTime / ms	5.95	
Echo Times / ms	1.83, 3.35, 4.87	
Bandwidth per Pixel / Hz	930	
Flip Angle / degree	8	
Field of View / mm	256	
Acquisition time per water/fat map	# Spokes	Time / ms
	45	267.75
Separation Method	DPE, IDEAL, ASR	
Newton Steps	6	

Table 6.3: Measurement parameters of the data used by the multi-echo water-fat separation methods.

6.4.1 Direct Phase Encoding

Direct phase encoding (DPE) was introduced by Xiang and An [32] and allows for water-fat separation and identification. The MRI signal may be sampled at arbitrary echo times, including in-phase and opposed phase echo times. The spectral complexity of fat is not taken into account, fat is assumed to have only the methylene peak. The used signal model is

$$S(t) = (W + F\exp(i\Delta\omega_{\mathrm{wf}}t))\exp(i\gamma\Delta B_0 t + i\phi) \tag{6.16}$$

with W and F the water and fat amplitudes as real quantities, $\Delta\omega_{\mathrm{wf}} = 2\pi\Delta f_{\mathrm{wf}}$ the chemical shift between water and fat, t the echo time, ΔB_0 the field inhomogeneity and other phase errors combined in ϕ. DPE requires equidistant echo times, which allow for the derivation of a quadratic equation. The two solutions reflect the ambiguity between water and fat which can be resolved using the particular phase relation between water and fat. A local and global orientation filter are subsequently applied yielding corrected water and fat maps. These can be improved in SNR with a second pass solution. Water and fat separated frames with DPE of a

real-time series are displayed in figure 6.10.

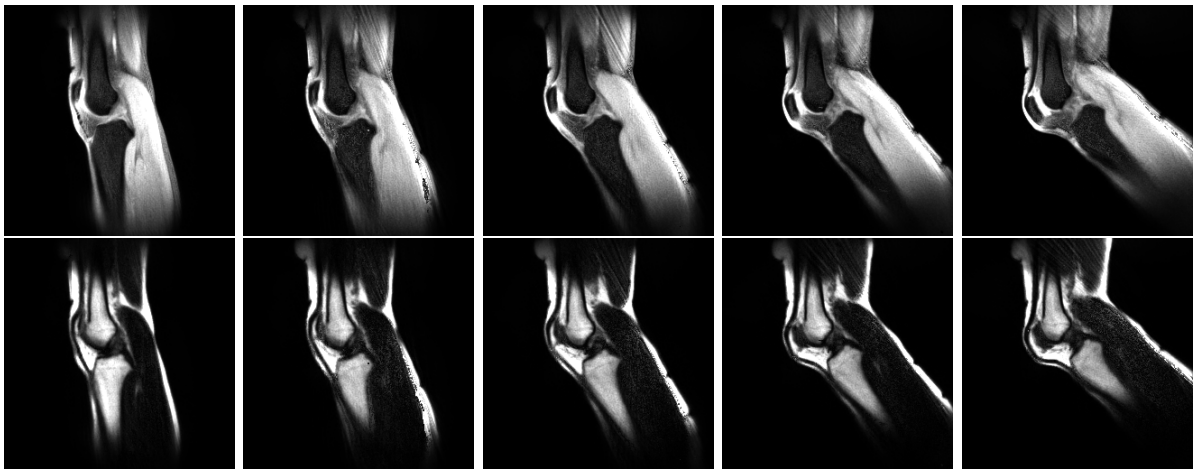

Figure 6.10: Water-fat separated frames with DPE and second pass solution. Top row shows water and bottom row shows fat images.

The DPE works bettern than the 3PD for water-fat separation on real-time data. However, the time DPE required to separate water and fat is long, denying the direct display of the water and fat images. With the usage of a multi-peak fat model, the DPE algorithm fails to produce swap-free water-fat separated images because the defined relationship between water and fat is abandoned. Without the multi-peak model, DPE water-fat separation leads to incomplete water and fat separation, denying fat quantification [140]. Furthermore, DPE does not take advantage of the available serial data since each frame is reconstructed by itself. A possible way to include real-time data properties is the extension of the orientation filters to temporal neighboring frames, which should improve the robustness of the DPE water-fat separation.

6.4.2 ASR

The ASR algorithm was proposed by J. Berglund [33] in 2010 for whole body imaging. The method uses a single-peak fat model and models the signal as

$$S_1 = (W + a_0 F) \tag{6.17}$$
$$S_2 = (W + a_0 a F)\, b \tag{6.18}$$
$$S_3 = \left(W + a_0 a^2 F\right) b^2 \tag{6.19}$$

with the complex water and fat signals W and F and the phasors

$$a_0 = \exp\left(2\pi i \Delta f_{\mathrm{wf}} t_0\right) \tag{6.20}$$
$$a = \exp\left(2\pi i \Delta f_{\mathrm{wf}} \Delta t\right) \tag{6.21}$$
$$b = \exp\left(2\pi i \gamma \Delta B_0 \Delta t\right) \tag{6.22}$$

with chemical shift between water and fat Δf_{wf}, first echo time t_0 and echo time spacing Δt and field inhomogeneity ΔB_0.

A quadratic equation of the field inhomogeneity phasor is derived from equations 6.17-6.19 providing two possible solutions for each pixel. The correct field inhomogeneity map is coherently grown from multiple seed pixels. The coherence between neighboring pixels is high if their phase difference is small. Once the true field inhomogeneity map is grown, water and fat maps are derived from equations 6.17-6.19.

Extensions

For complete water-fat separation the spectral complexity of fat must be taken into account [130, 140], but the publication of the ASR algorithm uses only a single-peak model for fat. The extension of the ASR algorithm to the multi-peak fat model as developed by the author is straight forward, only the phasors a and a_0 must be adapted.

$$a_0 = \sum_{j=1}^{M} F_j \exp\left(2\pi i \Delta f_{\mathrm{w,f}_j} t_0\right) \tag{6.23}$$

$$a = \sum_{j=1}^{M} F_j \exp\left(2\pi i \Delta f_{\mathrm{w,f}_j} \Delta t\right) \tag{6.24}$$

with the resonance frequency differences to water $\Delta f_{\mathrm{w,f}_j}$ and relative intensities F_j of the M fat peaks. The values for the chemical shifts and relative intensities are given in table 6.5 [128].

A comparison between the single- and multi-peak fat model is shown in figure 6.11, where no difference between the two models is visible. However, a ROI analysis of structures containing fat, shows increased signal intensity in the multi-peak fat map for each ROI as presented in table 6.4.

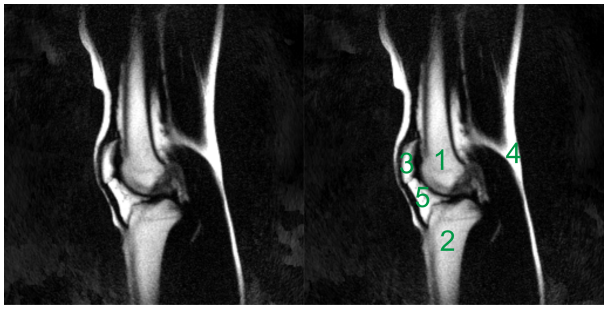

Figure 6.11: Representative fat maps of a ASR water-fat separation with usage of the single-peak fat model (left) and the multi-peak fat model (right).

ROI	Single-Peak Fat Model	Multi-Peak Fat Model
Femur(1)	69	104
Tibia(2)	68	103
Patella(3)	80	120
Subcutaneous(4)	110	164
Fat Pad(5)	79	118

Table 6.4: Signal intensity comparison of lipid rich regions.

The reconstruction time is a crucial factor for real-time applications, due to the large amount of acquired data. Although the reconstruction time could be significantly reduced for the Matlab implementation, only an implementation in C resulted in sufficient fast water-fat separations.

Real-time water-fat separation is possible using a sequential, framewise water-fat separation as demonstrated in figure 6.12. For the first frames the framewise ASR water-fat separation delivers correctly separated water and fat images, but as the leg is bent the framewise ASR real-time water-fat separation fails in regions where the field inhomogeneity is large.

The phase between the frames changes for each pixel smoothly over time, even in the presence of motion, which is exploited in the ASR algorithm by performing an in-plane phasor coherent region growing with additional consideration of the phasor from the previous, already determined frame (see figure 6.13). In detail, for each pixel the coherence is determined using not only the in-plane neighbors but also the previous phasor value at the same pixel position. The approach developed by the author is called 2.5D ASR because it uses the time as third dimension but only in the backwards direction. The 2.5D ASR delivers water and fat images free of water and fat swaps, as demonstrated in figure 6.14.

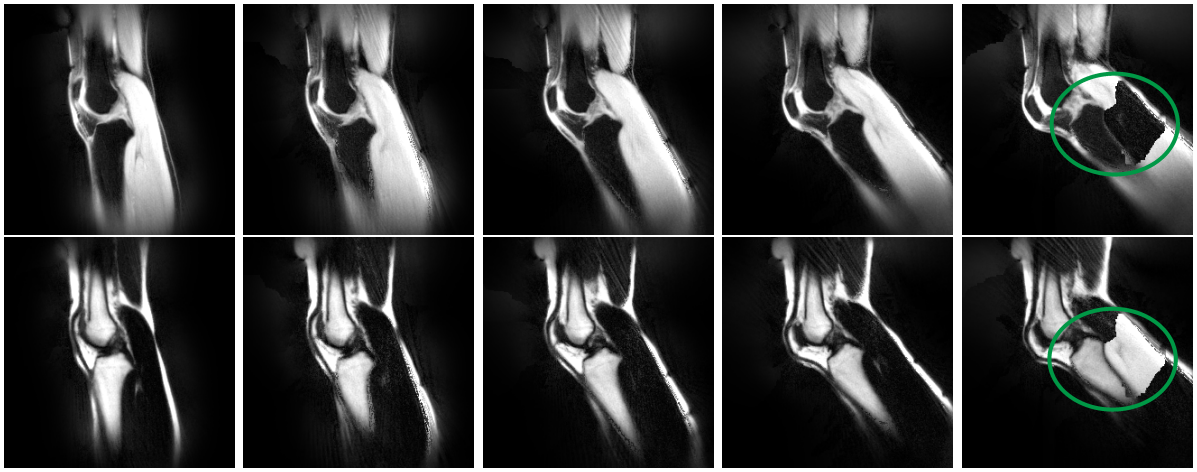

Figure 6.12: Framewise ASR water-fat separation. Top row shows water and bottom row shows fat images. Note the severe water-fat swaps at the end of the time series (green circle).

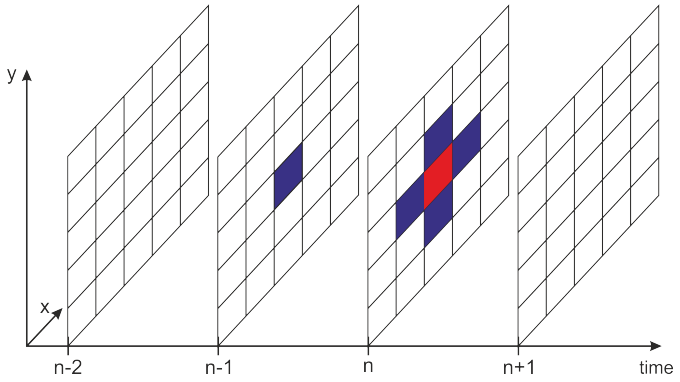

Figure 6.13: Schematic outline of the 2.5D region growing process. The pixels marked in blue are used for the 2.5D region growing of the red pixel.

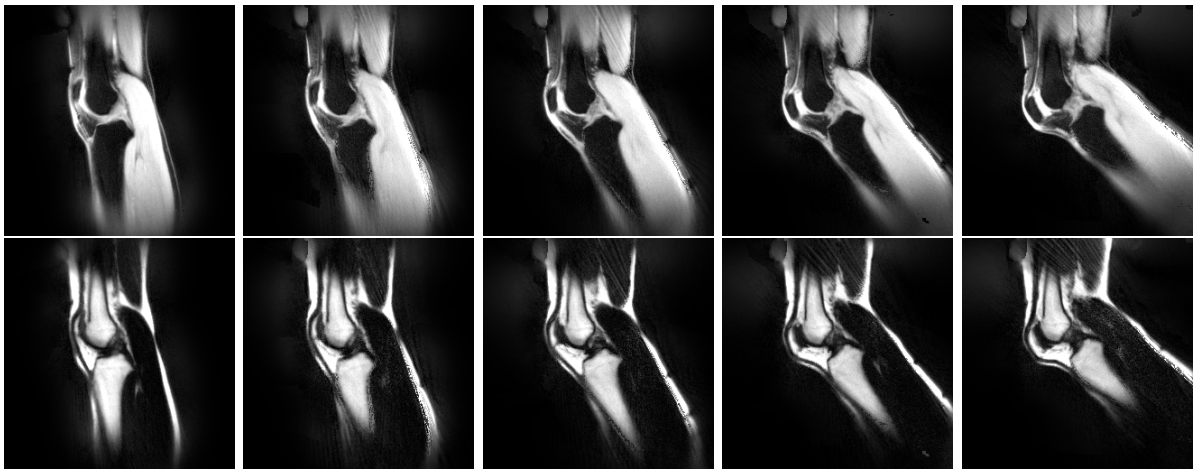

Figure 6.14: 2.5D ASR water-fat separation with coherence calculation including the previous frame. Top row shows water and bottom row shows fat images.

Rearranging the data into a 3D data set, with time as third dimension, as visualized in figure 6.13, and running a 3D reconstruction is another possibility to use the temporal phase evolution.

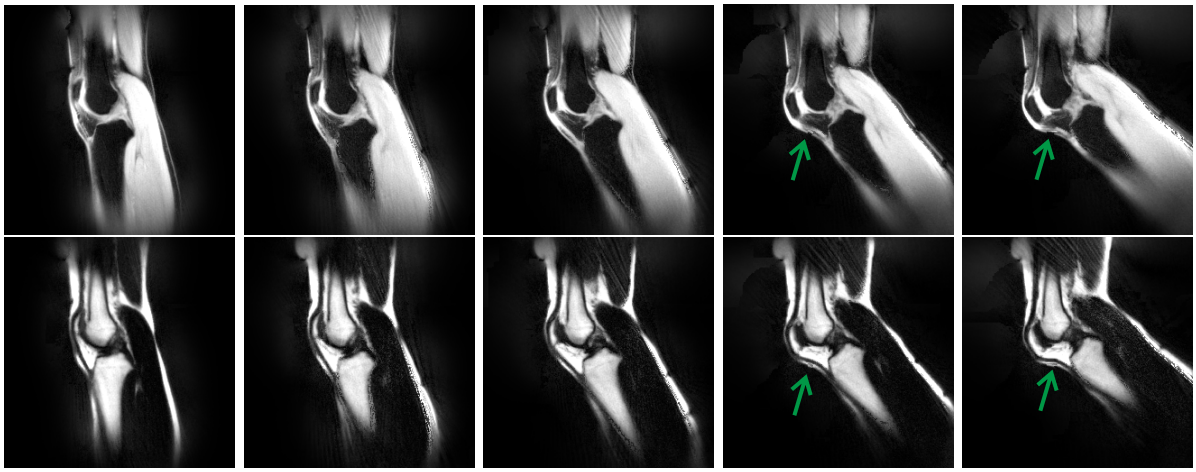

Figure 6.15: 3D ASR water-fat separation. Top row shows water and bottom row shows fat images. The water-fat separation is good, however some areas show water-fat swaps (green arrows).

The approach developed by the author called 3D-ASR and resulting water and fat images yield only a small amount of water-fat swaps if any, see figure 6.15. However, the 3D-ASR water-fat separation is not as robust as the 2.5D-ASR water-fat separation. The distribution of the seed pixels all over the data set without the use of temporal information is problematic and may result in false selection of seed pixels yielding water-fat swaps.

6.4.3 IDEAL

Voxel Independent IDEAL

The IDEAL algorithm proposed in 2004 by Scott B. Reeder [34] is an iterative least-squares estimation method independent of echo time. The signal is modelled as

$$s(t) = \left(\sum_{j=1}^{M} \rho_j \exp\left(2\pi i \Delta f_{\mathrm{w,f}_j} t\right) \right) \exp\left(2\pi i \psi t\right) \tag{6.25}$$

with the chemical shift $\Delta f_{\mathrm{w,f}_j}$ of the chemical species j, of which M different species are present, ρ_j is the spin density of the j-th chemical species, t the time and ψ the field inhomogeneity. If N measurements are made at echo times t_n, N different signal equations are obtained:

$$s_n = s(t_n) = \left(\sum_{j=1}^{M} \rho_j \exp\left(2\pi i \Delta f_{\mathrm{w,f}_j} t_n\right) \right) \exp\left(2\pi i \psi t_n\right) \qquad n \in \{1,\ ...,\ N\} \tag{6.26}$$

In this system of equations are $M+1$ complex unknowns, $\rho_j, j \in \{1, ..., M\}$ and ψ, requiring $N+1$ for exact solution. For example for fat and water $M = 2$ and at least $N = 3$ measurements are required.

The algorithm starts with an initial guess of the field inhomogeneity ψ_0, which allows to remove the contribution of the field inhomogeneity map. The obtained system of linear equations can be solved and an update $\Delta\psi$ for the field inhomogeneity is calculated. The iterative estimation of $\Delta\psi$ is repeated until $\Delta\psi$ is less than a given threshold (e.g. 1Hz) or the maximum number of allowed iterations is exceeded. Finally, an estimate of the chemical species with a smoothed ψ is calculated.

The framewise voxel independent IDEAL with a single fat peak ($M = 2$, $N = 3$) for real-time data works quite well. Exemplary results are shown in figure 6.16.

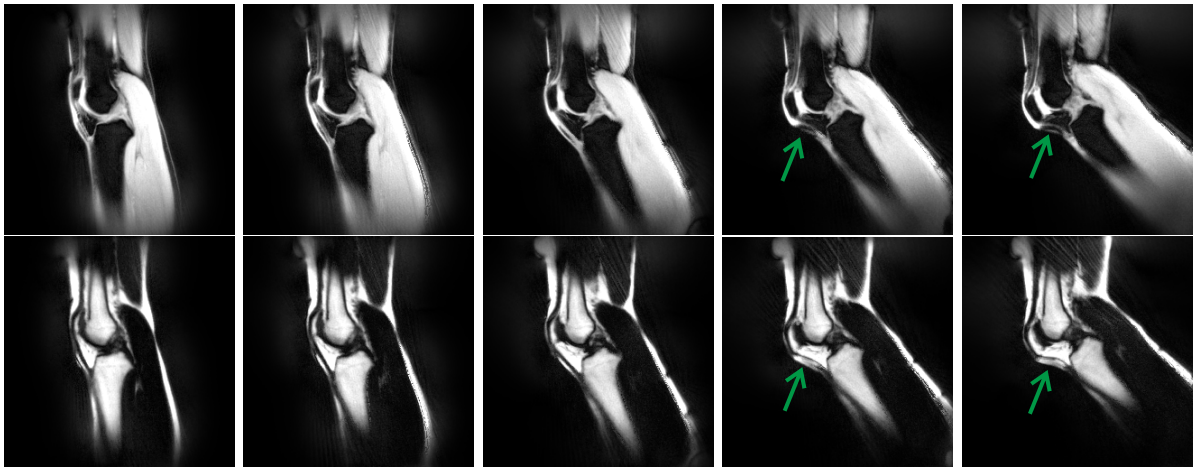

Figure 6.16: Framewise water-fat separation with the voxel independent IDEAL. Top row show water images and the bottom row the fat images.

Multi-peak IDEAL

The multi-peak model was introduced to the IDEAL algorithm by Yu in 2008 [141]. It is a simplification of equation 6.4 without relaxation, but capable of including multiple fat peaks. Inclusion of a multi-peak fat model offers two options for estimating the water and fat amplitudes. First, a pre-calibrated fat model with known relative amplitudes and chemical shifts may be used. The pre-calibrated fat model requires only three echoes to estimate the water and fat amplitudes. Second, a self calibration version which estimates as many peaks as are allowed by the number of acquired echoes, similar to the voxel independent IDEAL. The signal model for both options is

$$S(t) = \left(\rho_w + \rho_f \sum_{j=1}^{M} \alpha_j e^{2\pi i \Delta f_{\mathrm{w,f}_j} t} \right) e^{2\pi i \psi t} \tag{6.27}$$

with water and fat amplitudes ρ_w and ρ_f, M different fat peaks with relative amplitude of the j-th peak α_j and other variables as defined for the voxel independent IDEAL. The relative amplitudes of the fat peaks have as side condition $\sum_{j=1}^{M} \alpha_j = 1$. The extension of the voxel independent IDEAL algorithm is straight forward, the signal equation in matrix notation is

$$S = D(\psi) \cdot A \cdot \rho = \begin{bmatrix} e^{2\pi i \psi t_1} & 0 & \dots & 0 \\ 0 & e^{2\pi i \psi t_2} & \dots & 0 \\ \vdots & \vdots & \ddots & \vdots \\ 0 & 0 & \dots & e^{2\pi i \psi t_k} \end{bmatrix} \cdot \begin{bmatrix} 1 & \sum_{j=1}^{M} \alpha_j e^{2\pi i \Delta f_{\mathrm{w,f}_j} t_1} \\ 1 & \sum_{j=1}^{M} \alpha_j e^{2\pi i \Delta f_{\mathrm{w,f}_j} t_2} \\ \vdots & \vdots \\ 1 & \sum_{j=1}^{M} \alpha_j e^{2\pi i \Delta f_{\mathrm{w,f}_j} t_K} \end{bmatrix} \cdot \begin{bmatrix} \rho_w \\ \rho_f \end{bmatrix} \tag{6.28}$$

Instead of only containing a single exponential term which represents a single fat peak, the second column in the matrix A contains now the weighted sum of individual fat peaks. The system of equations in 6.28 is solved almost exactly as in the IDEAL algorithm.

Second, a self-calibration IDEAL version, which estimates the relative fat amplitudes directly from the measured data may be used. However, this approach requires many echoes to be

measured and is inferior to the pre-calibrated IDEAL version. Relative fat peak amplitudes and chemical shift frequencies for the pre-calibrated IDEAL for different biological tissues are summarized in table 6.5. The peak amplitudes of the fat spectrum vary depending on the measured anatomy, flip angle and repetition time of the FLASH sequence [142–144]. Therefore, it may be advantageous to model the fat spectrum according to the measured anatomy and acquisition parameters. However, the anatomical spectra are very similar and the amplitude changes caused by imaging are small due to the extremely short repetition time and small flip angle. No qualitative difference between the different spectra from table 6.5 were observed in the water-fat separation. A comparison between the single- and multi-peak fat model is shown

Subcutaneous Fat: Yu et al. 2008 [141]						
Chemical Shift / Hz	-472	-420	-318	-234	-46	94
Relative Amplitude	0.06	0.62	0.15	0.03	0.04	0.10
Bone Marror: Ren et al. 2008 [128]						
Chemical Shift / Hz	-430	-381	-345	-264	-200	112
relative Amplitude	0.08	0.55	0.06	0.08	0.14	0.04
Subcutaneous Fat: Ren et al. 2008 [128]						
Chemical Shift / Hz	-430	-381	-345	-264	-200	112
relative Amplitude	0.08	0.62	0.07	0.09	0.06	0.06
Liver Fat: Hamilton et al. 2008 [129]						
Chemical Shift / Hz	-467	-400	-316	-116	-61	-67
relative Amplitude	0.09	0.54	0.17	0.05	0.04	0.10

Table 6.5: Chemical shift frequencies at 3 T and amplitudes of the six major fat peaks.

in figure 6.17, where no qualitative difference is visible. However, a ROI analysis of structures containing fat, shows strongly increased signal intensity in the multi-peak fat map for each ROI as presented in table 6.6. The signal intensity in the water images remained constant, independently of the used fat model. The fourfold signal increase in the fat maps obtained with the multi-peak fat model is also observed in the image noise and caused by convergence into different fieldmap minima. However, the strong increase in fat signal intensity does not lead to an overestimation of fat fraction, instead fat fractions for the analysed regions increase into ranges comparable literature [145].

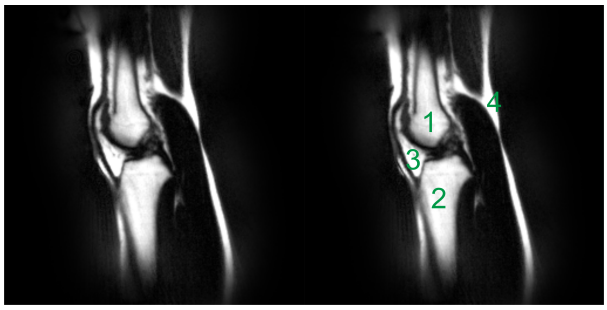

Figure 6.17: Representative fat maps of an IDEAL water-fat separation with usage of the single-peak fat model (left) and the multi-peak fat model (right).

ROI	Single-Peak Fat Model	Multi-Peak Fat Model
Femur(1)	93	350
Tibia(2)	96	360
Fat Pad(3)	107	409
Subcutaneous(4)	130	488

Table 6.6: Signal intensity comparison of lipid rich regions.

Region Growing IDEAL

The water-fat ambiguity appears in IDEAL as different minima to the iterative solution. With an initial guess of the field inhomogeneity, the minimization process is likely to converge into a nearby minimum [26, 27]. Without initial guess ($\psi = 0$) the voxel independent IDEAL converges into a minimum near to 0, which is potentially wrong. To overcome this problem of the pixel independent IDEAL, Yu suggested in 2005 the region growing IDEAL [27].

The region growing IDEAL consists of two steps: first, selecting a starting pixel and second the region growing itself. The starting pixel is selected on a low resolution map and estimated with the voxel independent IDEAL. The field map estimate is then used as initial guess in the voxel independent IDEAL of the corresponding high resolution pixels. The field map is then grown using a square-spiral trajectory, where the next initial value is extrapolated from a weighted linear 2D fit of the already known field map pixels. With this initial value the voxel independent IDEAL is run. The region growing approach ensures a connected field map without jumps which are allowed by the pixel independent IDEAL.

Results for the framewise region growing IDEAL applied to real-time data are shown in figure 6.18. The water-fat separation is superior to the framewise voxel independent IDEAL. However, a frame is completely swapped, but otherwise correctly separated. Besides the water-fat swapped images in the time series, the reconstruction time with the region growing IDEAL for a typical real-time series is about 10 hours.

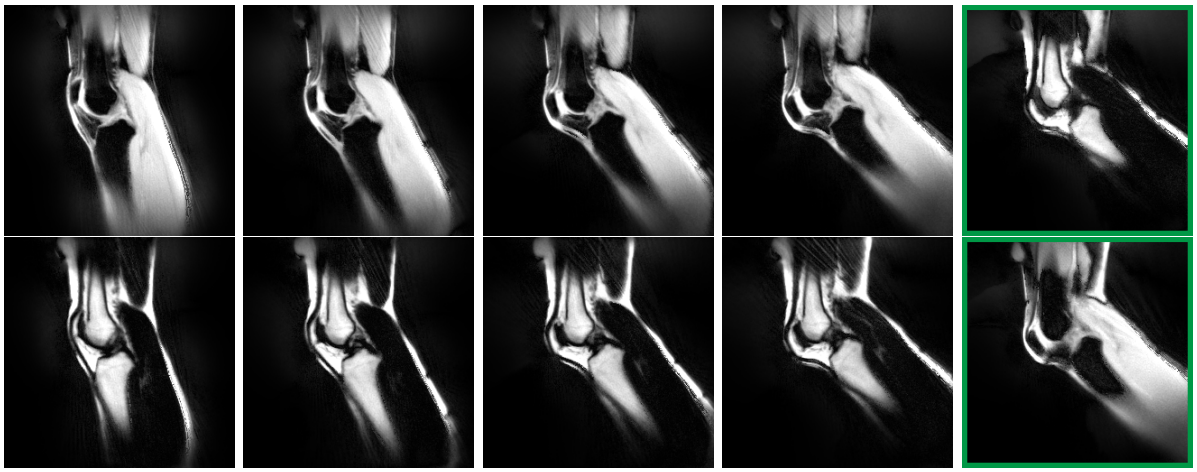

Figure 6.18: Water-fat separation with the framewise region growing IDEAL. Top row show water time series and the bottom row the fat time series. Note the fat frame in the water series and the water frame in the fat series (green frames).

Complex IDEAL

Yu proposed an extension of the the IDEAL algorithm which theoretically is able to additionally estimate the T_2^* [146]. The model from equation 6.25 is extended by a single T_2^* component for water and all fat peaks.

$$s(t) = \left(\rho_w + \rho_f \sum_{j=1}^{M} \alpha_j \exp\left(2\pi i \Delta f_{\mathrm{w,f}_j} t\right) \right) \exp\left(2\pi i \psi t - R_2^* t\right) \tag{6.29}$$

A complex field map $\psi_c = \psi + iR_2^*$ is defined, leaving the signal equation almost the same as for the multi-peak IDEAL, see equation 6.27.

Results of the framewise real-time complex IDEAL are shown in figure 6.19. The water-fat separation works well for the frames with only small field inhomogeneities but fails in the cases for larger field inhomogeneities. The T_2^* map estimation however, does not provide robust results. For the initial frames of the time series where no motion is present negative T_2^* values are estimated outside the object which can be removed by thresholding. At the onset of motion the algorithm fails to converge into a minimum and returns zeros, which are visible as large homogeneous gray areas in T_2^* map of figure 6.19. Without convergence not only the T_2^* estimation but also the water-fat separation fails. The missing convergence may be recovered if more echoes are acquired, prolonging data acquisition.

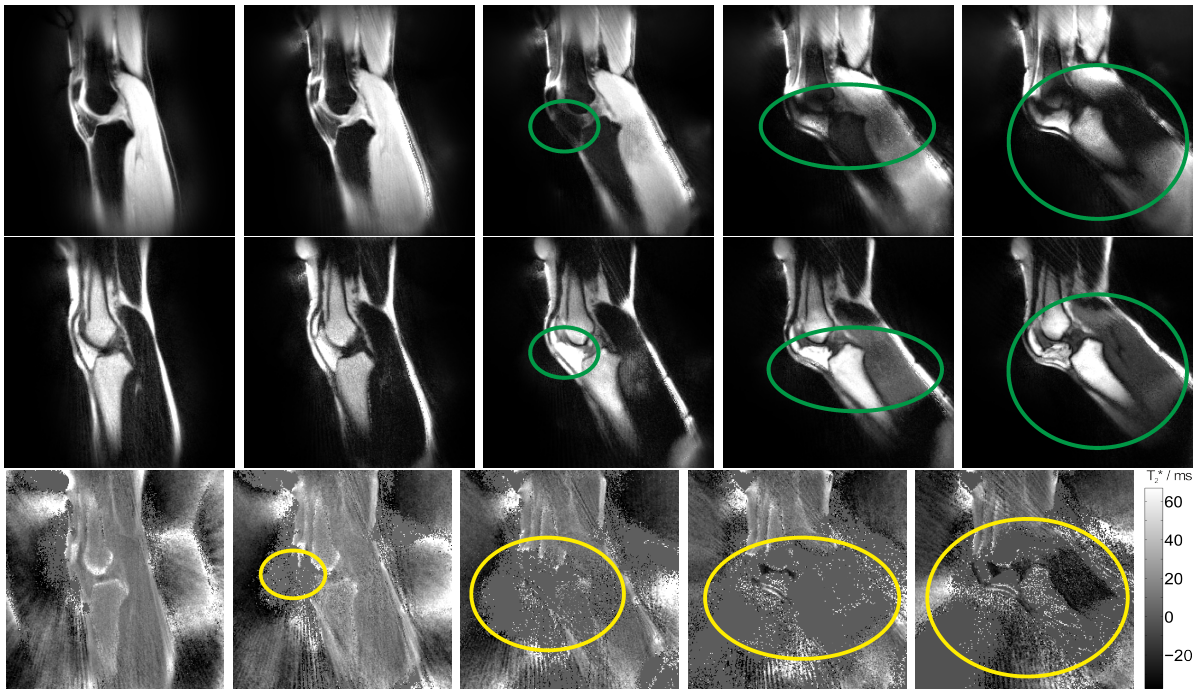

Figure 6.19: Water-fat separation with the complex IDEAL. Water (top row) and fat (middle row) images exhibit was fat swaps (green circles) in areas where the T_2^* (bottom row) estimation converged not or to a false minimum (yellow circles).

Phase-Constrained IDEAL I

The idea was published by Mark Bydder in 2011 [147]. He suggested to constrain the water and fat phase to be the same at time $t = 0\,\text{ms}$ after the RF pulse. To achieve this, a single-peak fat model is used and the known field inhomogeneity is removed from the signal equation.

$$S_n = (W + F \exp(-2\pi i \Delta f t_n)) \qquad n \in \{1, ..., N\} \tag{6.30}$$

The phase-constrained solution for equation 6.30 is

$$x_{\text{pc}} = \text{Re}\left(A^H A\right)^{-1} \text{Re}\left(A^H S \exp(-i\phi)\right) \exp(i\phi) \tag{6.31}$$

with

$$\phi = \frac{1}{2} \arg\left[\left(A^H S\right) \text{Re}\left(A^H A\right)^{-1} \left(A^H S\right)\right] \tag{6.32}$$

Selected frames from a water-fat separated real-time series are displayed in figure 6.20. In the beginning of the measurement, where the field inhomogeneity is not yet large, the water-fat separation works flawlessly. However, as the field inhomogeneity increases water-fat swaps appear in regions of strong field inhomogeneities, see figure 6.20.

For the calculation of x_{pc}, equation 6.31 is not splitted into real and imaginary parts as in the original IDEAL, but uses a complex formulation similar to the complex IDEAL with T_2^* estimation. This increases the computational time per water and fat frame.

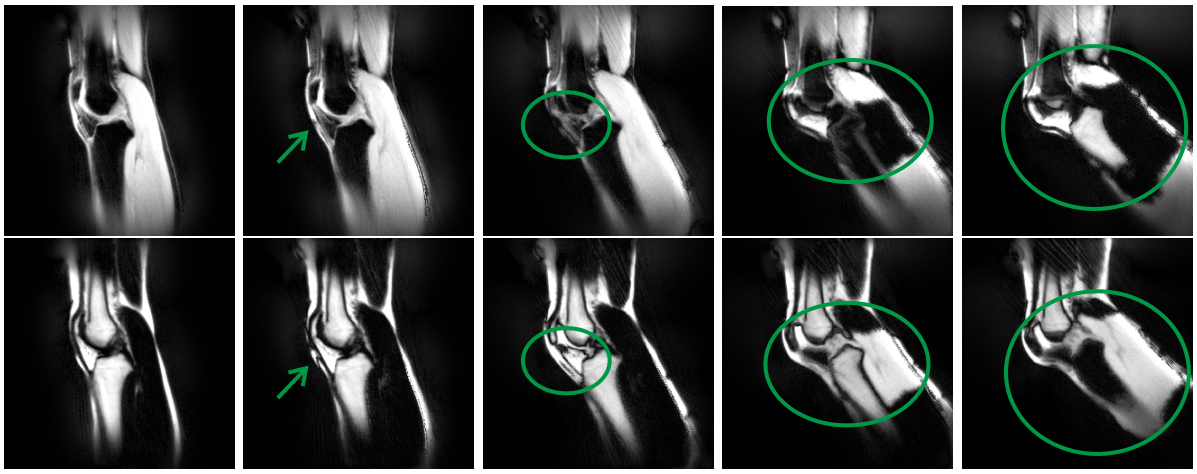

Figure 6.20: Water-fat separation with phase-constrained IDEAL I. Top row shows water images and the bottom row fat images. Water-fat swaps are indicated by green arrows and circles.

Phase-Constrained IDEAL II

This phase-constrained algorithm was published by Yu in 2006 [148] together with Reeder. The original IDEAL algorithm is modified to estimate also the initial phase ϕ_0 with signal model

$$S_n = (W + F\exp(2\pi i\Delta f t + \theta_0 i))\exp(2\pi i\psi t + i\phi_0) \qquad W, F, \psi, \phi_0, \Delta f, t, \theta_0 \in \mathbb{R} \qquad (6.33)$$

The model treats W, F, ψ, ϕ_0 as unknown variables and $\Delta f, t, \theta_0$ as known variables and is solved similarly as the voxel independent IDEAL. The results are shown in figure 6.21, where even at the beginning water-fat swaps are visible. The swaps expand with the increasing field inhomogeneity although the algorithm is provided with an initial guess for the field inhomogeneity map. In addition, the reconstruction time to separate a typical real-time water-fat acquisition is long, questioning the use of phase-constrained IDEAL II in real-time imaging.

6.4.4 Optimized Sequential IDEAL

The optimized sequential IDEAL combines the favourite features of the presented IDEAL variations. Starting with the real region growing IDEAL for the field map estimation of the first frame. Having a robust estimate of the field map the phase-constrained IDEAL I is used to separate water and fat. For the second frame the field map from the previous frame is strongly smoothed and provided as initial guess for the next frame. All successive frames use the real voxel independent IDEAL for the field map estimation due to the fastest reconstruction time. If more than two frames have been separated the initial field map for the next frame is extrapolated from previous field maps. If available, the last 5 frames are used for the extrapolation. The water-fat separation for all frames is done with the phase-constrained IDEAL after the field map has been estimated.

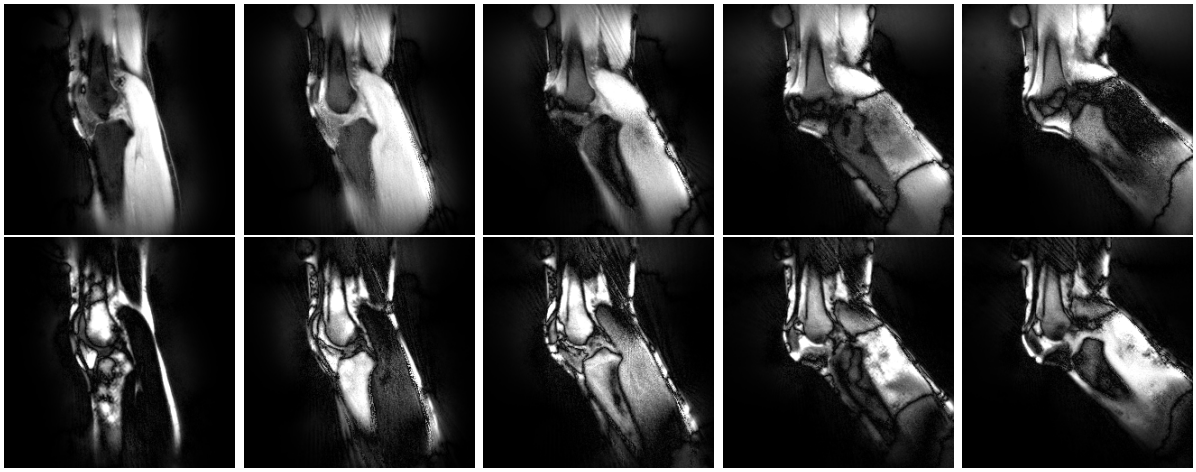

Figure 6.21: Water-fat separation with the phase-constrained IDEAL II. Both water (top row) and fat (bottom row) exhibit severe water-fat swaps.

The results of the sequential IDEAL are displayed in figure 6.22. They show excellent water-fat separation even in difficult situations with a changing and strongly inhomogeneous field map. The reconstruction time is reasonably fast with 1-4 seconds per frame for the C implementation, except for the first frame, where the region growing IDEAL slows down the water-fat separation.

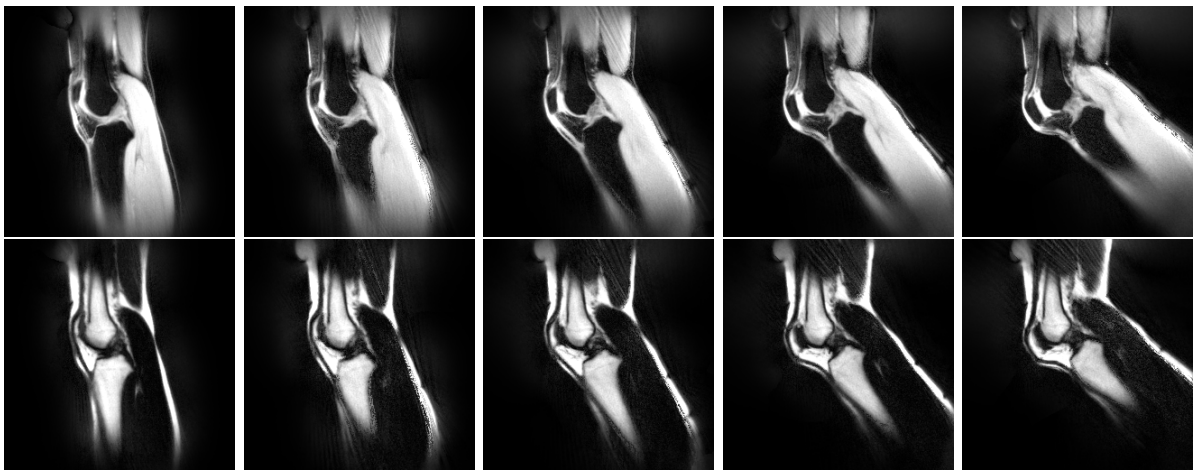

Figure 6.22: Water-fat separation with the optimized sequential IDEAL. Top row show water images and the bottom row the fat images.

6.5 Single-Echo Methods

Instead of using multiple images for water-fat separation, methods using a single image have also been developed [37, 148, 149]. These one-point methods use a single-peak fat model and data is acquired at an echo time t_{E} where the phase between water and fat is $\pi/2$.

6.5.1 Quadrature Sampling

Sampling water and fat with a phase difference of $\pi/2$ is called quadrature sampling [37]. The signal equation is

$$S(t_E) = (W + iF)\, e^{2\pi i \psi t_E} \tag{6.34}$$

A small exponent in equation 6.34 can be neglected, yielding water as real and fat as imaginary part of the reconstructed complex image. The exponent is small, if the product between the echo time t_E and the field inhomogeneity ψ is small. However, the echo time is limited to the quadrature sampling values

$$2\pi\Delta f_\mathrm{fw} t = \pi/2 \cdot (2n-1) \qquad n \in \mathbb{N}. \tag{6.35}$$

with the three shortest echo times given in table 6.7.

n	1	2	3
Echo Time / ms	0.61	1.82	3.03
$2\pi\Delta f_\mathrm{fw} t$	$\frac{\pi}{2}$	$\frac{3}{2}\pi$	$\frac{5}{2}\pi$

Table 6.7: The three shortest possible quadrature sampling echo times at water-fat frequency difference of $\Delta f_\mathrm{wf} = 412\,\mathrm{Hz}$ (3 T)

Due to the periodicity of the complex exponential function in equation 6.34 any echo time fulfilling the quadrature sampling condition 6.35 is possible. However, with increasing echo time even small values of the field inhomogeneity map lead to water-fat swaps, because water and fat are rotated away from the real and imaginary axes. Besides the possible water-fat swaps the signal decays with T_2^* leading to a loss of signal intensity for late echo times.

Results for the quadrature sampling water-fat separation at echo time TE=3.03 ms with disregard of the field inhomogeneity map are shown in figure 6.23. The quality of the water-fat separation is poor, because of the disregarded field inhomogeneity map. In regions with low field inhomogeneity values, like the posterior part of the brain, the water-fat separation works better than in regions with high field inhomogeneity values, e.g. around the eyes.

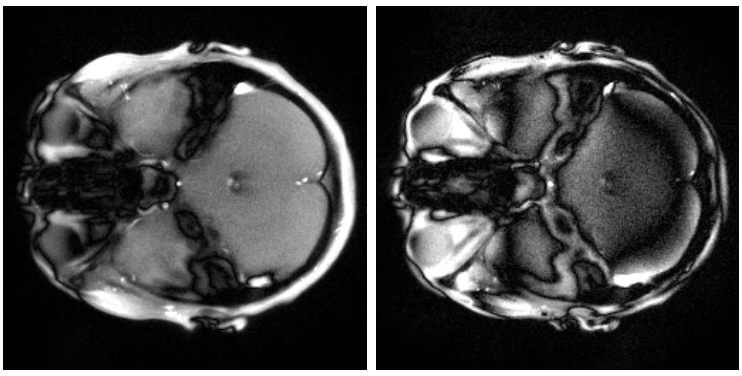

Figure 6.23: Quadrature water-fat separation without calculating a field inhomogeneity map. The left image shows water and the right image fat.

6.5.2 1-Point Plus Separation

The idea of the 1-Point Plus Separation was published by Yu in 2006 for the use of breast imaging with contrast agents [148]. He proposed to use the 'Iterative Phase-Constrained IDEAL' (see

section 6.4.3, [34, 148]) to estimate iteratively the field inhomogeneity map and the initial phase of water and fat magnetization from a preparatory multi-echo measurement and subsequently apply the field map and the initial phase on a single-echo measurement acquired in quadrature.

The description of the water and fat signals for the initial phase-constrained model with four unknown variables according to [148] is

$$S_n = (|W| + |F| \exp(2\pi i \Delta f t_n)) \exp(2\pi i \psi + i\phi_0) \qquad |W|, |F|, \phi_0, \psi \in \mathbb{R} \tag{6.36}$$

with the water and fat phase ϕ_W and ϕ_F at the time $t = 0$ after the RF pulse approximately $\phi_W = \phi_F = \phi_0$. If the field inhomogeneity map and initial phase are known and removed from the data, only water and fat remain. This is true for the multi-echo measurements as well as for the single-echo measurements. It is then possible to separate water and fat from a single-echo acquisition, if they have been acquired in quadrature. In this case water is the real and fat the imaginary part of the demodulated data. Applying this method to real-time data, a further assumption must be made: The field inhomogeneity map must be constant over time.

Single-echo measurements with echo time TE=1.78 ms and 47 spokes have been acquired and reconstructed. However, the estimation of the initial phase ϕ_0 from the multi-echo measurement failed for the in-vivo measurements of the abdomen and only poorly water-fat separated images have been generated, see figure 6.24. Additionally, motion in the images is accompanied by a change of the field inhomogeneity map, violating the constant field inhomogeneity map assumption.

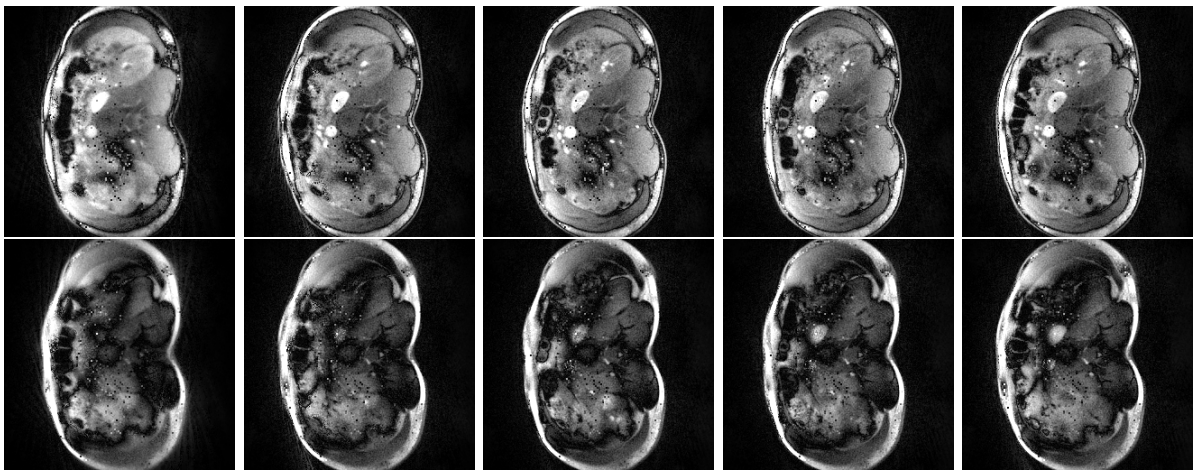

Figure 6.24: Single echo water-fat separation with the use of a previously estimated field map and initial phase. Note the inhomogeneous water-fat separation in each frame.

6.6 Fat Quantification

The fat fraction with water W and F signals is calculated according to

$$\eta_F = \frac{|F|}{|W| + |F|} \tag{6.37}$$

and has become an important alternative to spectroscopy or biopsy in the detection of liver diseases [22]. However, for proper fat quantification with MRI, the following confounding factors must be considered and corrected [22].

- Spectral Complexity:
  The proton MR spectrum of fat has been measured accurately in humans and consists of more than only the methylene peak [128, 129]. Therefore proper fat quantification must account for this spectral complexity, see e.g. equation 6.4 as suggested by Yu [141].
  Reeder showed that both single-peak and multi-peak water-fat separations correlate with magnetic resonance spectroscopy, however, the use of a pre-calibrated multi-peak fat model had the highest correlation [140]. Similar result have been found by Guiu [150] with a three-point Dixon water-fat separation method and correction for T_1, T_2 and T_2*.

- T_1 bias
  'T_1 weighted sequences lead to an overestimation of fat due to the short T_1 values of fat compared to water' [151], which was demonstrated by Liu and Bydder [152, 153]. They removed T_1 bias by acquiring the images with a flip angle of less than 5°. Instead of using a low flip angle, the use of a long T_R is also possible [153]. If none of the previous methods is applicable, the T_1 bias can be corrected by including T_1 relaxation in the model [153] or by using a dual flip angle approach, which weights the water and fat signal according to the flip angle [152].

- T_2^* decay:
  The signal in multi-echo gradient-refocused imaging decays with T_2^* and the change in signal intensity over the echoes alters the water-fat separation if not accounted for. The T_2^* decay can be included into the model by assuming a complex field map $\psi = \Delta B_0 + iR_2^*$ as suggested by Yu et al [141, 146] for the complex IDEAL. For a magnitude fitting model Bydder et al included the T_2^* decay into the model [153] and showed that a system with multiple peaks appears at low spectral resolution like a two component system with shortened effective T_2^*. Instead of including T_2^* decay, measuring T_2^* and correcting the acquired images is also possible. Mostly, a combined T_2^* for water and fat is assumed, but not necessarily needed [154, 155].

- Noise Bias:
  The noise bias occurs with the magnitude operation on the water and fat maps. Noise in the complex images is Gaussian with zero mean and changes to a positive non-zero value after the magnitude operation. Especially at low and high fat fractions noise bias is evident [22, 152]. The noise bias can be removed with a magnitude discrimination after initial water fat separation or with a phase-constrained water-fat separation method [152].

- Eddy Currents:
  Eddy currents affect the phase of the acquired images. Performing magnitude water-fat separation, these effects are naturally avoided [156, 157]. However, in general only the phase of the first echo is corrupted and neglecting its phase by using a mixed magnitude/complex water-fat separation method avoids this bias [156, 157].

The influence of these confounding factors onto the fat fraction estimation has been evaluated in great detail in phantoms e.g. [151] as well as in volunteers e.g. [158, 159] and all of them can be corrected for accurate fat quantification. With regard to real-time imaging, almost all confounding factor can be removed.

Except for DPE, all three-point water-fat separation methods are capable of using a multi-peak fat model and thereby removing this confounding factor. T_1 can effectively be removed with the use of flip angles with less than 5°, which is easily achieved with the FLASH sequence. The noise bias is taken care of by the phase-constrained water-fat reconstructions. For sequential imaging, the field inhomogeneity map is estimated without the phase constraint and for the

final water-fat separation the phase-constraint is applied. The T_2^* and eddy current bias are more difficult to account for. With only three echoes the T_2^* estimation is not very accurate or even fails. Acquiring more echoes prolongs the data acquisition time and therefore reduces the temporal resolution and degrades the water-fat separation quality in the case of fast motion. Magnitude or mixed magnitude/complex water-fat separation have been not been investigated, leaving the eddy current effect on the fat fraction map uncorrected in fast water-fat imaging.

Results of free breathing abdominal real-time water-fat separation with fat-fraction maps are displayed in figure 6.25. As visible in the fat fraction maps, this volunteer does not have suspicious fat deposition in the liver.

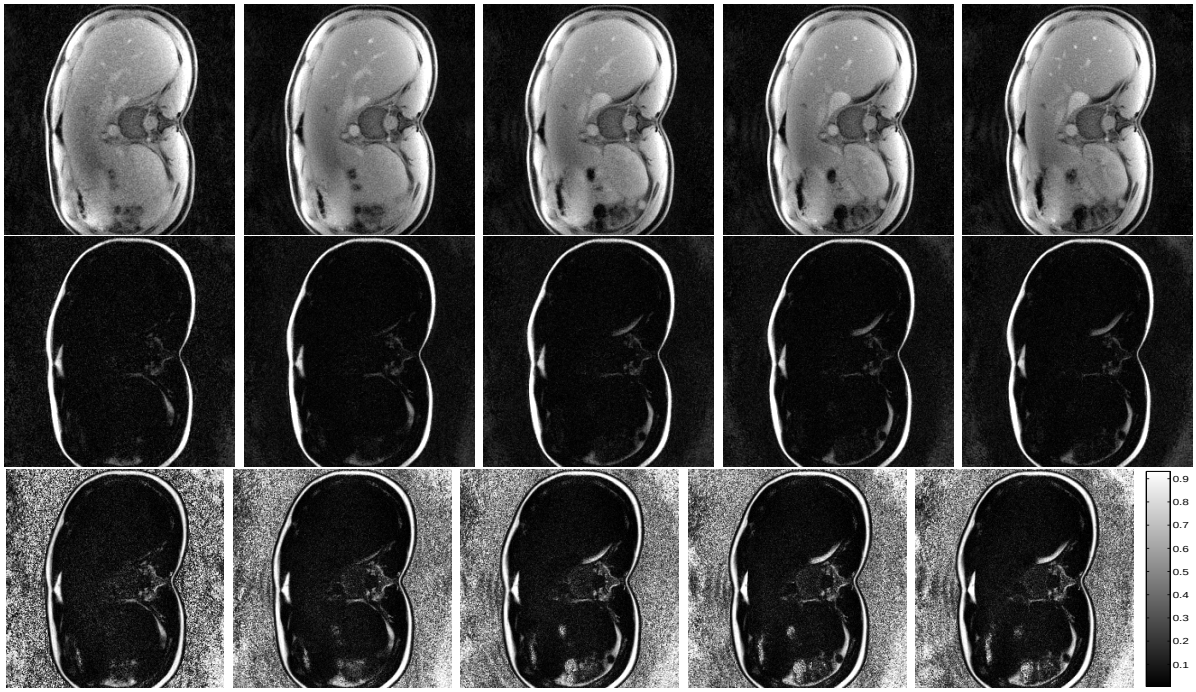

Figure 6.25: IDEAL Phase constrained water (top row) and fat (middle row) separated time series and the corresponding fat fraction maps (bottom row). The colorbar indicates the fat fraction with zero (black) and 100% (white).

6.7 Spatial and Temporal Resolution

The achievable spatial and temporal resolution and possible degree of undersampling for water-fat separation in real-time has been investigated with knee measurements. The knee is a challenging anatomy for water-fat separation in real-time due to strong field inhomogeneities and large motion, as well as the necessity of high-resolution images. In figures 6.26 (water) and 6.27 (fat) the results for a knee measurement with $1.0\,\mathrm{mm}^2$ in-plane resolution and different number of acquired spokes are displayed. For each data several image reconstructions with NLINV Newton steps ranging from 5 to 11 and succeeding water-fat separations have been performed. The sharpness of the reconstructed images increases with the number of Newton steps, as does noise. Depending on the degree of undersampling (number of spokes) the reconstructed images are increasingly contaminated with noise. Image reconstructions with 11 Newton steps exhibit even for acquisitions with 125 spokes strong noise. However, independent of the Newton steps, noise or the number of acquired spokes, the water-fat separation is flawless with these acquisition and reconstruction parameters.

The measurements with 0.75 mm^2 in-plane resolution show a different behavior. Water-fat separations from NLINV reconstructions with any odd number of Newton steps show water-fat swaps. Five and six Newton steps produce blurry images which do not reflect the measured in-plane resolution. Artifact free water-fat separations are obtained from image reconstructions with 8 and sometimes with 10 Newton steps. The presence of increased noise in the images with 10 Newton steps favors water-fat separation on images reconstructed with 8 Newton steps. However, with 15 spokes minor water-fat swaps appear, indicating the declined robustness of the field map estimation at extreme undersampling combined with high in-plane resolution.

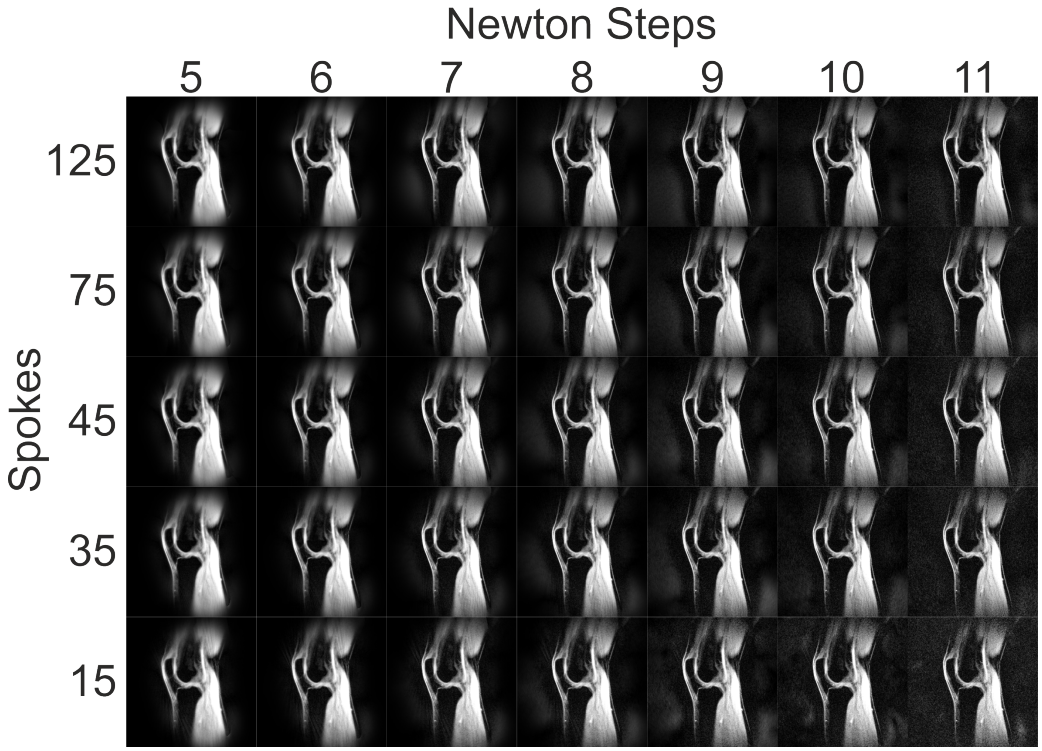

Figure 6.26: Water images from optimized sequential IDEAL water-fat separated time series at an in-plane resolution of 1.0 mm^2.

A comparison for different bending speeds of the knee was performed for a volunteer with an in-plane resolution of 0.75 mm^2. Shortest possible echo times have been selected and acquisition times of 1000, 500 and 250 ms per frame corresponding to 151, 75 and 37 spokes per frame.

The results are presented in figures 6.31, 6.30 and show that with faster acquisition times the images regain sharpness, especially for faster motions. However, faster acquisitions require higher undersampling which leads to increased streaking artefacts and noise. The highly undersampled images with 37 spokes show the same details as the acquisition with more spokes. In conclusion, data acquired with 37 spokes and reconstructed with 8 Newton steps captures motion sufficiently fast without loss of image detail and avoids water-fat swaps from the reconstruction.

With an extreme undersampling of only 13 spokes real-time water-fat images at a temporal resolution of about 51 ms of the human heart have been acquired. Results are presented in figure 6.32. The water-fat separation was artefact free independent of the Newton steps. However, an increase from 6 to more Newton steps did not improve the image quality, nor is it needed to reveal image details at an in-plane resolution of 2 mm. Due to the temporal resolution of 51 ms the systolic phase is not accurately resolved, but the hyper-intense subcutaneous fat could be removed from the water images yielding a more homogeneous image. Also due to the combination of three images for the water and fat maps, they exhibit less noise than the original individual

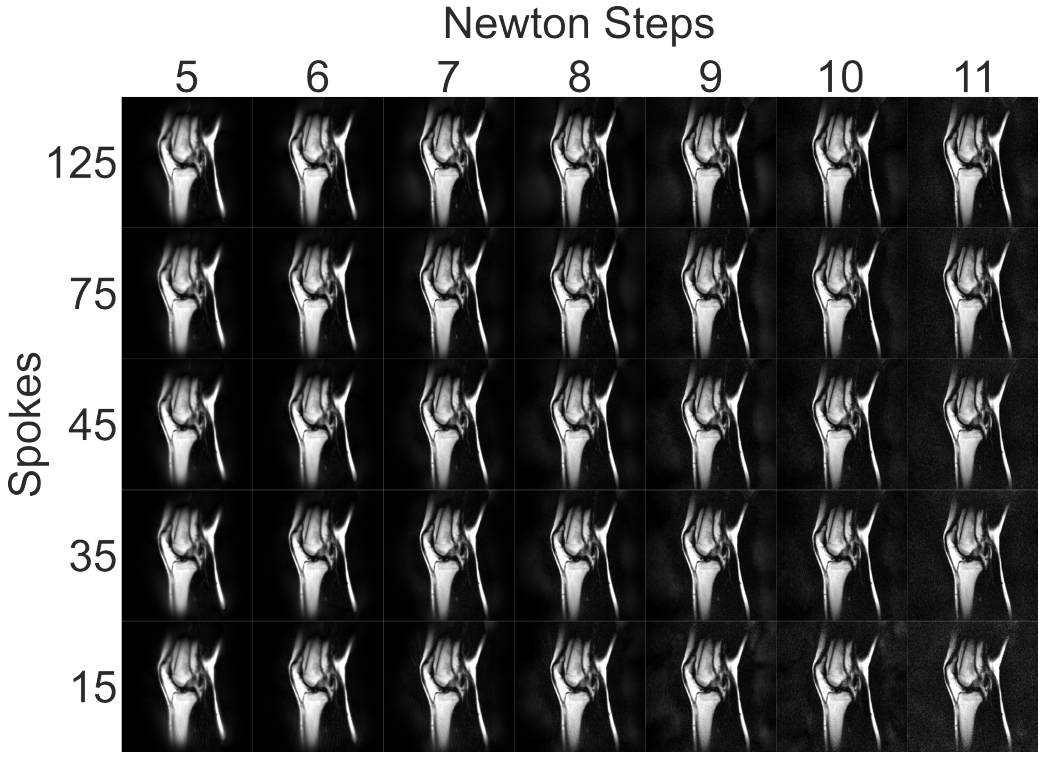

Figure 6.27: Fat images from optimized sequential IDEAL water-fat separated time series at an in-plane resolution of $1.0\,\mathrm{mm}^2$.

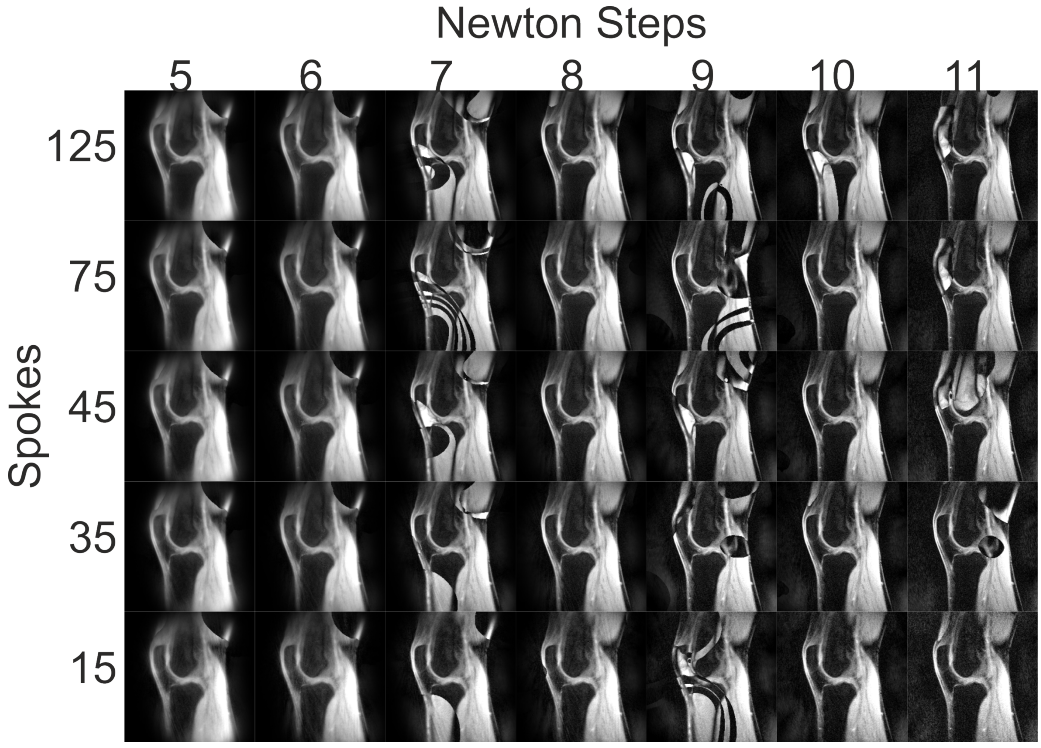

Figure 6.28: Water images from optimized sequential IDEAL water-fat separated time series at an in-plane resolution of $0.75\,\mathrm{mm}^2$.

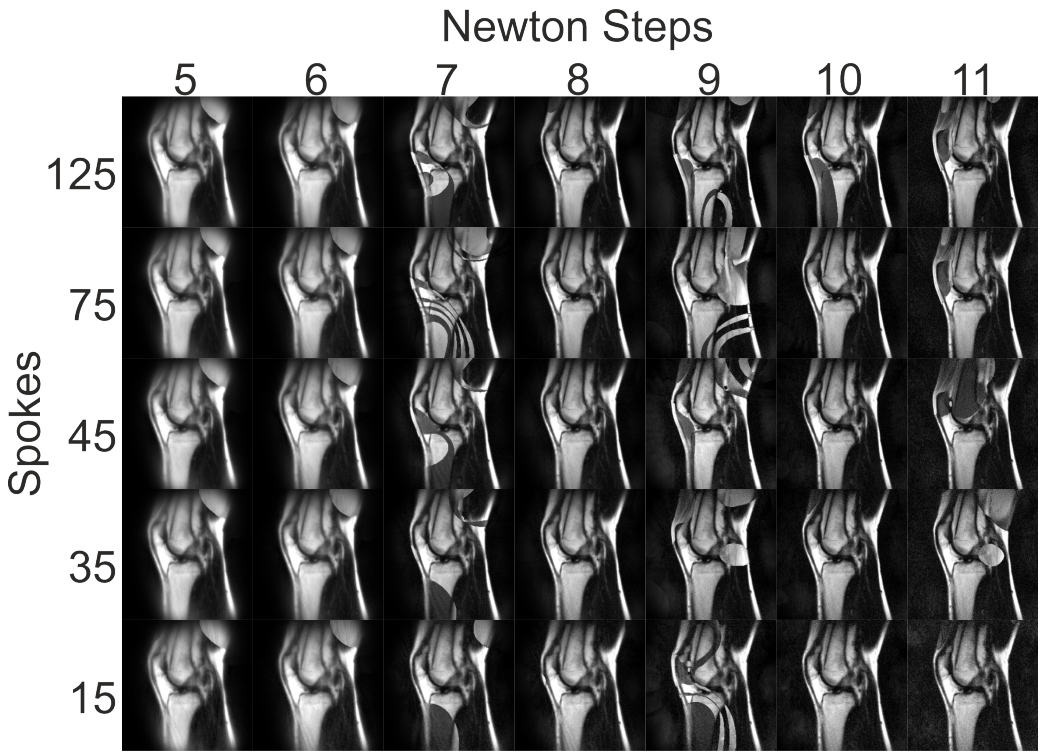

Figure 6.29: Fat images from optimized sequential IDEAL water-fat separated time series at an in-plane resolution of 0.75 mm^2.

echo acquisitions.

Water-fat separation on real-time data has also been tested on the abdomen. Measurement parameters include in-plane resolutions of 1.50, 1.00, 0.75 mm^2 at fastest possible echo times, 31-37 spokes yielding a temporal resolution of about 200 ms. Results are presented in figure 6.33. With increasing in-plane resolution the number of Newton steps was also increased from 6 to 8 to keep the sharpness constant. However, noise increased due to decreasing voxel size and increasing Newton steps. The water-fat separation was successful despite the increasing noise, only some gas bubbles in the gastrointestinal tract produced minor swap artefacts at the bubble borders (green arrow) at in-plane resolutions of 0.75 mm^2.

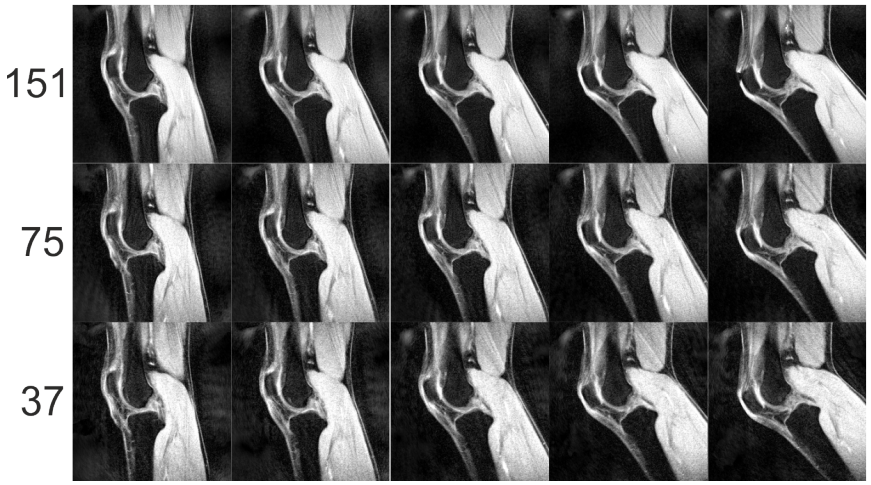

(a) slow motion

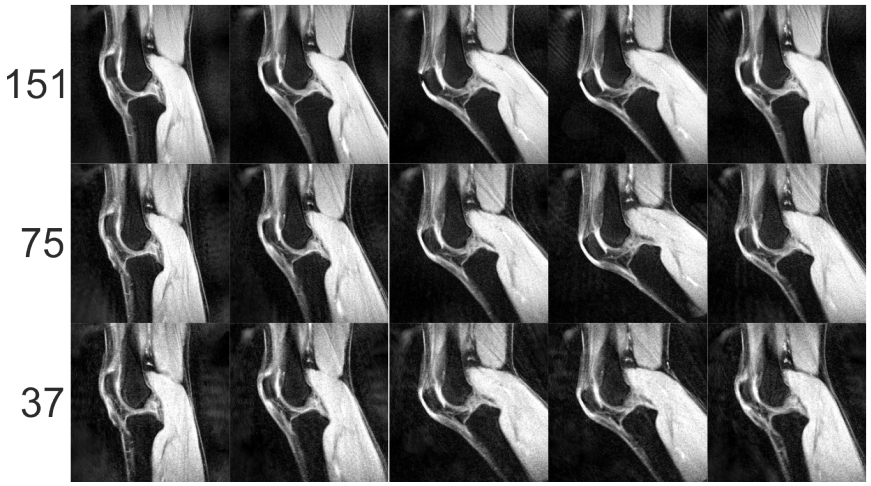

(b) medium motion

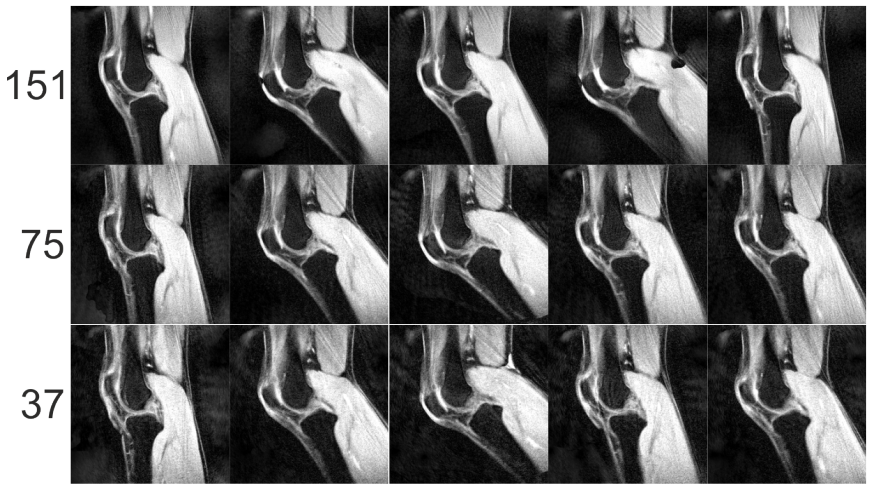

(c) fast motion

Figure 6.30: Water images after optimized sequential IDEAL water-fat separation with different bending speeds of the knee, acquired with different number of spokes (number on the left).

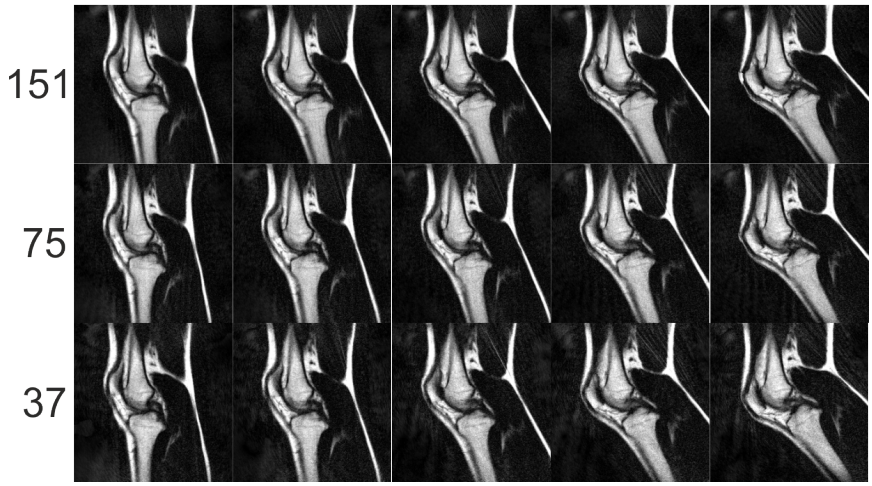

(a) slow motion

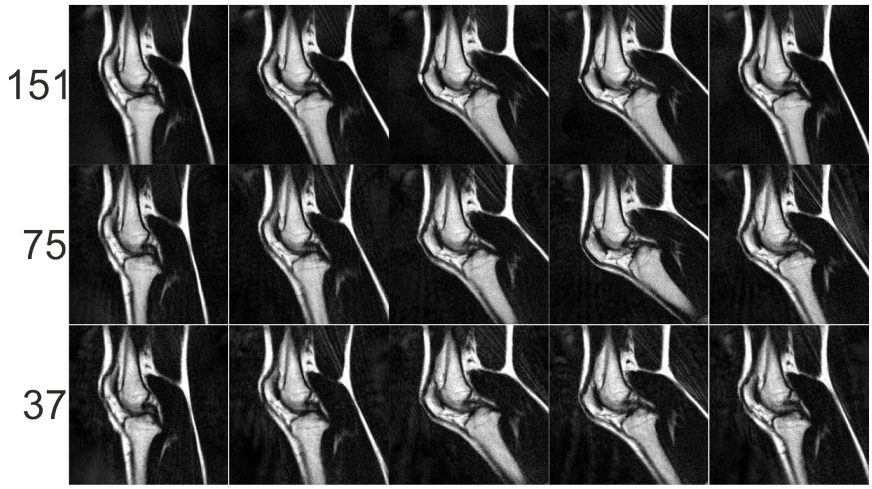

(b) medium motion

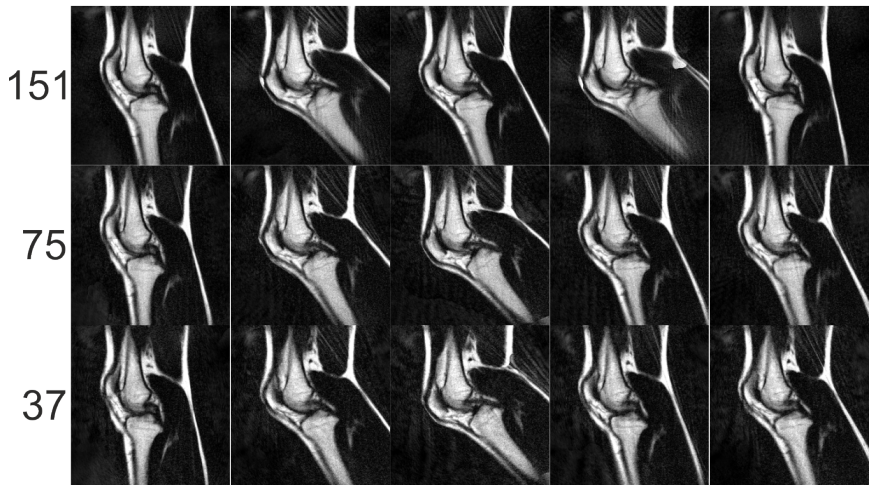

(c) fast motion

Figure 6.31: Fat images with optimized sequential IDEAL water-fat separation for different bending speeds of the knee, acquired with different number of spokes (number on the left).

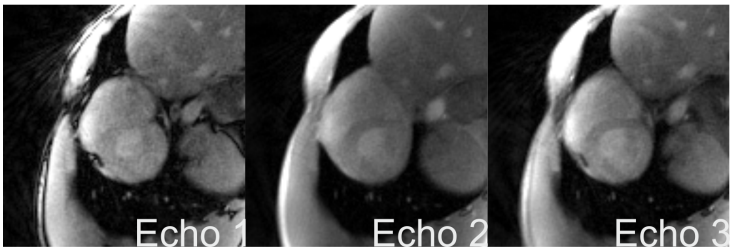

(a) Single Multi-Echo Frame

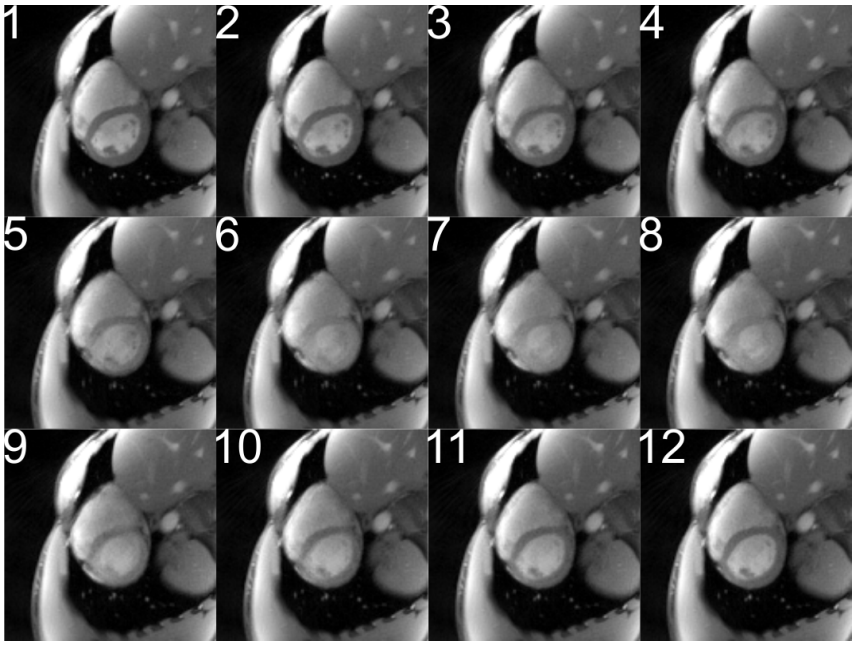

(b) Water

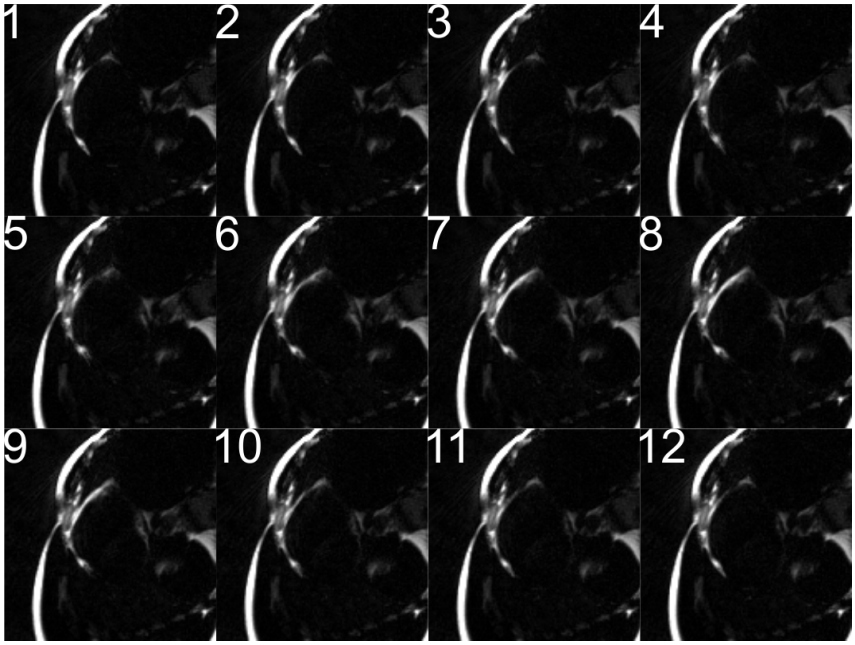

(c) Fat

Figure 6.32: Representative heartbeat from a water-fat separated real-time series.

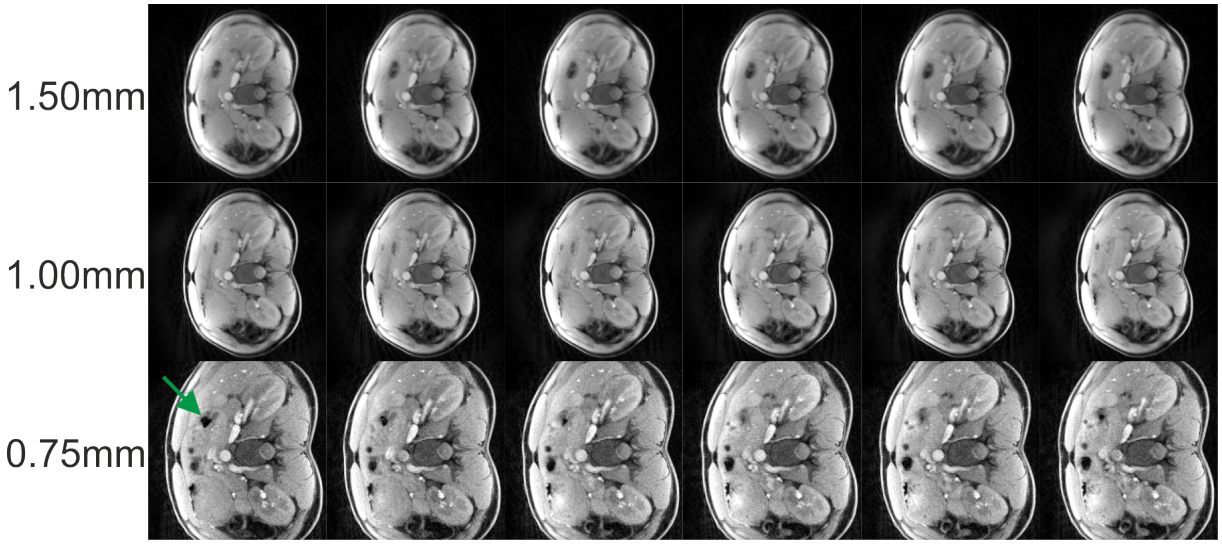

(a) Water

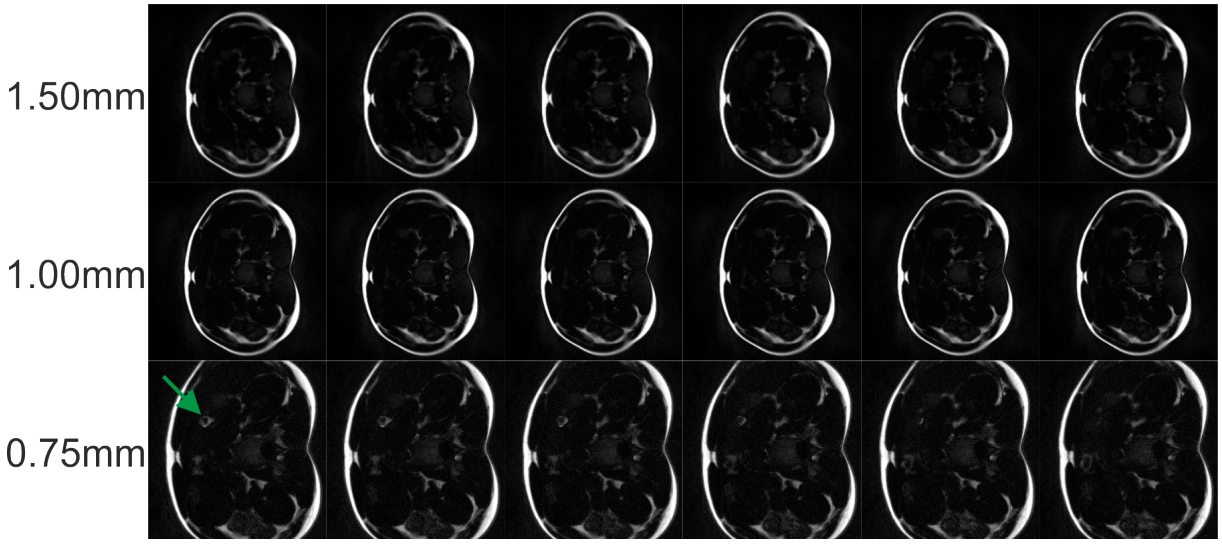

(b) Fat

Figure 6.33: Sequential frames from an abdominal real-time water-fat separated time series with 45 spokes yielding 270 ms per frame. Gas bubbles lead to incorrect water-fat separation (arrow).

6.8 Results at 7 Tesla

Several measurements at a 7 T scanner in Magdeburg have been performed, including the saturation pulses approach and data for the echo-time independent multi-echo water-fat separation.

The saturation of water or fat works quite well due to the increased T_1 relaxation times of fat and water at higher field strengths [160], see figure 6.34. However, the water saturated images exhibit stronger blurring than the fat saturated or unsaturated images. The acquisition parameters for a real-time saturation measurement include in-plane resolution of $0.75\,\mathrm{mm}^2$, echo time TE=1.68 ms, repetition time TR=2.78 ms and 25 spokes yielding a temporal resolution of 75 ms per frame.

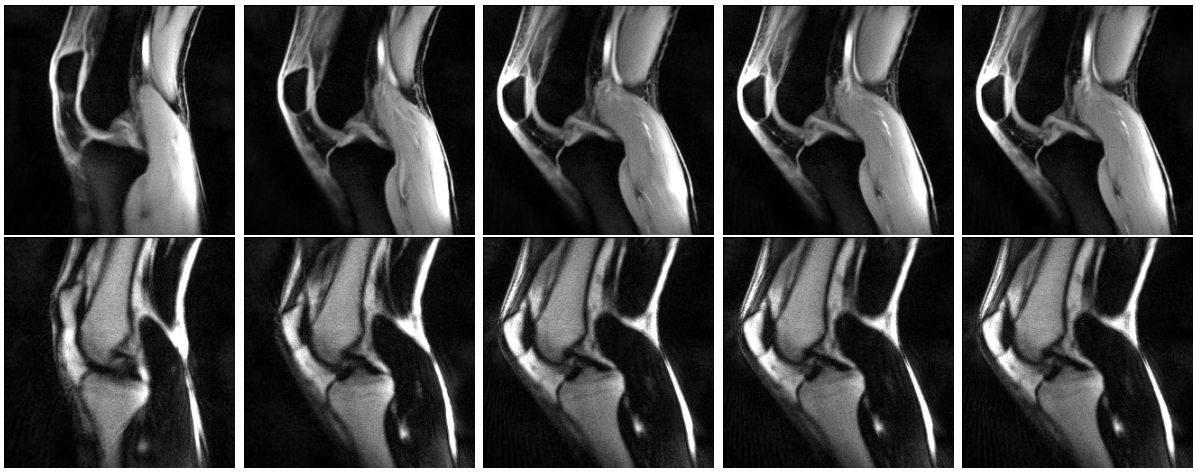

Figure 6.34: Real-time water (top row) and fat (bottom row) suppression at 7 T.

The three-point water-fat separation methods operating successful on real-time data at 3 T like DPE, ASR and IDEAL failed to produce swap free water and fat separated images at 7 T. The failure is due to the false estimation of the field inhomogeneity map/phasor which is due to the stronger field inhomogeneities and faster T_2^* decay at 7 T.

6.9 Discussion

Water-fat separation on real-time data reconstructed with NLINV was explored using conventional saturation pulses between frames as well as Dixon water-fat and advanced separation methods like DPE, ASR and IDEAL.

The effect of the saturation pulses depends strongly on the T_1 relaxation time of the tissue, favoring water over fat saturation due to the longer T_1 of water. At 3 T short acquisition times ($<$100 ms) for each image and a very good shim led to successful water/fat saturation.

Using saturation pulses and the signal recovery, a completely new water-fat separation method based on correlation between each pixel time series and the saturation pattern was developed. The quality of the correlation water-fat separation method depends on the quality of the saturation pulses and the length of the data acquisition. However, this method is not suitable for real-time water-fat separation because only a single water or fat image is obtained from the whole time series. Furthermore, motion of the object requires pixel tracking before the time series can be correlated to the saturation paradigm. Correlation separation may be favorable if one is interested in either water or fat images.

The Dixon water-fat separation algorithms are simple and fast. However, with regard to fast imaging the fixed echo times reduce the possible applications, since the usable temporal and/or

spatial resolution is restricted. Also, to separate water and fat compartments successfully, the field map must be estimated correctly, which most likely involves phase unwrapping. A simple temporal phase unwrapping approach has been implemented, yielding swap free water and fat images, as long as the first frame is free of spatial phase-wraps and each pixel time series no interrupted by noise.

The echo-time independent methods DPE, ASR and IDEAL are well suited for water-fat separation. However, the reconstruction time for DPE is quite long, rendering DPE unfavorable for fast water-fat separation despite the artefact free separation quality. Furthermore, DPE loses its ability to successfully separate water and fat with the introduction of the multi-peak fat model. The ASR and IDEAL algorithms are faster, ASR has already suitable reconstruction time for real-time display of water and fat images. The current optimized sequential IDEAL implementation needs 1-4 seconds per frame for the water-fat separation, excluding the first frame where the region growing slows down the field map estimation. Such a reconstruction time is not fast enough for displaying water and fat maps in real-time, however, the problem is easily parallelized and ported to GPUs where the necessary speed-up can be achieved [161]. At the current state the optimized sequential IDEAL emerges the most suitable method for real-time water-fat separation, because it allows to correct for all confounding factors easier than the other examined methods. However, proper estimation of the T_2^* requires more than three echoes, in practice at least 6 [146], prolonging the measurement and increasing the acquisition time. But having more echoes available the estimation of the field map becomes more robust. For most measurements the rt-IDEAL and ASR algorithms were able to obtain water and fat images of good quality and showed a quite robust reconstruction behavior. However, in some cases the water-fat separation fails and water-fat swaps in few temporally connected frames and small areas containing only few pixels deteriorate the water and fat maps. The phase-constrained IDEAL I works better than the iterative estimation of the initial phase (phase-constrained IDEAL II) and is necessary for quantitative fat maps. Complex water and fat images may allow for access to additional parameters encoded in phase, such as temperature or velocity.

The optimized sequential IDEAL was tested on various anatomies, including the knee, heart and abdomen. For the knee, limitations of the water-fat separation have been evaluated. Increased undersampling does not lead to a loss in image quality but improved capturing of motion. Higher in-plane resolution shows increased noise because more Newton steps are needed to reveal the measured in-plane resolution. This was already demonstrated by Uecker in his thesis [7] and holds true together with water-fat separation. The water-fat separations for NLINV image reconstructions with different Newton steps show that for high-resolution images only 8 Newton steps lead to proper water-fat separation. This effect is confined to the high-resolution knee image reconstructions, for the other measured parts of the body no failure of the rt-IDEAL water-fat reconstruction was observed independent of the number of Newton steps.

Real-time imaging requires fast image acquisition to freeze the imaged object and reconstruct it correctly [59], which is even more challenging for real-time water-fat acquisitions due to the necessity of multiple echoes. However, good water and fat maps are obtained for relatively fast moving objects with a variety of temporal resolutions. On the other hand, images of moving objects are unable to resolve the same details as static data acquisitions, which is caused by the prolonged acquisition, where small details change from one spoke to the next and therefore cannot be reconstructed properly. With lower in-plane resolution this effect is reduced as shown for the cardiac data and abdominal data.

The fastest water-fat separation methods are single-point methods, but here no correct water-fat separation could be achieved, because of the false estimation of field inhomogeneity maps or because of the incorrect assumption of a temporally constant field inhomogeneity map in case of the 1-Point plus separation.

At 7 Tesla, where T_1 is increased and the saturation holds longer, complete water and fat saturation was achieved. With regard to real-time water-fat separation at 7 T, saturation is the favorable method, because the advanced echo-time independent water-fat separation methods failed at 7 T.

In principle, not only water and fat can be separated, but any chemical species. This was demonstrated with an ethanol phantom and for water, fat and silicone separation in a volunteer by An in 2001 [162] and for C^{13} imaging by Reeder et al [163]. The findings for water-fat separation should be easily transferred to separation of arbitrary chemical species acquired with fast imaging methods.

6.10 Conclusion

Real-time water-fat separation is feasible, not only with respect to the data acquisition but also with respect to the image reconstruction and water-fat separation. For data from a 3 T scanner, two successful approaches were found, one approach employs saturation pulses between every frame and the other approach uses an echo-time independent multi-point acquisition (three echoes) and advanced water-fat separation algorithms. The 2.5D ASR algorithm has a reconstruction time suitable for real-time display, but cannot correct for most confounding factors for fat quantification. The optimized sequential IDEAL on the other hand can correct for almost all confounding facts, but must be implemented on GPUs to enable the display of water and fat frames in real-time. For data from a 7 T scanner, only the saturation pulses provided successful water-fat separation. Furthermore, model-based approaches may allow to accurately estimate T_2^* with only three echoes, enabling even more accurate fat quantification in real-time or more robust water-fat separation.

Chapter 7

Phase-Contrast Flow MRI Phase Unwrapping

MRI acquires complex data in k-space and most image reconstructions yield complex images. The magnitude represents the proton density weighted with the coils and object specific relaxation properties. Examples for information encoded in the phase are phase-contrast imaging, where the velocity is encoded into the phase [51], or thermometry, where the proton resonance frequency changes with temperature [164]. Since water and fat protons have slightly different resonance frequencies their signal intensities interfere, which is visible in in-phase and opposed-phase images. The extraction of values from the phase may be difficult because values can only be determined within the interval of $I = [-\pi, \pi]$ modulus 2π. Any value exceeding the phase interval of I in any direction is wrapped back into I, thereby alterating the extracted values. Another problem are points where the phase circles around, so called phase poles. Phase wraps can sometimes be resolved if the phase is sampled accordingly well, but phase poles are a fundamental problem which cannot be unwrapped. Typically phase poles occur for complex flow patterns [165] or coil combination [166].

Aside from the general phase problems, real-time MRI data provides additional challenges. The first challenge is that the large amount of measured data requires fast and simple algorithms. This is especially true for phase measurements, since phase unwrapping algorithms can usually not be parallelized. The second challenge is the presence of motion, which must be considered during phase unwrapping of real-time MRI data.

Phase unwrapping algorithms have been developed for Dixon real-time water-fat separation and real-time phase-contrast flow MRI. The phase unwrapping algorithm for the Dixon real-time water-fat separation is described in 6.3.3 as an extension to the Dixon water-fat separation method.

The phase unwrapping method for real-time phase-contrast flow MRI described in the following sections has been published by the author, including figures 7.1, 7.2, 7.3, 7.5, 7.6 [165].

7.1 Theory

For phase unwrapping of real-time phase-contrast flow MRI data a path integration method along both the temporal and the spatial domain within a region-of-interest (ROI) is used. The algorithm presented in figure 7.1 and the following sections follows previous ideas that combined temporal and spatial velocity-encoded MRI signals in the presence of vascular movements [167, 168].

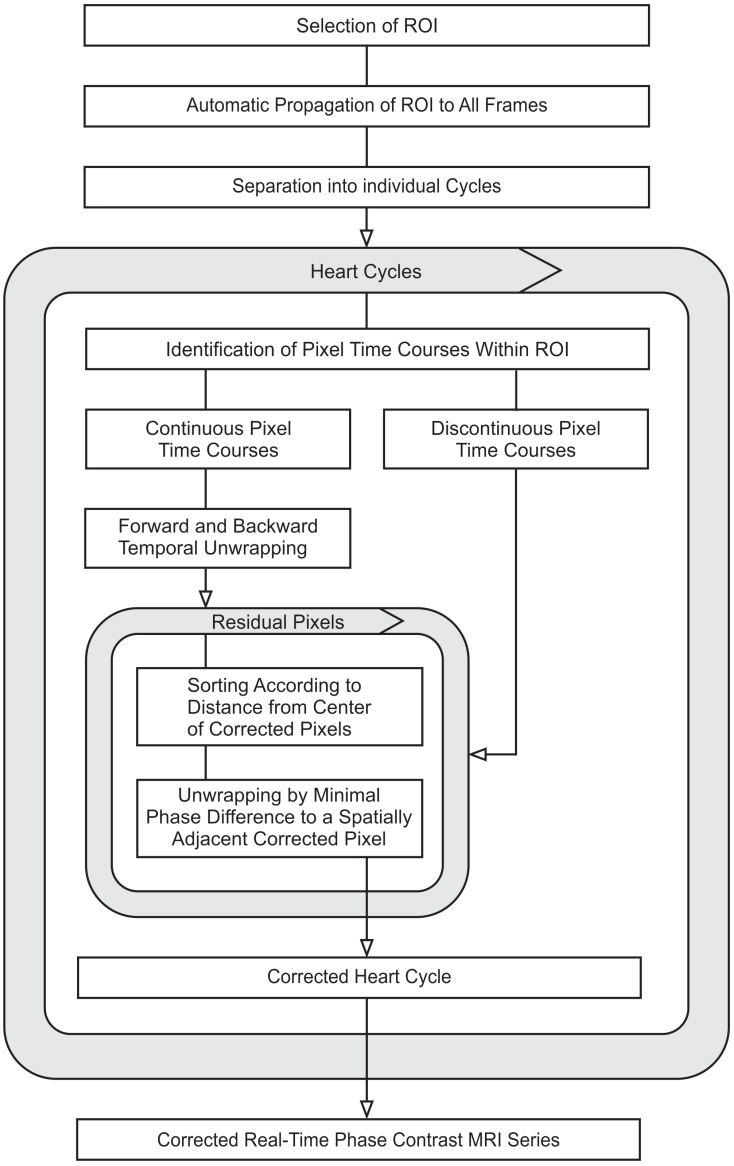

Figure 7.1: Schematic outline of the algorithm proposed for phase unwrapping of real-time phase-contrast flow MRI data.

7.1.1 Preprocessing

The ROI definition is obtained from a preprocessing step. The preprocessing of MRI data starts with the manual definition of a ROI in a single diastolic magnitude image as depicted in 7.2 (top row, left-most image). In this example the ROI covers the ascending aorta with phase wraps during systole (7.2, second row). Its contours are automatically propagated to all magnitude images and phase-contrast maps (7.2, third row). The underlying method is part of the CAIPI (Integrated Processing of Multimodal Cardiac Image Data) prototype software for the analysis of cardiovascular image data (Fraunhofer MEVIS, Bremen,Germany) and has been described in detail [169, 170]. Briefly, in order to transfer the delineation of the ROI to the entire series of images, the vessel motion is estimated using the Morphon approach, a phase-based registration method [170]. The calculated motion is used to propagate the vessel boundaries from the reference frame through the image series. This process is implemented as a two-step approach to minimize error propagation. First, the image series is split into individual heart cycles.

Starting from the reference frame, in which the contour was drawn,corresponding time frames in other heart cycles are identified in accordance to the detected contraction phase. The Morphon approach is applied to compensate for spatial displacements due to breathing between these time frames. This non-rigid registration method estimates the deformation between two frames from the phase difference between quadrature filter responses, which are intensity-invariant and proportional to the spatial change. This calculation is iterated in a scale space to handle both noise and motion in different orders of magnitude. In a second step, the contours of these reference frames are propagated through each cardiac cycle using serial deformation fields calculated with the same method.

7.1.2 Phase Unwrapping

After propagation of the ROI and automatic separation of a real-time MRI series into successive cardiac cycles for individual analyses, a first step refers to the identification of pixels with a continuous signal intensity time course within the previously defined ROIs $R_1, ..., R_n$. These pixels x are defined as

$$\{x : x \in \bigcap_{i=1}^{N} R_i\} \tag{7.1}$$

and represent blood signal throughout the entire cardiac cycle. They mainly refer to the inner area of a vessel which may be spatially displaced due to cardiac movements or free breathing. Accordingly, pixels in the outer zones of each ROI eventually exhibit a discontinuous signal intensity time course, in the sense that they represent aortic blood during one part of the cardiac cycle and surrounding tissue outside the aorta at other times. Discontinuous pixels y are defined as

$$\{y : y \in R_i, i \in \{1, ..., N\} \wedge \notin \bigcap_{i=1}^{N}\} \tag{7.2}$$

The third row in 7.2 depicts the masks obtained for continuous (gray) and discontinuous pixels (black). Continuous time series are unwrapped by a pixelwise application of Itoh's method: First in a forward direction and secondly backwards with reverse temporal ordering. Itoh's method relies on the initial identification of a time point with correct phase value, i.e. without phase wrapping. This condition is easily fulfilled as many phases during a cardiac cycle exhibit only low flow velocities. Respective diastolic frames are identified using the co-registered ECG time stamp, e.g. see the left-most frame in the second row of 7.2. Secondly, the phase difference between the initial time point and the next time point is calculated and added to the initial phase. This step is repeated with the newly unwrapped time point as initial value until the end of the time course or path is reached. If the initial pixel has a correct phase and if all phase differences are between $-\pi$ and π, then all phases will be unwrapped correctly. In fact, this latter condition is fulfilled if the phase values obtained by forward and backward propagation agree. An example is shown in 7.3 (left column) for a real-time MRI study of the human aorta. Phase wrapping at VENC = $100\,\mathrm{cm\,s^{-1}}$ was simulated using data of an acquisition at VENC = $200\,\mathrm{cm\,s^{-1}}$ which served as ground truth. Residual pixels with continuous time courses but temporally inconsistent phase values are sorted according to their distance from the center of gravity of already corrected pixels. Starting with the most central uncorrected pixel, the phase differences with its already corrected nearest neighbors (maximum of 4) are calculated. Unwrapping is then performed by adding the minimum phase difference to the initial value (7.3 middle column). This approach ensures – and inherently assumes – a very local (i.e., pixelwise) smoothness or spatial continuity

of the phase (i.e., flow) within a vessel, while moving from inner corrected pixels to outer still uncorrected pixels. Subsequently, the same strategy is applied to all pixels with a discontinuous time course, again by pursuing a "circular" growth from the inner zone of pixels with reliable phase unwrapping to the periphery of the vessel lumen. The entire procedure is outlined in 7.3 depicting the treatment of two continuous signal intensity time courses with and without identical phases during forward and backward treatment (left and middle column, respectively) as well as a discontinuous time course (right column).

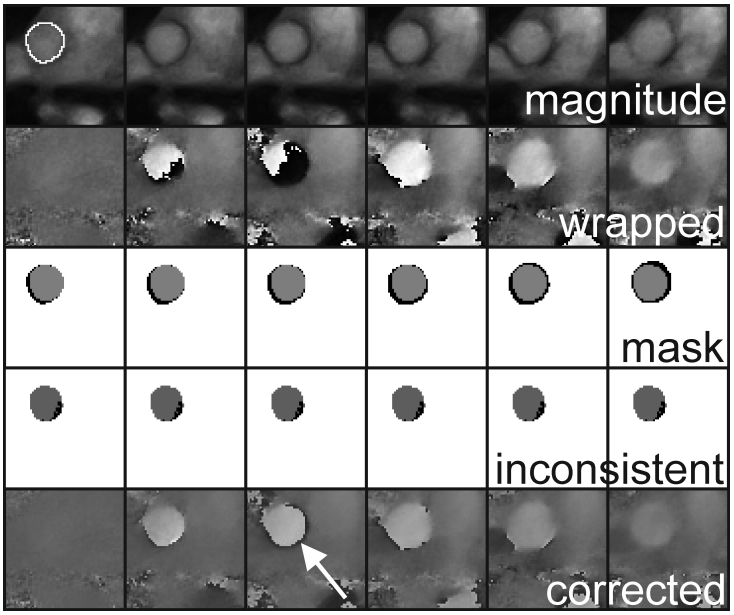

Figure 7.2: Real-time phase-contrast flow MRI of the human aorta at VENC = $100\,\mathrm{cm\,s^{-1}}$ (simulated). (Top) Magnitude images with region-of-interest (ROI), (second row) phase-contrast maps with phase wraps, (third row) masks obtained for pixels with a continuous (gray) and discontinuous (black) signal intensity time course, (fourth row) continuous pixels with consistent (gray) and inconsistent (black) forward and backward phase unwrapping, and (bottom) phase-contrast maps after correction. Residual pixels (white arrow) lie outside the analyzed ROI and most likely refer to the vessel wall.

7.2 Methods

7.2.1 Real-Time Phase-contrast Flow MRI

All studies were performed on a clinical 3 T MRI system (Tim Trio, Siemens Healthcare, Erlangen, Germany) using a cardiac coil with 16 anterior and 16 posterior elements. Flow evaluations in real time were accomplished with the use of a highly undersampled radial FLASH sequence with image reconstruction by regularized nonlinear inversion (NLINV) [8, 76]. The NLINV method was modified for phase-contrast flow MRI to yield phase-sensitive reconstructions of two series of differently flow-encoded images, while phase-contrast maps were obtained without any temporal filter [53, 59, 76]. Magnitude images and phase-contrast maps were computed online using a server with 2 x 4 graphics processing units (sysGen/TYAN Octuple-GPU, 2x Intel Westmere E5620 processor, 48GB RAM, Sysgen, Bremen, Germany) which was fully integrated into the reconstruction pipeline of the commercial MRI system [9, 50].

For both phantom and human studies two sequential images with and without a bipolar flow-encoding gradient were obtained from only 7 spokes within an acquisition time of slightly above

20 ms each [76]. In order to allow for a proper VNR analysis, the measurements with VENC = 200 cm s^{-1} were performed with the same temporal resolution of 43.4 ms as required for VENC = 100 cm s^{-1}. The experimental parameters for phase-contrast flow MRI were: repetition time TR = 3.10 ms, echo time TE = 2.21 ms, flip angle 10°, nominal in-plane resolution 1.3 x 1.3 mm^2, and slice thickness 6 mm. Dynamic reconstructions of phase-contrast maps therefore correspond to a rate of 23 frames per second.

The algorithm for phase unwrapping was developed in MATLAB (MathWorks, Natick, MA) and a respective offline implementation was applied for analyzing the data of the present study.

7.2.2 Phantom Studies

The flow phantom was made of acrylic glass and filled with stationary water. It comprised two tubes (i.e., 10 and 20 mm diameter) performing a U turn in a coronal plane which resulted in four areas of through-plane flow (two tubes, two directions). The tubes are connected outside the phantom and flow is driven by a computer-controlled immersion pump (Lux Plus KTW270, Herzog, Göttingen, Germany). Pulsatile flow as in the human aorta was generated by a repetitive pump protocol with a brief period (0.4 s) of high velocity followed by a longer period (1.6 s) of lower velocity (repetition cycle 2.0 s). High-flow and low-flow conditions referred to pump voltages differing by a factor two [75]. During high-flow conditions phase wraps occurred for VENC = 100 cm s^{-1} but not for VENC = 200 cm s^{-1}.

Human Studies

Ten young volunteers without known illness and contraindications for MRI participated in the study. The study was approved by the institutional review board and written informed consent was obtained from each subject before MRI. Blood flow was measured during free breathing and simultaneously in the ascending and descending aorta using a single plane perpendicular to the ascending aorta at the level of the right pulmonary artery. For each volunteer phase-contrast flow MRI was performed with VENC = 100 cm s^{-1} (three measurements) and VENC = 200 cm s^{-1} (one measurement). Depending on where a phase wrap occurred, either the ascending or descending aorta was unwrapped and analyzed.

7.2.3 Simulated Data

Simulations were performed using human flow MRI data with VENC = 200 cm s^{-1} and no phase wraps. Simulated phase wraps were generated by retrospectively reducing the phase interval from $[-\pi, \pi]$ to $[-\pi/2, \pi/2]$. Values above $\pi/2$ (below $-\pi/2$) were added (subtracted) by π, while all values within $[-\pi/2, \pi/2]$ remained unchanged. To obtain wrapped phase data within $[-\pi, \pi]$ all values were subsequently multiplied by two. The corresponding artificial VENC = 100 cm s^{-1} data sets were unwrapped and analyzed the same way as applied for the true VENC = 100 cm s^{-1} phantom and human data and the results were compared to the evaluations of the original VENC = 200 cm s^{-1} data without phase wraps (ground truth).

7.2.4 Velocity-to-Noise Ratio

For each time frame the phase-contrast flow MRI reconstruction yields two differently flow-encoded sets of $c = [1, \ldots, M]$ complex images $\rho_{1,c}$ and $\rho_{2,c}$ where M denotes the number of MRI receive channels. These sets of images are combined into a single complex phase-contrast map

$$\rho_{pc} = \sum_{c=1}^{M} \rho_{1,c} \bar{\rho}_{2,c} \tag{7.3}$$

where the bar represents the complex conjugate. The phase of ρ_{pc} is converted into a velocity map. The VNR is calculated according

$$\mathrm{VNR} = \frac{|v|\,\pi}{\mathrm{VENC}}\mathrm{SNR} \tag{7.4}$$

where $|v|$ is the mean value of the absolute velocity in a ROI and the SNR is taken from the magnitude images of ρ_{pc} [171, 172].
Possible VNR improvements were evaluated in the phantom and all subjects using single frames with high velocity in the selected ROI. In human subjects these frames referred to peak systole. The SNR of the magnitude image was determined by segmenting the whole image using Otsu's method [123] into a foreground and background signal. The SNR was then calculated by dividing the mean of the foreground by the standard deviation of the background signal.

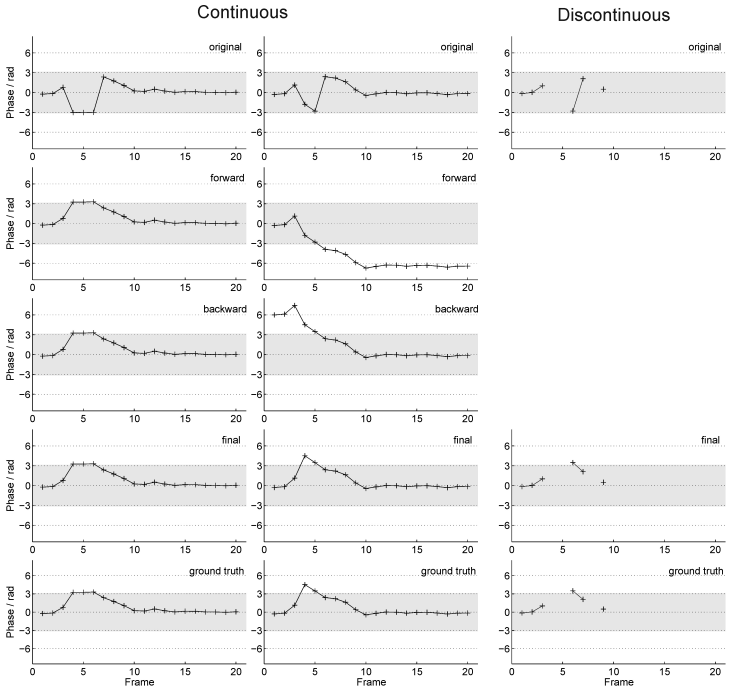

Figure 7.3: Phase unwrapping for three different types of single pixels and real-time phase-contrast flow MRI of the human aorta (single cardiac cycle) at VENC = 100 cm s^{-1} (simulated). (Left) Continuous signal intensity time course with and (middle) without identical phase values for forward and backward unwrapping, (right) discontinuous signal intensity time course. (Top to bottom) The individual traces correspond to the artificially wrapped time courses, forward and backward phase unwrapping with Itoh's method (continuous time courses only), corrected time courses after adding spatial continuity (if applicable), and ground truth obtained for VENC = 200 cm s^{-1}.

7.3 Results

The proposed method for phase unwrapping of real-time phase-contrast flow MRI data resulted in a robust correction of velocity-encoded phase values both in vitro and in vivo. Representative results for an in vivo phase contrast measurement is shown in figure 7.4. The reliability of the approach was first validated using simulated data of a flow phantom and the human aorta as shown in 7.5, where phase wraps occur for flow velocities larger than 100 cm s^{-1}. The traces show

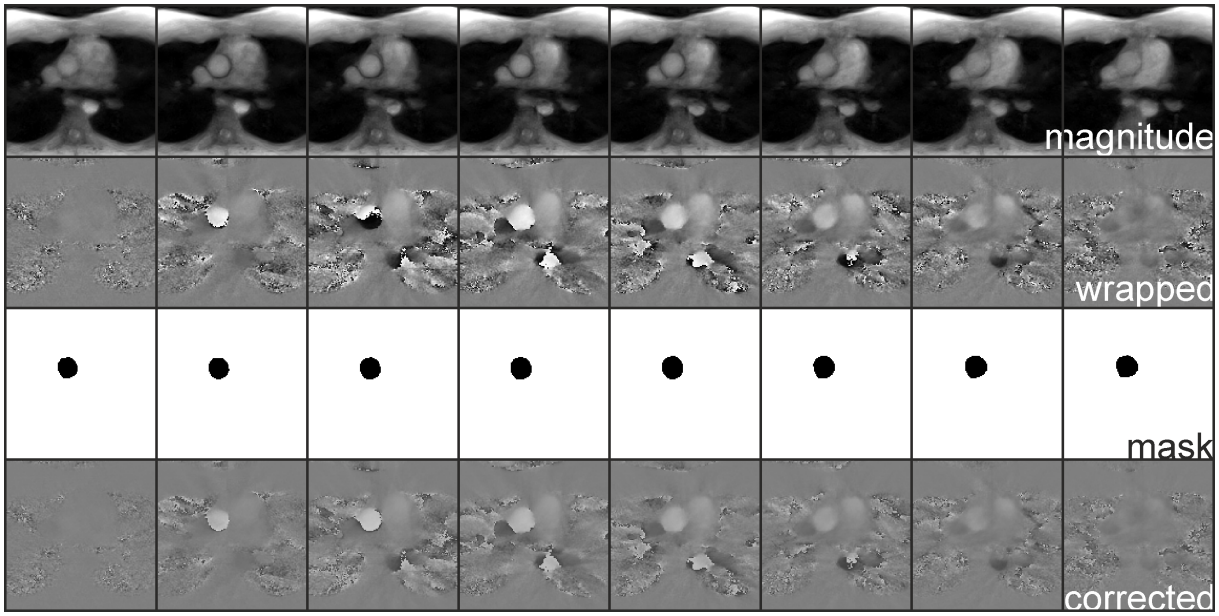

Figure 7.4: Representative results from a real-time phase-contrast flow MRI with VENC = $100\,\mathrm{cm\,s^{-1}}$. (Top) Magnitude images, (second row) phase-contrast maps with phase wraps, (third row) masks obtained for unwrapped pixels, and (bottom) phase-contrast maps after correction.

the mean flow rates averaged across the vessel lumen for the artificially wrapped and corrected data in comparison to ground truth. Without correction the affected flow rates (i.e., flow volumes per unit time) are reduced, whereas phase unwrapping restores correct velocities (not shown) and flow rates.

Complementing the results for single-pixel phase values (velocities) in 7.3, the time frames shown in the bottom row of 7.2 depict corrected phase-contrast maps for the human aorta at $100\,\mathrm{cm\,s^{-1}}$ (simulated). In all cases, i.e. in all pixels of the propagated ROIs, phase unwrapping exactly restored the phase values of the original acquisition at VENC = $200\,\mathrm{cm\,s^{-1}}$ (ground truth). Residual pixels (bottom row of 7.2, white arrow) were found outside the analyzed ROI and most likely refer to the vessel wall.

7.6 demonstrates the reliable performance of the phase unwrapping method for prospectively acquired real-time phase-contrast flow MRI data at VENC = $100\,\mathrm{cm\,s^{-1}}$. The example again depicts corrected flow rates for a phantom and the human aorta. The resulting improvement in VNR was close to the expected value of 2 for a halved VENC value in almost all cases (see Table 1). Small deviations in individual subjects were due to variations in SNR of the magnitude images and mean velocities within the ROI. On average, the mean VNR values $\pm$ standard deviation were 9.6 ± 3.2 for VENC = $200\,\mathrm{cm\,s^{-1}}$ (no phase wraps) and 20.0 ± 5.8 for VENC = $100\,\mathrm{cm\,s^{-1}}$ (after phase unwrapping).

7.4 Discussion

This chapter describes a simple and robust approach to phase unwrapping of real-time phase-contrast flow MRI data which extends Itoh's method [36] by exploiting temporal and spatial continuity. Previously, a method for temporal phase unwrapping, which treats all pixel intensity time courses as continuous and only uses forward unwrapping, has been applied to ECG-gated cine flow MRI data [173]. This strategy ignores discontinuous pixel contributions due to motion of the aorta, which seems to be acceptable for the analysis of a single time-averaged cine MRI data

Subject	VENC = 200 cm s^{-1} without phase unwrapping	VENC = 100 cm s^{-1} with phase unwrapping
Phantom	15.4	30.0
1	13.0	26.3
2	9.1	20.2
3	5.1	13.3
4	8.0	20.0
5	5.6	10.9
6	9.2	19.0
7	9.6	20.9
8	12.2	29.5
9	15.5	24.3
10	8.9	15.4
Mean ± SD	9.6 ± 3.2	20.0 ± 5.8

Table 7.1: Velocity-to-noise ratio along the phase dimension for real-time flow MRI. Values refer to peak mean velocities at systole.

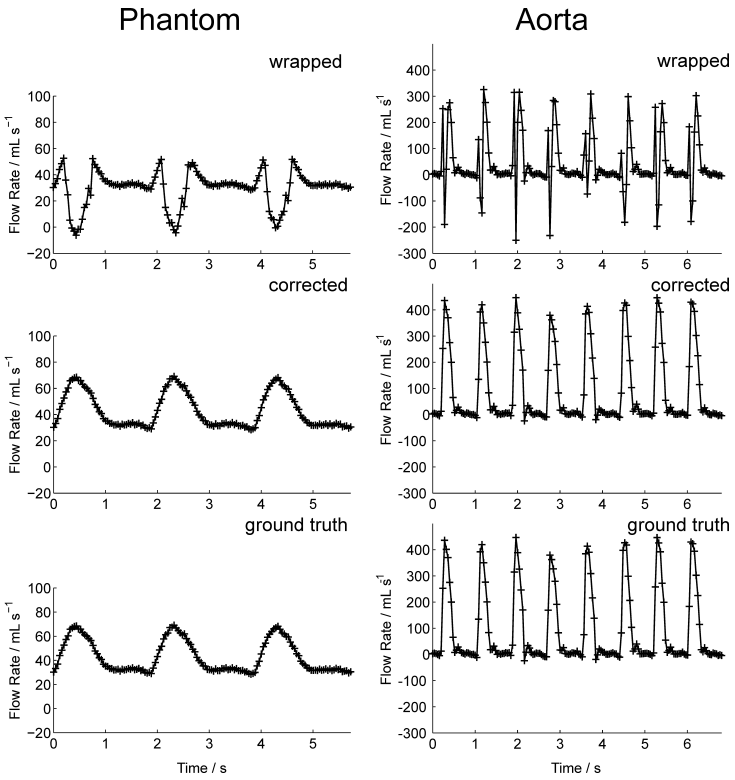

Figure 7.5: Real-time flow rates for (left) a flow phantom and (right) the ascending aorta (single subject). (Top) Simulated phase-wrapped flow MRI data at VENC = 100 cm s^{-1}, (middle) corrected data after phase unwrapping, and (bottom) ground truth for VENC = 200 cm s^{-1}.

set from multiple cardiac cycles. However, in order to benefit from real-time MRI advantages such as free breathing and functional access to individual cardiac cycles, a more elaborate multi-step method for phase unwrapping is required which includes a treatment of pixels with discontinuous signal intensity time courses. On the other hand, the present method is less demanding than a previous method for spatiotemporal phase unwrapping which attempts to track the exact path

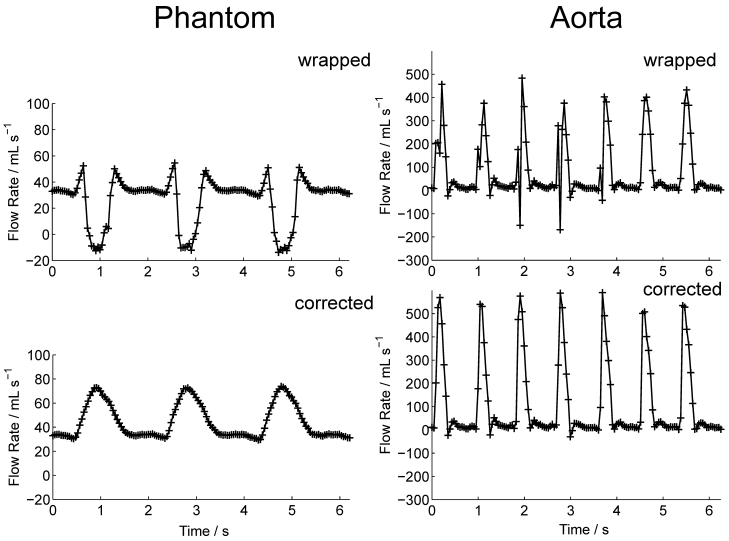

Figure 7.6: Real-time flow rates for (left) a flow phantom and (right) the ascending aorta (single subject) using phase-contrast flow MRI at VENC = 100 cm s^{-1}. (Top) Phase-wrapped data and (bottom) corrected data after phase unwrapping.

of pixel intensities throughout all frames of a cardiac cycle [168]. Provided the vascular ROI as a whole is reliably propagated to cope with movement-related displacements, such a complex task is indeed not necessary as quantitative flow parameters are obtained by integrating phase values across the entire vessel lumen.

A known limitation of the basic Itoh algorithm are higher-order phase wraps if the absolute phase difference between two adjacent time points is equal to or larger than π [36]. In addition, problems may occur for phase wraps in two or three dimensions which increase the degree of complexity as well as the corresponding computational demand, e.g. see [35, 174–176]. It remains to be seen whether these methods may be adapted to unwrap real-time phase-contrast flow MRI data. In general, the need for a phase correction, which is caused by a too low VENC value, should not be confused with the occurrence of phase wraps which are due to the presence of turbulence or other complex flow patterns, e.g. in patients with a stenosis or valve dysfunction. In these cases, phase errors are due to contributions from higher-order through-plane flow (e.g., accelerated flow or jerk) or in-plane flow components which should not be translated into false through-plane velocities by phase unwrapping. Instead, it seems mandatory to minimize respective phase contributions by adding motion-compensating magnetic field gradients to the phase-contrast MRI acquisition technique rather than to seek a correction.

The computation time for the present phase unwrapping method, which was implemented in MATLAB and applied offline, was about 10–15 s for a typical real-time phase-contrast MRI data set of 370 frames. This duration can further be reduced by parallelizing the algorithm, e.g. for multiple cardiac cycles, and by porting the code into a faster programming language like C/C++. In addition, the current workflow for phase unwrapping is tedious, because of the sequential application of two different software packages for segmentation/propagation and phase unwrapping, respectively. However, the currently prepared integration of the phase unwrapping algorithm into the CAIPI software will provide an easy-to-use tool for an almost completely automatic analysis of real-time phase-contrast maps with low VENC values and high VNR based on reliable phase unwrapping. This integration will facilitate more extended clinical trials of large patient cohorts.

7.5 Conclusion

In conclusion, the proposed phase unwrapping method for real-time flow MRI allows for measurements with reduced velocity encoding and increased VNR. By treating individual cardiac cycles with temporal forward and backward unwrapping and by identifying pixels with and without continuous support representing the same tissue throughout the cardiac cycle, the method exploits the true temporal continuity of a real-time MRI acquisition and offers robust performance for moving vessels.

Chapter 8

Summary and Outlook

8.1 Summary

In this thesis MRI methods for T_2^* mapping, water-fat separation and phase-unwrapped flow quantification have been extended to the experimental conditions of a real-time data acquisition and corresponding image reconstruction. The transfer includes the development of a gradient delay correction method for radial MRI with extension to multi-echo data as well as asymmetric gradient echo data.

A basic version of the gradient delay correction has first been presented by Block and Uecker [11]. The extension to multi-echo data is necessary because the trajectories of the different echoes are not considered during gridding. This can be compensated if individual gradient delay corrections for each echo are performed. Considering asymmetric echoes, the data is cropped to a much shorter but symmetric echo data for which the time shift and subsequently the gradient delay is estimated. The robustness and accuracy of the methods were experimentally confirmed. Although motion excerted a strong influence on the gradient delay estimation, the obtained corrections markedly improved the image quality compared to reconstructions from uncorrected data.

For real-time T_2^* mapping only the single-exponential model $f(t) = S_0 \exp(-t/T_2^*)$ with initial value S_0 and decay parameter T_2^* is able to fit the amount of real-time data in a reasonable time of about 0.2 seconds per frame because the model can be linearized. Simulations of the single-exponential fit demonstrated that the sampling length determines the accuracy and precision of the estimated T_2^* value. Up to three times the longest applied gradient-echo time, T_2^* values are estimated with a standard deviation below 5 %. For longer T_2^* values, the standard deviation increases rapidly, producing unreliable fitting results. Switching from linear to non-linear fitting, accuracy and precision improve [110] but the analysis must be restricted to a region of interest for real-time T_2^* mapping.

The influence of motion on T_2^* mapping was investigated with a specially designed motion phantom which rotates an agarose disk [73]. Dephasing during the slice selection gradient and signal enhancement due to inflow of fresh isochromats determine the signal intensity of a single-echo measurement. The T_2^* decay estimated from a multi-echo measurement is altered due to the dephasing along the radial read-out gradients and the resulting T_2^* shortening has been experimentally confirmed.

T_2^* mapping in real-time was applied to the human heart. With a still limited temporal resolution between $50 - 100\,\text{ms}$, cardiac T_2^* maps have been obtained. The low SNR was partly compensated for by using regions-of-interest rather than single pixels for the analyses applied to cardiac T_2^* data. These analyses comprised a Fourier analysis of T_2^* and S_0 time series and the retrospective generation of a single artificial heart cycle at even higher temporal resolution. Both

approaches revealed a periodic variation of T_2^* during the cardiac cycle which apart from residual motion effects may reflect differences in myocardial perfusion and/or oxygenation in agreement with earlier suggestions [16, 105].

Water-fat separation in MRI is possible in many different ways. The most prominent methods are saturation and multi-echo methods. In the conventional saturation method, a saturation pulse is applied before each k-space line. However, utilizing the speed of real-time data acquisitions, a complete frame may be acquired while the saturated magnetization has not completely recovered. The regrowth of the saturated magnetization depends on T_1 which favours water saturation over fat saturation. Successful water/fat saturated MRI movies at a resolution of 0.75 mm could be acquired at 3 and 7 T. A new water-fat separation method using repetitive saturation pulses, continuous data acquisition and a correlation analysis was also developed.

Multi-echo water-fat separation methods separate into the Dixon method [28–31], which requires fixed echo times at in-phase and opposed-phase conditions and echo-time independent methods like 'Direct Phase Encoding' (DPE, [32]), 'Analytical water/fat separation with a safest-first region-growing scheme' (ASR, [33]) and 'Iterative Decomposition of water and fat with Echo Asymmetry and Least-squares' (IDEAL, [34]). All of these methods have been implemented for water-fat separation in real-time MRI though with variable results. As in conventional applications, the quality of the field inhomogeneity map mainly determines the quality of water-fat separation in real-time. Moreover, real-time variants have to exploit the temporal continuity between frames to estimate the field inhomogeneity correctly over time in the presence of motion. In the Dixon method this was achieved by a simple one-dimensional temporal unwrapping of the phase of the field inhomogeneity. For the echo-time independent methods, only ASR and IDEAL allowed for a direct implementation of temporal information. In ASR the region growing is performed framewise with consideration of the previous frame, ensuring a spatially and temporally coherent region growing. In the IDEAL algorithm advantage of temporal information was taken by providing the field map from the previous frame as initial guess of the current field map estimation.

Because a quantitative assessment of fat has become increasingly important in clinical studies, care was taken to correct for respective confounding factors. Because almost all problems could be accounted for in the IDEAL algorithm, it resulted in the most promising real-time solution with optimized spatial and temporal resolution. For example, separate water and fat MRI films of the moving knee with 250 ms per frame and in-plane resolution of 0.75 mm could be acquired.

Phase unwrapping of complex MR images is a complicated task and many algorithms have been proposed [35], but each algorithm encounters situations where it fails. This is mainly due to the presence of noise or the occurrence of phase poles distributed over the image. However, real-time phase-contrast MRI techniques acquire time series of slices with velocity encoding along the slice direction and vessels intersecting the slice perpendicular. Phase-unwrapping can therefore be restricted to the segmented vessel. The additional separation into individual cardiac cycles allows then for a one-dimensional phase-unwrapping algorithm [36] along the temporal axis. The algorithm has been verified in numerical simulations and was demonstrated to correctly treat data of a flow phantom and healthy human subjects. Furthermore, the algorithm was published by the author [165] and shown to allow for a reduced velocity encoding which increases the velocity-to-noise ratio.

8.2 Outlook

In future implementations, the physical gradient delay correction should directly be applied to measured data and therefore incorporated into the image reconstruction algorithm. Its use may supersede an alternative phase correction method [93], as it does not compromise access to

physiological parameters depending on phase.

Real-time T_2^* mapping will further be explored in other anatomical locations like the knee. In this context, the development of a multi-echo multi-spokes sequence will provide images with T_2^* contrast at higher temporal resolution than obtainable by multi-echo single-spoke acquisitions. Together with the assessment of the functional anatomy of the heart T_2^* measurements may provide access to cardiac perfusion and tissue oxygenation. The development of a model-based approach for T_2^* estimation may also increase the accuracy of quantitative determinations.

Because water-fat separation in real-time is a computationally demanding task, respective image reconstructions will be speeded up by porting the optimized IDEAL algorithm to graphical processing units for online display of water and fat maps. A model-based water-fat separation for real-time data which includes temporal information may further improve a quantitative water-fat separation.

The developmental state of the spatiotemporal phase unwrapping technique represents a proof of concept. The next step is the incorporation of the algorithm into the flow analysis software used for real-time MRI data in order to validate its robustness in clinical studies.

Appendix A

Gradient Delay correction

A.1 Radial Gradient Delay Model

In this section the gradient delay model according to Peters [77] is presented. The radial gradient switching scheme in the logical coordinate system is

$$G_{\text{log}} = \begin{bmatrix} G_1 \\ G_2 \\ G_3 \end{bmatrix} = \begin{bmatrix} G_{\text{read}}(t)\cos\theta \\ G_{\text{read}}(t)\sin\theta \\ G_{\text{slice}}(t) \end{bmatrix} \tag{A.1}$$

with the readout angle of the spoke θ and G_{read} as a combination of the three physical gradients. The readout spokes in an arbitrarily oriented slice of the physical coordinate system are rotated by θ around the center of the slice. The delays caused by the physical gradients are found by rotation from the logical coordinate system into the physical coordinate system. The rotation is described by a rotation matrix R_{ij}, $i, j \in \{1, 2, 3\}$, which is defined by the slice orientation.

$$G_{\text{phys}}(t) = \begin{bmatrix} G_x \\ G_y \\ G_z \end{bmatrix} = \begin{bmatrix} R_{11} & R_{12} & R_{13} \\ R_{21} & R_{22} & R_{23} \\ R_{31} & R_{32} & R_{33} \end{bmatrix} \begin{bmatrix} G_{\text{read}}(t)\cos\theta \\ G_{\text{read}}(t)\sin\theta \\ G_{\text{slice}}(t) \end{bmatrix} \tag{A.2}$$

The delay of the gradients is represented here by the time delay operator T:

$$T[G_{\text{phys}}(t)] := \begin{bmatrix} G_x(t - t_{d,x}) \\ G_y(t - t_{d,y}) \\ G_z(t - t_{d,z}) \end{bmatrix} \tag{A.3}$$

The delayed physical gradients are calculated according to equation A.4.

$$G_{\text{phys}}^{\text{del}} = T[RG_{\text{log}}] \tag{A.4}$$

The physical gradient delays must be transformed back into the logical gradient delays, since data is only measured in the logical gradient system.

$$G_{\text{log}}^{\text{del}} = R^T T[RG_{\text{log}}] \tag{A.5}$$

The error between the ideal and delayed trajectory is calculated as the difference between the two trajectories.

$$\Delta k(\tau) = \frac{\gamma}{2\pi}\int_0^\tau G_{\text{log}}^{\text{del}}(t)dt - \frac{\gamma}{2\pi}\int_0^\tau G_{\text{log}}(t)dt \tag{A.6}$$

The shifts of the delayed trajectory in the logical coordinate system are

$$\begin{aligned}\Delta k_1(\theta) = G_{\text{read}}\frac{\gamma}{2\pi}\big(&t_x R_{11}^2\cos(\theta) + t_y R_{21}^2\cos(\theta) + t_z R_{31}^2\cos(\theta) + \\ &+ t_x R_{11}R_{12}\sin(\theta) + t_y R_{22}R_{21}\sin(\theta) + t_z R_{32}R_{31}\sin(\theta)\big) + \\ &- G_{\text{slice}}\frac{\gamma}{2\pi}\left(t_x R_{11}R_{13} + t_y R_{21}R_{23} + t_z R_{31}R_{33}\right)\end{aligned} \tag{A.7}$$

$$\begin{aligned}\Delta k_2(\theta) = G_{\text{read}}\frac{\gamma}{2\pi}\big(&t_x R_{12}^2\sin(\theta) + t_y R_{22}^2\sin(\theta) + t_z R_{32}^2\sin(\theta) + \\ &+ t_x R_{11}R_{12}\cos(\theta) + t_y R_{22}R_{21}\cos(\theta) + t_z R_{32}R_{31}\cos(\theta)\big) + \\ &- G_{\text{slice}}\frac{\gamma}{2\pi}\left(t_x R_{12}R_{13} + t_y R_{22}R_{23} + t_z R_{32}R_{33}\right)\end{aligned} \tag{A.8}$$

$$\begin{aligned}\Delta k_3(\theta) = G_{\text{read}}\frac{\gamma}{2\pi}\big(&t_x R_{11}^2\cos(\theta) + t_y R_{21}^2\cos(\theta) + t_z R_{31}^2\cos(\theta) + \\ &+ t_x R_{11}R_{12}\sin(\theta) + t_y R_{22}R_{21}\sin(\theta) + t_z R_{32}R_{31}\sin(\theta)\big) + \\ &- G_{\text{slice}}\frac{\gamma}{2\pi}\left(t_x R_{13}^2 + t_y R_{23}^2 + t_z R_{33}^2\right)\end{aligned} \tag{A.9}$$

A rotation around the logical z-axis with the angle θ gives then the parallel and perpendicular gradient delays $\Delta k_{\parallel}$ and $\Delta k_{\perp}$ of the spoke acquired at angle θ.

$$\begin{bmatrix}\Delta k_{\parallel}\\ \Delta k_{\perp}\\ \Delta k_3\end{bmatrix} = \begin{bmatrix}\cos\theta & \sin\theta & 0\\ -\sin\theta & \cos\theta & 0\\ 0 & 0 & 1\end{bmatrix}\begin{bmatrix}\Delta k_1(\theta)\\ \Delta k_2(\theta)\\ \Delta k_3(\theta)\end{bmatrix} \tag{A.10}$$

$$\begin{aligned}\Delta k_{\parallel}(\theta) = G_{\text{read}}\frac{\gamma}{2\pi}\big[\ &\cos^2(\theta)\left(t_x R_{11}^2 + t_y R_{21}^2 + t_z R_{31}^2\right) + \\ &\sin^2(\theta)\left(t_x R_{12}^2 + t_y R_{22}^2 + t_z R_{32}^2\right) + \\ &2\cos(\theta)\sin(\theta)\left(t_x R_{11}R_{12} + t_y R_{22}R_{21} + t_z R_{32}R_{31}\right)\big] \\ - G_{\text{slice}}\frac{\gamma}{2\pi}\big[\ &\cos(\theta)\left(t_x R_{11}R_{13} + t_y R_{21}R_{23} + t_z R_{31}R_{33}\right) + \\ &\sin(\theta)\left(t_x R_{12}R_{13} + t_y R_{22}R_{23} + t_z R_{32}R_{33}\right)\big]\end{aligned} \tag{A.11}$$

$$\begin{aligned}\Delta k_{\perp}(\theta) = G_{\text{read}}\frac{\gamma}{2\pi}\big[\ &\cos^2(\theta)\left(t_x R_{11}R_{12} + t_y R_{22}R_{21} + t_z R_{32}R_{31}\right) + \\ &-\sin^2(\theta)\left(t_x R_{11}R_{12} + t_y R_{22}R_{21} + t_z R_{32}R_{31}\right) + \\ &\cos(\theta)\sin(\theta)\left(t_x R_{12}^2 + t_y R_{22}^2 + t_z R_{32}^2 - t_x R_{11}^2 - t_y R_{21}^2 - t_z R_{31}^2\right)\big] \\ - G_{\text{slice}}\frac{\gamma}{2\pi}\big[\ &\cos(\theta)\left(t_x R_{12}R_{13} + t_y R_{22}R_{23} + t_z R_{32}R_{33}\right) \\ &-\sin(\theta)\left(t_x R_{11}R_{13} + t_y R_{21}R_{23} + t_z R_{31}R_{33}\right)\big]\end{aligned} \tag{A.12}$$

$$\begin{aligned}\Delta k_3(\theta) = G_{\text{read}}\frac{\gamma}{2\pi}\big[\ &\cos(\theta)\left(t_x R_{11}^2 + t_y R_{21}^2 + t_z R_{31}^2\right) + \\ &\sin(\theta)\left(t_x R_{11}R_{12} + t_y R_{22}R_{21} + t_z R_{32}R_{31}\right)\ \big] \\ - G_{\text{slice}}\frac{\gamma}{2\pi}\big[\ &t_x R_{13}^2 + t_y R_{23}^2 + t_z R_{33}^2\ \big]\end{aligned} \tag{A.13}$$

Introducing the global delays $t_{g1}, ..., t_{g7}$

$$t_{g1} = t_x R_{11}^2 + t_y R_{21}^2 + t_z R_{31}^2 \tag{A.14}$$
$$t_{g2} = t_x R_{12}^2 + t_y R_{22}^2 + t_z R_{32}^2 \tag{A.15}$$
$$t_{g3} = t_x R_{11} R_{12} + t_y R_{22} R_{21} + t_z R_{32} R_{31} \tag{A.16}$$
$$t_{g4} = t_x R_{11} R_{13} + t_y R_{21} R_{23} + t_z R_{31} R_{33} \tag{A.17}$$
$$t_{g5} = t_x R_{12} R_{13} + t_y R_{22} R_{23} + t_z R_{32} R_{33} \tag{A.18}$$
$$t_{g6} = t_x R_{12}^2 + t_y R_{22}^2 + t_z R_{32}^2 - t_x R_{11}^2 - t_y R_{21}^2 - t_z R_{31}^2 \tag{A.19}$$
$$t_{g7} = t_x R_{13}^2 + t_y R_{23}^2 + t_z R_{33}^2 \tag{A.20}$$

simplify the gradient delays to

$$\Delta k_{\parallel}(\theta) = G_{\text{read}} \frac{\gamma}{2\pi} \left[\cos^2(\theta) t_{g1} + \sin^2(\theta) t_{g2} + 2\cos(\theta)\sin(\theta) t_{g3}\right] - G_{\text{slice}} \frac{\gamma}{2\pi} \left[\cos(\theta) t_{g4} + \sin(\theta) t_{g5}\right] \tag{A.21}$$

$$\Delta k_{\perp}(\theta) = G_{\text{read}} \frac{\gamma}{2\pi} \left[\cos^2(\theta) t_{g3} - \sin^2(\theta) t_{g3} + \cos(\theta)\sin(\theta) t_{g6}\right] - G_{\text{slice}} \frac{\gamma}{2\pi} \left[\cos(\theta) t_{g5} - \sin(\theta) t_{g4}\right] \tag{A.22}$$

$$\Delta k_3(\theta) = G_{\text{read}} \frac{\gamma}{2\pi} \left[\cos(\theta) t_{g1} + \sin(\theta) t_{g3}\right] - G_{\text{slice}} \frac{\gamma}{2\pi} \left[t_{g7}\right] \tag{A.23}$$

A.2 Three-Spokes Estimation

Considering three spokes for the shift estimation, then two almost antiparallel spokes S_{θ_1} and S_{θ_2} at angles θ_1 and θ_2 which encompass the reference spoke S_θ at angle θ as illustrated in figure 4.4 are used. The Fourier transforms of the cross correlations $C(S_\theta, S_{\theta_1})[k]$ and $C(S_\theta, S_{\theta_2})[k]$ are calculated and added subsequently. Shift of $\alpha, \alpha_1, \alpha_2$ are assumed for the three spokes S_θ, S_{θ_1} and S_{θ_2}.

$$\begin{aligned}
g[k] &= \mathcal{F}\left[C(S_\theta, S_{\theta_1})\right][k] + \mathcal{F}\left[C(S_\theta, S_{\theta_2})\right][k] = \mathcal{F}\left[S_\theta\right][k]\overline{\mathcal{F}\left[S_{\theta_1}\right][k]} + \mathcal{F}\left[S_\theta\right][k]\overline{\mathcal{F}\left[S_{\theta_2}\right][k]} \\
&= \mathcal{F}\left[S_0\right][k]\overline{\mathcal{F}\left[S_0\right][k]} \left(\omega^{(\alpha+\alpha_1)k} + \omega^{(\alpha+\alpha_2)k}\right) \\
&= \mathcal{F}\left[S_0\right][k]\overline{\mathcal{F}\left[S_0\right][k]} \cdot \left[2\sin\left(\frac{2\pi}{N}\frac{k}{2}\left(2\alpha+\alpha_1+\alpha_2\right)\right)\cos\left(\frac{2\pi}{N}\frac{k}{2}\left(\alpha_1-\alpha_2\right)\right)\right. \\
&\qquad \left. +2i\cos\left(\frac{2\pi}{N}\frac{k}{2}\left(2\alpha+\alpha_1+\alpha_2\right)\right)\cos\left(\frac{2\pi}{N}\frac{k}{2}\left(\alpha_1-\alpha_2\right)\right)\right] \qquad \text{(A.24)} \\
&= \mathcal{F}\left[S_0\right][k]\overline{\mathcal{F}\left[S_0\right][k]} \cdot \left[\omega^{\frac{1}{2}(2\alpha+\alpha_1+\alpha_2)k}\right]\cos\left(\frac{2\pi}{N}\frac{k}{2}(\alpha_1-\alpha_2)\right) \qquad \text{(A.25)}
\end{aligned}$$

In equation A.25 everything except the ω-term is real and only the complex term contributes to the shift calculation from the phase. The angle of the almost antiparallel spokes is specified as

$\theta_1 = \theta + \pi + \epsilon_1$ and $\theta_1 = \theta + \pi - \epsilon_2$, with $\epsilon_{1,2} \in \mathbb{R}$. The theoretical shift from three spoke is

$$\Delta k_{\text{theory}} = 2\Delta k_{\parallel}(\theta) + \Delta k_{\parallel}(\theta + \pi + \epsilon_1) + \Delta k_{\parallel}(\theta + \pi - \epsilon_2) \tag{A.26}$$

$$= t_{g1}\left[2 + \frac{1}{2}\left(2\cos(2\theta) + 2\cos(2(\theta + \epsilon_1 - \epsilon_2))\cos(\epsilon_1 + \epsilon_2)\right)\right] \tag{A.27}$$

$$+ t_{g2}\left[2 - \frac{1}{2}\left(2\cos(2\theta) + 2\cos(2(\theta + \epsilon_1 - \epsilon_2))\cos(\epsilon_1 + \epsilon_2)\right)\right] \tag{A.28}$$

$$+ 2t_{g3}\left[\sin(2\theta) + \sin(2(\theta + \epsilon_1 - \epsilon_2))\cos(\epsilon_1 + \epsilon_2)\right] \tag{A.29}$$

$$+ t_{g4}\left[2\cos\theta + 2\cos(\theta + \pi + \frac{\epsilon_1 - \epsilon_2}{2})\cos(\frac{\epsilon_1 + \epsilon_2}{2})\right] \tag{A.30}$$

$$+ t_{g5}\left[2\sin\theta + 2\sin(\theta + \pi + \frac{\epsilon_1 - \epsilon_2}{2})\cos(\frac{\epsilon_1 + \epsilon_2}{2})\right] \tag{A.31}$$

With the assumption that $|\epsilon_1 - \epsilon_2| \ll 1$ and $|\epsilon_1 + \epsilon_2| \ll 1$ the arguments of the cosine can be approximated to $\theta + \pi\frac{\epsilon_1 - \epsilon_2}{2} \approx \theta + \pi$ and $\frac{\epsilon_1 - \epsilon_2}{2} \approx 0$. With the previous approximations the shift due to the slice select gradient vanishes and only a shift from the read gradient remains.

$$\Delta k_{\text{theory}} = 4\left(t_{g1}\cos^2\theta + t_{g2}\sin^2\theta + 2t_{g3}\sin\theta\cos\theta\right) \tag{A.32}$$

Bibliography

[1] Peter Mansfield. "Multi-planar image formation using NMR spin echoes". In: *Journal of Physics C: Solid State Physics* 10.3 (1977), p. L55.

[2] J. Frahm, A. Haase, and D. Matthaei. "Rapid NMR imaging of dynamic processes using the FLASH technique." eng. In: *Magn Reson Med* 3.2 (Apr. 1986), pp. 321–327.

[3] K. P. Pruessmann, M. Weiger, M. B. Scheidegger, and P. Boesiger. "SENSE: sensitivity encoding for fast MRI." eng. In: *Magn Reson Med* 42.5 (Nov. 1999), pp. 952–962.

[4] Mark A. Griswold, Peter M. Jakob, Robin M. Heidemann, Mathias Nittka, Vladimir Jellus, Jianmin Wang, Berthold Kiefer, and Axel Haase. "Generalized autocalibrating partially parallel acquisitions (GRAPPA)." eng. In: *Magn Reson Med* 47.6 (June 2002), pp. 1202–1210. DOI: 10.1002/mrm.10171.

[5] Leslie Ying and Jinhua Sheng. "Joint image reconstruction and sensitivity estimation in SENSE (JSENSE)." eng. In: *Magn Reson Med* 57.6 (June 2007), pp. 1196–1202. DOI: 10.1002/mrm.21245.

[6] Martin Uecker, Thorsten Hohage, Kai Tobias Block, and Jens Frahm. "Image reconstruction by regularized nonlinear inversion–joint estimation of coil sensitivities and image content." eng. In: *Magn Reson Med* 60.3 (Sept. 2008), pp. 674–682. DOI: 10.1002/mrm.21691.

[7] Martin Uecker. "Nonlinear Reconstruction Methods for Parallel Magnetic Resonance Imaging". PhD thesis. Goettingen, 2009.

[8] Martin Uecker, Shuo Zhang, Dirk Voit, Alexander Karaus, Klaus-Dietmar Merboldt, and Jens Frahm. "Real-time MRI at a resolution of 20 ms." eng. In: *NMR Biomed* 23.8 (Oct. 2010), pp. 986–994. DOI: 10.1002/nbm.1585.

[9] Sebastian Schaetz and Martin Uecker. "A Multi-GPU Programming Library for Real-Time Applications". In: *CoRR* abs/1301.1215 (2013).

[10] Martin Uecker, Shuo Zhang, and Jens Frahm. "Nonlinear inverse reconstruction for real-time MRI of the human heart using undersampled radial FLASH." eng. In: *Magn Reson Med* 63.6 (June 2010), pp. 1456–1462. DOI: 10.1002/mrm.22453.

[11] K. T. Block and M. Uecker. "Simple Method for Adaptive Gradient-Delay Compensation in Radial MRI". In: *In Proc. Intl. Soc. Mag. Reson. Med. 19.* 2011.

[12] Markus Untenberger, Zhenggou Tan, Dirk Voit, Arun Joseph, Volkert Roeloffs, Klaus-Dietmar Merbold, Sebastian Schaetz, and Jens Frahm. "Advances in Real-time Phase-Contrast Flow MRI using Asymmetric Radial Gradient Echoes". In: *Magnetic Resonance in Medicine* (2015, accepted).

[13] Tallal Charles Mamisch, Timothy Hughes, Timothy J. Mosher, Christoph Mueller, Siegfried Trattnig, Chris Boesch, and Goetz Hannes Welsch. "T2 star relaxation times for assessment of articular cartilage at 3 T: a feasibility study." eng. In: *Skeletal Radiol* 41.3 (Mar. 2012), pp. 287–292. DOI: 10.1007/s00256-011-1171-x.

[14] John C. Wood, Cathleen Enriquez, Nilesh Ghugre, J Michael Tyzka, Susan Carson, Marvin D. Nelson, and Thomas D. Coates. "MRI R2 and R2* mapping accurately estimates hepatic iron concentration in transfusion-dependent thalassemia and sickle cell disease patients." eng. In: *Blood* 106.4 (Aug. 2005), pp. 1460–1465. DOI: 10.1182/blood-2004-10-3982.

[15] Ruiliang Bai, Cheng Guan Koay, Elizabeth Hutchinson, and Peter J. Basser. "A framework for accurate determination of the T2 distribution from multiple echo magnitude MRI images." eng. In: *J Magn Reson* 244 (July 2014), pp. 53–63. DOI: 10.1016/j.jmr.2014.04.016.

[16] K. R. Thulborn, J. C. Waterton, P. M. Matthews, and G. K. Radda. "Oxygenation dependence of the transverse relaxation time of water protons in whole blood at high field." eng. In: *Biochim Biophys Acta* 714.2 (Feb. 1982), pp. 265–270.

[17] M. E. Meyer, O. Yu, B. Eclancher, D. Grucker, and J. Chambron. "NMR relaxation rates and blood oxygenation level." eng. In: *Magn Reson Med* 34.2 (Aug. 1995), pp. 234–241.

[18] Dinesh G. Nair. "About being BOLD." eng. In: *Brain Res Brain Res Rev* 50.2 (Dec. 2005), pp. 229–243. DOI: 10.1016/j.brainresrev.2005.07.001.

[19] E. Angelucci, G. M. Brittenham, C. E. McLaren, M. Ripalti, D. Baronciani, C. Giardini, M. Galimberti, P. Polchi, and G. Lucarelli. "Hepatic iron concentration and total body iron stores in thalassemia major." eng. In: *N Engl J Med* 343.5 (Aug. 2000), pp. 327–331. DOI: 10.1056/NEJM200008033430503.

[20] N. F. Olivieri and G. M. Brittenham. "Iron-chelating therapy and the treatment of thalassemia." eng. In: *Blood* 89.3 (Feb. 1997), pp. 739–761.

[21] Jens-Peter Kühn, Diego Hernando, Birger Mensel, Paul C. Krüger, Till Ittermann, Julia Mayerle, Norbert Hosten, and Scott B. Reeder. "Quantitative chemical shift-encoded MRI is an accurate method to quantify hepatic steatosis." eng. In: *J Magn Reson Imaging* 39.6 (June 2014), pp. 1494–1501. DOI: 10.1002/jmri.24289.

[22] Scott B. Reeder, Irene Cruite, Gavin Hamilton, and Claude B. Sirlin. "Quantitative Assessment of Liver Fat with Magnetic Resonance Imaging and Spectroscopy." eng. In: *J Magn Reson Imaging* 34.4 (Oct. 2011), spcone. DOI: 10.1002/jmri.22775.

[23] Houchun Harry Hu, Peter Börnert, Diego Hernando, Peter Kellman, Jingfei Ma, Scott Reeder, and Claude Sirlin. "ISMRM workshop on fat-water separation: insights, applications and progress in MRI." eng. In: *Magn Reson Med* 68.2 (Aug. 2012), pp. 378–388. DOI: 10.1002/mrm.24369.

[24] Susanne Bonekamp, An Tang, Arian Mashhood, Tanya Wolfson, Christopher Changchien, Michael S. Middleton, Lisa Clark, Anthony Gamst, Rohit Loomba, and Claude B. Sirlin. "Spatial distribution of MRI-Determined hepatic proton density fat fraction in adults with nonalcoholic fatty liver disease." eng. In: *J Magn Reson Imaging* 39.6 (June 2014), pp. 1525–1532.

[25] Russell N. Low, Jingfei Ma, and Neeraj Panchal. "Fast spin-echo triple-echo Dixon: initial clinical experience with a novel pulse sequence for fat-suppressed T2-weighted abdominal MR imaging." eng. In: *J Magn Reson Imaging* 30.3 (Sept. 2009), pp. 569–577. DOI: 10.1002/jmri.21880.

[26] Ethan K. Brodsky, Venkata V. Chebrolu, Walter F. Block, and Scott B. Reeder. "Frequency response of multipoint chemical shift-based spectral decomposition." eng. In: *J Magn Reson Imaging* 32.4 (Oct. 2010), pp. 943–952. DOI: 10.1002/jmri.22308.

[27] Huanzhou Yu, Scott B. Reeder, Ann Shimakawa, Jean H. Brittain, and Norbert J. Pelc. "Field map estimation with a region growing scheme for iterative 3-point water-fat decomposition." eng. In: *Magn Reson Med* 54.4 (Oct. 2005), pp. 1032–1039. DOI: 10.1002/mrm.20654.

[28] W Thomas Dixon. "Simple proton spectroscopic imaging." In: *Radiology* 153.1 (1984), pp. 189–194.

[29] G. H. Glover and E. Schneider. "Three-point Dixon technique for true water/fat decomposition with B0 inhomogeneity correction." eng. In: *Magn Reson Med* 18.2 (Apr. 1991), pp. 371–383.

[30] G. H. Glover. "Multipoint Dixon technique for water and fat proton and susceptibility imaging." eng. In: *J Magn Reson Imaging* 1.5 (1991), pp. 521–530.

[31] T. E. Skinner and G. H. Glover. "An extended two-point Dixon algorithm for calculating separate water, fat, and B0 images." eng. In: *Magn Reson Med* 37.4 (Apr. 1997), pp. 628–630.

[32] Q. S. Xiang and L. An. "Water-fat imaging with direct phase encoding." eng. In: *J Magn Reson Imaging* 7.6 (1997), pp. 1002–1015.

[33] Johan Berglund, Lars Johansson, Håkan Ahlström, and Joel Kullberg. "Three-point Dixon method enables whole-body water and fat imaging of obese subjects." eng. In: *Magn Reson Med* 63.6 (June 2010), pp. 1659–1668. DOI: 10.1002/mrm.22385.

[34] Scott B. Reeder, Zhifei Wen, Huanzhou Yu, Angel R. Pineda, Garry E. Gold, Michael Markl, and Norbert J. Pelc. "Multicoil Dixon chemical species separation with an iterative least-squares estimation method." eng. In: *Magn Reson Med* 51.1 (Jan. 2004), pp. 35–45. DOI: 10.1002/mrm.10675.

[35] Dennis C Ghiglia and Mark D Pitt. *Two-Dimensional Phase Unwrapping: Theory, Algorithms and Software*. John Wiley & Sons, 1998.

[36] K. Itoh. "Analysis of the phase unwrapping algorithm." eng. In: *Appl Opt* 21.14 (July 1982), p. 2470.

[37] Mark E. Haacke, Robert W. Brown, Michael R. Thompson, and Ramesh Vankatesan. *Magnetic Resonance Imaging: Physical Principles and Sequence Design*. Wiley-Liss, 1999.

[38] C.P. Slichter. *Principles of Magnetic Resonance*. Solid-State Sciences Series. World Publishing Company, 1990. ISBN: 9780387501574.

[39] A. Abragam. *The Principles of Nuclear Magnetism*. International series of monographs on physics. Clarendon Press, 1961.

[40] Zhi-Pei Liang and Paul C. Lauterbur. *Principles of Magneitc Resonance Imaging: A Signal Processing Perspective*. Ed. by Robert J. Herrick. IEEE Press series in biomedical engineering, 2000.

[41] Matt A. Bernstein, Kevin F. King, and Xiaohong Joe Zhou. *Handboo of MRI Pulse Sequences*. Elsevier Academic Press, 2004.

[42] S. Zhang. "Real-Time Magnetic Resonance Imaging". PhD thesis. Georg -August-Universität Göttingen, 2009.

[43] K. Scheffler and J. Hennig. "Reduced circular field-of-view imaging." eng. In: *Magn Reson Med* 40.3 (Sept. 1998), pp. 474–480.

[44] Jens Frahm, Wolfgang Hanicke, and Klaus-Dietmar Merboldt. "Transverse coherence in rapid FLASH NMR imaging". In: *Journal of Magnetic Resonance (1969)* 72.2 (1987), pp. 307–314.

[45] A. Haase, J. Frahm, D. Matthaei, W. H"anicke, and K-D. Merboldt. "FLASH imaging: rapid NMR imaging using low flip-angle pulses. 1986." eng. In: *J Magn Reson* 213.2 (Dec. 2011), pp. 533–541. DOI: 10.1016/j.jmr.2011.09.021.

[46] R. E. Hendrick, J. B. Kneeland, and D. D. Stark. "Maximizing signal-to-noise and contrast-to-noise ratios in FLASH imaging." eng. In: *Magn Reson Imaging* 5.2 (1987), pp. 117–127.

[47] J. Frahm, K. D. Merboldt, W. H"anicke, and A. Haase. "Flow suppression in rapid FLASH NMR images." eng. In: *Magn Reson Med* 4.4 (Apr. 1987), pp. 372–377.

[48] Nilesh R. Ghugre, Cathleen M. Enriquez, Thomas D. Coates, Marvin D Nelson Jr, and John C. Wood. "Improved R2* measurements in myocardial iron overload." eng. In: *J Magn Reson Imaging* 23.1 (Jan. 2006), pp. 9–16. DOI: 10.1002/jmri.20467.

[49] Vincenzo Positano, Alessia Pepe, Maria Filomena Santarelli, Barbara Scattini, Daniele De Marchi, Anna Ramazzotti, Gianluca Forni, Caterina Borgna-Pignatti, Maria Eliana Lai, Massimo Midiri, Aurelio Maggio, Massimo Lombardi, and Luigi Landini. "Standardized T2* map of normal human heart in vivo to correct T2* segmental artefacts." eng. In: *NMR Biomed* 20.6 (Oct. 2007), pp. 578–590. DOI: 10.1002/nbm.1121.

[50] M. Uecker, S. Zhang, D. Voit, K Dietmar Merboldt, and J. Frahm. "Real-time MRI - recent advances using radial FLASH". In: *Imaging in Medicine* 4 (2012), pp. 461–479.

[51] Paul R. Moran. "A flow velocity zeugmatographic interlace for {NMR} imaging in humans". In: *Magnetic Resonance Imaging* 1.4 (1982). Second Annual Meeting of the Society for Magnetic Resonance Imaging, pp. 197–203. ISSN: 0730-725X. DOI: http://dx.doi.org/10.1016/0730-725X(82)90170-9.

[52] D. J. Bryant, J. A. Payne, D. N. Firmin, and D. B. Longmore. "Measurement of flow with NMR imaging using a gradient pulse and phase difference technique." eng. In: *J Comput Assist Tomogr* 8.4 (Aug. 1984), pp. 588–593.

[53] Arun A. Joseph, Klaus-Dietmar Merboldt, Dirk Voit, Shuo Zhang, Martin Uecker, Joachim Lotz, and Jens Frahm. "Real-time phase-contrast MRI of cardiovascular blood flow using undersampled radial fast low-angle shot and nonlinear inverse reconstruction." eng. In: *NMR Biomed* 25.7 (July 2012), pp. 917–924. DOI: 10.1002/nbm.1812.

[54] Shuo Zhang, Kai Tobias Block, and Jens Frahm. "Magnetic resonance imaging in real time: advances using radial FLASH." eng. In: *J Magn Reson Imaging* 31.1 (Jan. 2010), pp. 101–109. DOI: 10.1002/jmri.21987.

[55] Nicole Seiberlich, Philipp Ehses, Jeff Duerk, Robert Gilkeson, and Mark Griswold. "Improved radial GRAPPA calibration for real-time free-breathing cardiac imaging." eng. In: *Magn Reson Med* 65.2 (Feb. 2011), pp. 492–505. DOI: 10.1002/mrm.22618.

[56] Martin Buehrer, Klaas P. Pruessmann, Peter Boesiger, and Sebastian Kozerke. "Array compression for MRI with large coil arrays." eng. In: *Magn Reson Med* 57.6 (June 2007), pp. 1131–1139. DOI: 10.1002/mrm.21237.

[57] Feng Huang, Sathya Vijayakumar, Yu Li, Sarah Hertel, and George R. Duensing. "A software channel compression technique for faster reconstruction with many channels." eng. In: *Magn Reson Imaging* 26.1 (Jan. 2008), pp. 133–141. DOI: 10.1016/j.mri.2007.04.010.

[58] Sebastian Schaetz. *MGPU Library*. Biomedizinische NMR Forschungs GmbH am Pax-Planck Institut fuer Biophysikalische Chemie. URL: http://www.biomednmr.mpg.de/index.php?option=com_content&task=view&id=136&Itemid=43.

[59] J. Frahm, S. Schätz, M. Untenberger, S. Zhang, D. Voit, K. D. Merboldt, J. M. Sohns, J. Lotz, and M. Uecker. "On the Temporal Fidelity of Nonlinear Inverse Reconstructions for Real- Time MRI – The Motion Challenge." eng. In: *The Open Medical Imaging Journal* 8 (2014), pp. 1–7. DOI: 10.2174/1874347101408010001.

[60] Alfredo Restrepo and Liliana Chacon. "A smoothing property of the median filter". In: *IEEE J SP* 42.6 (1994), pp. 1553–1555. DOI: 10.1109/78.286974.

[61] Neal C. Jr. Gallagher and Gary L Wise. "A theoretical analysis of the properties of median filters". In: *IEEE J ASSP* 29.6 (1981), pp. 1136–1141. DOI: 10.1109/TASSP.1981.1163708.

[62] Housen Li, Markus Haltmeier, Shuo Zhang, Jens Frahm, and Axel Munk. "Aggregated motion estimation for real-time MRI reconstruction". In: *Magnetic Resonance in Medicine* (2013), n/a–n/a. ISSN: 1522-2594. DOI: 10.1002/mrm.25020.

[63] T. Sumpf and M. Untenberger. "arrayShow: A Guide to an Open Source Matlab Tool for Complex MRI Data Analysis". In: *In Proc. Intl. Soc. Mag. Reson. Med. 21*. 2013.

[64] Tilman Sumpf. *arrShow*. Biomedizinische NMR Forschungs GmbH am Pax-Planck Institut fuer Biophysikalische Chemie. URL: http://www.biomednmr.mpg.de/index.php?option=com_content&task=view&id=137&Itemid=43.

[65] S. Schaetz, M. Untenberger, A. Niebergall, and J. Frahm. "Motion Phantom for Real-Time MRI". In: *In Proc. Intl. Soc. Mag. Reson. Med. 21*. 2013.

[66] Markus Hüllebrand. *CAIPI: Integrated Processing of Multimodal Cardiac Image Data*. Fraunhofer MEVIS. URL: http://www.mevis.fraunhofer.de/loesungen/caipi-integrated-processing-of-multimodal-cardiac-image-data.html.

[67] Eric W Weisstein. *Least Squares Fitting–Exponential*. MathWorld–A Wolfram Web Resource. URL: http://mathworld.wolfram.com/LeastSquaresFittingExponential.html.

[68] K. A. Kraft, P. P. Fatouros, G. D. Clarke, and P. R. Kishore. "An MRI phantom material for quantitative relaxometry." eng. In: *Magn Reson Med* 5.6 (Dec. 1987), pp. 555–562.

[69] J. O. Christoffersson, L. E. Olsson, and S. Sj"oberg. "Nickel-doped agarose gel phantoms in MR imaging." eng. In: *Acta Radiol* 32.5 (Sept. 1991), pp. 426–431.

[70] M. D. Mitchell, H. L. Kundel, L. Axel, and P. M. Joseph. "Agarose as a tissue equivalent phantom material for NMR imaging." eng. In: *Magn Reson Imaging* 4.3 (1986), pp. 263–266.

[71] F. A. Howe. "Relaxation times in paramagnetically doped agarose gels as a function of temperature and ion concentration." eng. In: *Magn Reson Imaging* 6.3 (1988), pp. 263–270.

[72] P. Walker, R. A. Lerski, R. Mathur-De Vrè, J. Binet, and F. Yane. "Preparation of agarose gels as reference substances for NMR relaxation time measurement. EEC Concerted Action Program." eng. In: *Magn Reson Imaging* 6.2 (1988), pp. 215–222.

[73] S. Schaetz, M. Untenberger, A. Niebergall, and J. Frahm. *Motion Phantom*. Biomedizinische NMR Forschungs GmbH am Pax-Planck Institut fuer Biophysikalische Chemie. URL: http://www.biomednmr.mpg.de/index.php?option=com_content&task=view&id=144&Itemid=43.

[74] A. A. Joseph. "Real-time MRI of Moving Spins Using Undersampled Radial FLASH". PhD thesis. Wuerzburg, 2013.

[75] A. A. Joseph, D. Voit, S. Schätz, K-D. Merboldt, and J. Frahm. "Towards Real-Time 3D Phase-Contrast Flow MRI". In: *In Proc. Intl. Soc. Mag. Reson. Med. 21.* 2013.

[76] Arun Joseph, Johannes T. Kowallick, Klaus-Dietmar Merboldt, Dirk Voit, Sebastian Schaetz, Shuo Zhang, Jan M. Sohns, Joachim Lotz, and Jens Frahm. "Real-time flow MRI of the aorta at a resolution of 40 msec". In: *Journal of Magnetic Resonance Imaging* 40.1 (2014), pp. 206–213. ISSN: 1522-2586. DOI: 10.1002/jmri.24328.

[77] Dana C. Peters, J Andrew Derbyshire, and Elliot R. McVeigh. "Centering the projection reconstruction trajectory: reducing gradient delay errors." eng. In: *Magn Reson Med* 50.1 (July 2003), pp. 1–6. DOI: 10.1002/mrm.10501.

[78] *2D & 3D Shepp-Logan Phantom Standards for MRI.* 2008, pp. 521–526. DOI: 10.1109/ICSEng.2008.15.

[79] C. B. Ahn and Z. H. Cho. "Analysis of eddy currents in nuclear magnetic resonance imaging". In: *Magnetic Resonance in Medicine* 17.1 (1991), pp. 149–163. ISSN: 1522-2594. DOI: 10.1002/mrm.1910170119.

[80] S. B. Reeder, E. Atalar, A. Z. Faranesh, and E. R. McVeigh. "Referenceless interleaved echo-planar imaging." eng. In: *Magn Reson Med* 41.1 (Jan. 1999), pp. 87–94.

[81] Ryan K. Robison, Ajit Devaraj, and James G. Pipe. "Fast, simple gradient delay estimation for spiral MRI." eng. In: *Magn Reson Med* 63.6 (June 2010), pp. 1683–1690. DOI: 10.1002/mrm.22327.

[82] Ch. Boesch, R. Gruetter, and E. Martin. "Temporal and spatial analysis of fields generated by eddy currents in superconducting magnets: Optimization of corrections and quantitative characterization of magnet/gradient systems". In: *Magnetic Resonance in Medicine* 20.2 (1991), pp. 268–284. ISSN: 1522-2594. DOI: 10.1002/mrm.1910200209.

[83] Ethan K. Brodsky, Alexey A. Samsonov, and Walter F. Block. "Characterizing and correcting gradient errors in non-cartesian imaging: Are gradient errors linear time-invariant (LTI)?" In: *Magnetic Resonance in Medicine* 62.6 (2009), pp. 1466–1476. ISSN: 1522-2594. DOI: 10.1002/mrm.22100.

[84] P Speier and F Trautwein. "Robust radial imaging with predetermined isotropic gradient delay correction". In: *In Proc. Intl. Soc. Mag. Reson. Med. 14.* 2006.

[85] P Speier and F Trautwein. "A Calibration for Radial Imaging with Large Inplane Shifts". In: *In Proc. Intl. Soc. Mag. Reson. Med. 13.* 2005.

[86] J. H. Duyn, Y. Yang, J. A. Frank, and J. W. van der Veen. "Simple correction method for k-space trajectory deviations in MRI." eng. In: *J Magn Reson* 132.1 (May 1998), pp. 150–153. DOI: 10.1006/jmre.1998.1396.

[87] Brian M Dale and J. Duerk. "The Use of Measured K-Space Trajectory For Reconstruction of Radial MRI Data". In: *In Proc. Intl. Soc. Mag. Reson. Med. 10.* 2002.

[88] Atsushi Takahashi and Terry Peters. "Compensation of multi-dimensional selective excitation pulses using measured k-space trajectories". In: *Magnetic Resonance in Medicine* 34.3 (1995), pp. 446–456. ISSN: 1522-2594. DOI: 10.1002/mrm.1910340323.

[89] Marcus T. Alley, Gary H. Glover, and Norbert J. Pelc. "Gradient characterization using a Fourier-transform technique". In: *Magnetic Resonance in Medicine* 39.4 (1998), pp. 581–587. ISSN: 1522-2594. DOI: 10.1002/mrm.1910390411.

[90] Tobias Wech, Johannes Tran-Gia, Dietbert Hahn, and Herbert Kösler. "Iterative Trajectory Correction for Radial Projection Imaging". In: *In Proc. Intl. Soc. Mag. Reson. Med. 21.* 2013.

[91] Julianna Ianni and William A Grissom. "k-SPIRiT: Non-Cartesian SPIRiT Image Reconstruction with Automatic Trajectory Error Compensation". In: *In Proc. Intl. Soc. Mag. Reson. Med. 22.* 2014.

[92] Xuelin Cui, John C Gore, and E. Brian Welch. "k-Space Shift Compensation Using an Alternating Gradient Readout Acquisition for Improved Radial Fat-Water MRI". In: *In Proc. Intl. Soc. Mag. Reson. Med. 20.* 2012.

[93] Amir Moussavi, Markus Untenberger, Martin Uecker, and Jens Frahm. "Correction of gradient-induced phase errors in radial MRI". In: *Magn. Reson. Med* 71.1 (2014), pp. 308–312. ISSN: 1522-2594.

[94] Youngkyoo Jung, Yogesh Jashnani, Richard Kijowski, and Walter F. Block. "Consistent non-cartesian off-axis MRI quality: calibrating and removing multiple sources of demodulation phase errors." eng. In: *Magn Reson Med* 57.1 (Jan. 2007), pp. 206–212. DOI: 10.1002/mrm.21092.

[95] Ethan K. Brodsky, Jessica L. Klaers, Alexey A. Samsonov, Richard Kijowski, and Walter F. Block. "Rapid measurement and correction of phase errors from B0 eddy currents: impact on image quality for non-Cartesian imaging." eng. In: *Magn Reson Med* 69.2 (Feb. 2013), pp. 509–515. DOI: 10.1002/mrm.24264.

[96] A. C. Silva, E. L. Barbier, I. J. Lowe, and A. P. Koretsky. "Radial echo-planar imaging." eng. In: *J Magn Reson* 135.1 (Nov. 1998), pp. 242–247. DOI: 10.1006/jmre.1998.1547.

[97] D. Li, D. J. Waight, and Y. Wang. "In vivo correlation between blood T2* and oxygen saturation." eng. In: *J Magn Reson Imaging* 8.6 (1998), pp. 1236–1239.

[98] D. Li, Y. Wang, and D. J. Waight. "Blood oxygen saturation assessment in vivo using T2* estimation." eng. In: *Magn Reson Med* 39.5 (May 1998), pp. 685–690.

[99] M. K. Atalay, S. B. Reeder, E. A. Zerhouni, and J. R. Forder. "Blood oxygenation dependence of T1 and T2 in the isolated, perfused rabbit heart at 4.7T." eng. In: *Magn Reson Med* 34.4 (Oct. 1995), pp. 623–627.

[100] S. B. Reeder, A. A. Holmes, E. R. McVeigh, and J. R. Forder. "Simultaneous noninvasive determination of regional myocardial perfusion and oxygen content in rabbits: toward direct measurement of myocardial oxygen consumption at MR imaging." eng. In: *Radiology* 212.3 (Sept. 1999), pp. 739–747. DOI: 10.1148/radiology.212.3.r99se27739.

[101] David S. Fieno, Steven M. Shea, Yongzhong Li, Kathleen R. Harris, J Paul Finn, and Debiao Li. "Myocardial perfusion imaging based on the blood oxygen level-dependent effect using T2-prepared steady-state free-precession magnetic resonance imaging." eng. In: *Circulation* 110.10 (Sept. 2004), pp. 1284–1290. DOI: 10.1161/01.CIR.0000140673.13057.34.

[102] Christian Jackowski, Wolf Schweitzer, Michael Thali, Kathrin Yen, Emin Aghayev, Martin Sonnenschein, Peter Vock, and Richard Dirnhofer. "Virtopsy: postmortem imaging of the human heart in situ using MSCT and MRI." eng. In: *Forensic Sci Int* 149.1 (Apr. 2005), pp. 11–23. DOI: 10.1016/j.forsciint.2004.05.019.

[103] P. Niemi, B. P. Poncelet, K. K. Kwong, R. M. Weisskoff, B. R. Rosen, T. J. Brady, and H. L. Kantor. "Myocardial intensity changes associated with flow stimulation in blood oxygenation sensitive magnetic resonance imaging." eng. In: *Magn Reson Med* 36.1 (July 1996), pp. 78–82.

[104] M. F. Wendland, M. Saeed, K. Lauerma, A. de Crespigny, M. E. Moseley, and C. B. Higgins. "Endogenous susceptibility contrast in myocardium during apnea measured using gradient recalled echo planar imaging." eng. In: *Magn Reson Med* 29.2 (Feb. 1993), pp. 273–276.

[105] R. M. Judd and B. I. Levy. "Effects of barium-induced cardiac contraction on large- and small-vessel intramyocardial blood volume." eng. In: *Circ Res* 68.1 (Jan. 1991), pp. 217–225.

[106] Pascal Sati, Peter van Gelderen, Afonso C. Silva, Daniel S. Reich, Hellmut Merkle, Jacco A. de Zwart, and Jeff H. Duyn. "Micro-compartment specific T2* relaxation in the brain". In: *NeuroImage* 77 (2013), pp. 268–278. ISSN: 1053-8119. DOI: http://dx.doi.org/10.1016/j.neuroimage.2013.03.005.

[107] Carlton F Hazlewood, Donald C Chang, Buford L Nichols, and Donald E Woessner. "Nuclear magnetic resonance transverse relaxation times of water protons in skeletal muscle". In: *Biophysical journal* 14.8 (1974), pp. 583–606.

[108] A. E. English, K. P. Whittall, M. L. Joy, and R. M. Henkelman. "Quantitative two-dimensional time correlation relaxometry." eng. In: *Magn Reson Med* 22.2 (Dec. 1991), pp. 425–434.

[109] RS Menon, MS Rusinko, and PS Allen. "Proton relaxation studies of water compartmentalization in a model neurological system". In: *Magnetic resonance in medicine* 28.2 (1992), pp. 264–274.

[110] F. Schweser, I. Krumbein, H.-J. Herrmann K.-H. andMentzel, and J. R. Reichenbach. "Which one is the mos accurate and has highest precision? - A comprehensive analysis of T2(*) estimation techniques". In: *Proc. Intl. Soc. Mag. Reon. Med. 22*. 2014.

[111] Phalla Ou, Yansong Zhao, Sara El Fawal, Puja Banka, and Andrew J. Powell. "Cardiac T2 measurements in patients with iron overload: a comparison of imaging parameters and analysis techniques." eng. In: *Magn Reson Imaging* 30.5 (June 2012), pp. 641–648. DOI: 10.1016/j.mri.2011.12.020.

[112] Taigang He, Peter D. Gatehouse, Paul Kirk, Raad H. Mohiaddin, Dudley J. Pennell, and David N. Firmin. "Myocardial T*2 measurement in iron-overloaded thalassemia: an ex vivo study to investigate optimal methods of quantification." eng. In: *Magn Reson Med* 60.2 (Aug. 2008), pp. 350–356. DOI: 10.1002/mrm.21625.

[113] M. Tapanya, K. Wantanajittikul, B. Ngammuang, S. Silvilairat, S. Fuchareon, K. Paiboonsukwong, and Saekho S. "Liver T2* measurements: The best curve fitting model for ROI based method and Pixel based method." In: *Proc. Intl. Soc. Mag. Reson. Med. 22*. 2014.

[114] P. B. Roemer, W. A. Edelstein, C. E. Hayes, S. P. Souza, and O. M. Mueller. "The NMR phased array." eng. In: *Magn Reson Med* 16.2 (Nov. 1990), pp. 192–225.

[115] Jin Yamamura, Regine Grosse, Joachim Graessner, Gritta E. Janka, Gerhard Adam, and Roland Fischer. "Distribution of cardiac iron measured by magnetic resonance imaging (MRI)-R*2." eng. In: *J Magn Reson Imaging* 32.5 (Nov. 2010), pp. 1104–1109. DOI: 10.1002/jmri.22364.

[116] John C. Wood and Leila Noetzli. "Cardiovascular MRI in thalassemia major." eng. In: *Ann N Y Acad Sci* 1202 (Aug. 2010), pp. 173–179. DOI: 10.1111/j.1749-6632.2010.05571.x.

[117] S. B. Reeder, A. Z. Faranesh, J. L. Boxerman, and E. R. McVeigh. "In vivo measurement of T*2 and field inhomogeneity maps in the human heart at 1.5 T." eng. In: *Magn Reson Med* 39.6 (June 1998), pp. 988–998.

[118] DeclanP. O'Regan, MartinaF. Callaghan, Julie Fitzpatrick, RossiP. Naoumova, JosephV. Hajnal, and StephanA. Schmitz. "Cardiac T2* and lipid measurement at 3.0 T-initial experience". In: *European Radiology* 18.4 (Apr. 1, 2008), pp. 800–805. DOI: 10.1007/s00330-007-0814-8.

[119] L. J. Anderson, S. Holden, B. Davis, E. Prescott, C. C. Charrier, N. H. Bunce, D. N. Firmin, B. Wonke, J. Porter, J. M. Walker, and D. J. Pennell. "Cardiovascular T2-star (T2*) magnetic resonance for the early diagnosis of myocardial iron overload." eng. In: *Eur Heart J* 22.23 (Dec. 2001), pp. 2171–2179.

[120] Alessia Pepe, Vincenzo Positano, Maria Filomena Santarelli, Fortunato Sorrentino, Eliana Cracolici, Daniele De Marchi, Aurelio Maggio, Massimo Midiri, Luigi Landini, and Massimo Lombardi. "Multislice multiecho T2* cardiovascular magnetic resonance for detection of the heterogeneous distribution of myocardial iron overload." eng. In: *J Magn Reson Imaging* 23.5 (May 2006), pp. 662–668. DOI: 10.1002/jmri.20566.

[121] Anna Angela Di Tucci, Gildo Matta, Simona Deplano, Attilio Gabbas, Cristina Depau, Daniele Derudas, Giovanni Caocci, Annalisa Agus, and Emanuele Angelucci. "Myocardial iron overload assessment by T2* magnetic resonance imaging in adult transfusion dependent patients with acquired anemias." eng. In: *Haematologica* 93.9 (Sept. 2008), pp. 1385–1388. DOI: 10.3324/haematol.12759.

[122] Gillian C. Smith, John Paul Carpenter, Taigang He, Mohammed H. Alam, David N. Firmin, and Dudley J. Pennell. "Value of black blood T2* cardiovascular magnetic resonance." eng. In: *J Cardiovasc Magn Reson* 13 (2011), p. 21. DOI: 10.1186/1532-429X-13-21.

[123] N Otsu. "A Threshold Selection Method from Gray-Level Histograms". In: *Systems, Man and Cybernetics, IEEE Transactions on* 9.1 (Jan. 1979), pp. 62–66. ISSN: 0018-9472. DOI: 10.1109/TSMC.1979.4310076.

[124] Yongxian Qian, Ashley A. Williams, Constance R. Chu, and Fernando E. Boada. "Multicomponent T2* mapping of knee cartilage: technical feasibility ex vivo." eng. In: *Magn Reson Med* 64.5 (Nov. 2010), pp. 1426–1431. DOI: 10.1002/mrm.22450.

[125] Markus Klarhöfer, Philipp Madörin, Deniz Bilecen, and Klaus Scheffler. "Assessment of muscle oxygenation with balanced SSFP: a quantitative signal analysis." eng. In: *J Magn Reson Imaging* 27.5 (May 2008), pp. 1169–1174. DOI: 10.1002/jmri.21334.

[126] Gustav Andreisek, Lawrence M. White, Marshall S. Sussman, Deanna L. Langer, Chirag Patel, Jason Wen-Shyang Su, Masoom A. Haider, and Jeff A. Stainsby. "T2*-weighted and arterial spin labeling MRI of calf muscles in healthy volunteers and patients with chronic exertional compartment syndrome: preliminary experience." eng. In: *AJR Am J Roentgenol* 193.4 (Oct. 2009), W327–W333. DOI: 10.2214/AJR.08.1579.

[127] K. Block, H. Chandarana, G. Fatterpekar, M. Hagiwara, S. Millia, T. Mulholland, M. Bruno, Ch. Geppert, and D.K. Sodickson. *Improving the Robustness of Clinical T1-Weighted MRI Using Radial VIBE*. www.siemens.com. Mai 2013.

[128] Jimin Ren, Ivan Dimitrov, A Dean Sherry, and Craig R. Malloy. "Composition of adipose tissue and marrow fat in humans by 1H NMR at 7 Tesla." eng. In: *J Lipid Res* 49.9 (Sept. 2008), pp. 2055–2062. DOI: 10.1194/jlr.D800010-JLR200.

[129] Gavin Hamilton, Takeshi Yokoo, Mark Bydder, Irene Cruite, Michael E. Schroeder, Claude B. Sirlin, and Michael S. Middleton. "In vivo characterization of the liver fat H MR spectrum." eng. In: *NMR Biomed* 24.7 (Aug. 2011), pp. 784–790. DOI: 10.1002/nbm.1622.

[130] Diego Hernando, Zhi-Pei Liang, and Peter Kellman. "Chemical shift-based water/fat separation: a comparison of signal models." eng. In: *Magn Reson Med* 64.3 (Sept. 2010), pp. 811–822. DOI: 10.1002/mrm.22455.

[131] Greg J. Stanisz, Ewa E. Odrobina, Joseph Pun, Michael Escaravage, Simon J. Graham, Michael J. Bronskill, and R Mark Henkelman. "T1, T2 relaxation and magnetization transfer in tissue at 3T." eng. In: *Magn Reson Med* 54.3 (Sept. 2005), pp. 507–512. DOI: 10.1002/mrm.20605.

[132] Rebecca Rakow-Penner, Bruce Daniel, Huanzhou Yu, Anne Sawyer-Glover, and Gary H. Glover. "Relaxation times of breast tissue at 1.5T and 3T measured using IDEAL." eng. In: *J Magn Reson Imaging* 23.1 (Jan. 2006), pp. 87–91. DOI: 10.1002/jmri.20469.

[133] Garry E. Gold, Eric Han, Jeff Stainsby, Graham Wright, Jean Brittain, and Christopher Beaulieu. "Musculoskeletal MRI at 3.0 T: relaxation times and image contrast." eng. In: *AJR Am J Roentgenol* 183.2 (Aug. 2004), pp. 343–351. DOI: 10.2214/ajr.183.2.1830343.

[134] M. Untenberger, M. Uecker, D. Voit, and J. Frahm. "Water-Fatat Separation using Time Series Correlation". In: *Proc. Intl. Soc. Mag. Reson. Med. 21*. 2013.

[135] B. D. Coombs, J. Szumowski, and W. Coshow. "Two-point Dixon technique for water-fat signal decomposition with B0 inhomogeneity correction." eng. In: *Magn Reson Med* 38.6 (Dec. 1997), pp. 884–889.

[136] Holger Eggers, Bernhard Brendel, Adri Duijndam, and Gwenael Herigault. "Dual-echo Dixon imaging with flexible choice of echo times." eng. In: *Magn Reson Med* 65.1 (Jan. 2011), pp. 96–107. DOI: 10.1002/mrm.22578.

[137] Qing-San Xiang. "Two-point water-fat imaging with partially-opposed-phase (POP) acquisition: an asymmetric Dixon method." eng. In: *Magn Reson Med* 56.3 (Sept. 2006), pp. 572–584. DOI: 10.1002/mrm.20984.

[138] Jingfei Ma. "Breath-hold water and fat imaging using a dual-echo two-point Dixon technique with an efficient and robust phase-correction algorithm." eng. In: *Magn Reson Med* 52.2 (Aug. 2004), pp. 415–419. DOI: 10.1002/mrm.20146.

[139] Johan Berglund, Hakan Ahlström, Lars Johansson, and Joel Kullberg. "Two-point dixon method with flexible echo times." eng. In: *Magn Reson Med* 65.4 (Apr. 2011), pp. 994–1004. DOI: 10.1002/mrm.22679.

[140] Scott B. Reeder, Philip M. Robson, Huanzhou Yu, Ann Shimakawa, Catherine D G. Hines, Charles A. McKenzie, and Jean H. Brittain. "Quantification of hepatic steatosis with MRI: the effects of accurate fat spectral modeling." eng. In: *J Magn Reson Imaging* 29.6 (June 2009), pp. 1332–1339. DOI: 10.1002/jmri.21751.

[141] Huanzhou Yu, Ann Shimakawa, Charles A. McKenzie, Ethan Brodsky, Jean H. Brittain, and Scott B. Reeder. "Multiecho water-fat separation and simultaneous R2* estimation with multifrequency fat spectrum modeling." eng. In: *Magn Reson Med* 60.5 (Nov. 2008), pp. 1122–1134. DOI: 10.1002/mrm.21737.

[142] G. Brix, S. Heiland, M. E. Bellemann, T. Koch, and W. J. Lorenz. "MR imaging of fat-containing tissues: valuation of two quantitative imaging techniques in comparison with localized proton spectroscopy." eng. In: *Magn Reson Imaging* 11.7 (1993), pp. 977–991.

[143] L. Hilaire, F. W. Wehrli, and H. K. Song. "High-speed spectroscopic imaging for cancellous bone marrow R(2)* mapping and lipid quantification." eng. In: *Magn Reson Imaging* 18.7 (Sept. 2000), pp. 777–786.

[144] F. W. Wehrli, J. Ma, J. A. Hopkins, and H. K. Song. "Measurement of R'2 in the presence of multiple spectral components using reference spectrum deconvolution." eng. In: *J Magn Reson* 131.1 (Mar. 1998), pp. 61–68. DOI: 10.1006/jmre.1997.1327.

[145] D.C. Karampinos, H. Yu, A. Shimakawa, T.E. Han, T.M. Link, S. Majumdar, and R. Krug. "Bone marrow fat fraction mapping in the proximal femur in vivo using IDEAL gradient echo imaging". In: *Proc. Intl. Soc. Mag. Reson. Med. 18.* 2010.

[146] Huanzhou Yu, Charles A. McKenzie, Ann Shimakawa, Anthony T. Vu, Anja C S. Brau, Philip J. Beatty, Angel R. Pineda, Jean H. Brittain, and Scott B. Reeder. "Multiecho reconstruction for simultaneous water-fat decomposition and T2* estimation." eng. In: *J Magn Reson Imaging* 26.4 (Oct. 2007), pp. 1153–1161. DOI: 10.1002/jmri.21090.

[147] Mark Bydder, Takeshi Yokoo, Huanzhou Yu, Michael Carl, Scott B. Reeder, and Claude B. Sirlin. "Constraining the initial phase in water-fat separation." eng. In: *Magn Reson Imaging* 29.2 (Feb. 2011), pp. 216–221. DOI: 10.1016/j.mri.2010.08.011.

[148] Huanzhou Yu, Scott B. Reeder, Charles A. McKenzie, Anja C S. Brau, Ann Shimakawa, Jean H. Brittain, and Norbert J. Pelc. "Single acquisition water-fat separation: feasibility study for dynamic imaging." eng. In: *Magn Reson Med* 55.2 (Feb. 2006), pp. 413–422. DOI: 10.1002/mrm.20771.

[149] Jingfei Ma. "A single-point Dixon technique for fat-suppressed fast 3D gradient-echo imaging with a flexible echo time." eng. In: *J Magn Reson Imaging* 27.4 (Apr. 2008), pp. 881–890. DOI: 10.1002/jmri.21281.

[150] Boris Guiu, Romaric Loffroy, Jean-Michel Petit, Serge Aho, Douraied Ben Salem, David Masson, Patrick Hillon, Jean-Pierre Cercueil, and Denis Krause. "Mapping of liver fat with triple-echo gradient echo imaging: validation against 3.0-T proton MR spectroscopy." eng. In: *Eur Radiol* 19.7 (July 2009), pp. 1786–1793. DOI: 10.1007/s00330-009-1330-9.

[151] Catherine D G. Hines, Huanzhou Yu, Ann Shimakawa, Charles A. McKenzie, Jean H. Brittain, and Scott B. Reeder. "T1 independent, T2* corrected MRI with accurate spectral modeling for quantification of fat: validation in a fat-water-SPIO phantom." eng. In: *J Magn Reson Imaging* 30.5 (Nov. 2009), pp. 1215–1222. DOI: 10.1002/jmri.21957.

[152] Chia-Ying Liu, Charles A. McKenzie, Huanzhou Yu, Jean H. Brittain, and Scott B. Reeder. "Fat quantification with IDEAL gradient echo imaging: correction of bias from T(1) and noise." eng. In: *Magn Reson Med* 58.2 (Aug. 2007), pp. 354–364. DOI: 10.1002/mrm.21301.

[153] Mark Bydder, Takeshi Yokoo, Gavin Hamilton, Michael S. Middleton, Alyssa D. Chavez, Jeffrey B. Schwimmer, Joel E. Lavine, and Claude B. Sirlin. "Relaxation effects in the quantification of fat using gradient echo imaging." eng. In: *Magn Reson Imaging* 26.3 (Apr. 2008), pp. 347–359. DOI: 10.1016/j.mri.2007.08.012.

[154] Venkata V. Chebrolu, Catherine D G. Hines, Huanzhou Yu, Angel R. Pineda, Ann Shimakawa, Charles A. McKenzie, Alexey Samsonov, Jean H. Brittain, and Scott B. Reeder. "Independent estimation of T*2 for water and fat for improved accuracy of fat quantification." eng. In: *Magn Reson Med* 63.4 (Apr. 2010), pp. 849–857. DOI: 10.1002/mrm.22300.

[155] Robert L. Janiczek, Giulio Gambarota, Christopher D J. Sinclair, Tarek A. Yousry, John S. Thornton, Xavier Golay, and Rexford D. Newbould. "Simultaneous T'(2) and lipid quantitation using IDEAL-CPMG." eng. In: *Magn Reson Med* 66.5 (Nov. 2011), pp. 1293–1302. DOI: 10.1002/mrm.22916.

[156] D. Hernando, C D G. Hines, H. Yu, and S. B. Reeder. "Addressing phase errors in fat-water imaging using a mixed magnitude/complex fitting method." eng. In: *Magn Reson Med* 67.3 (Mar. 2012), pp. 638–644. DOI: 10.1002/mrm.23044.

[157] Huanzhou Yu, Ann Shimakawa, Catherine D G. Hines, Charles A. McKenzie, Gavin Hamilton, Claude B. Sirlin, Jean H. Brittain, and Scott B. Reeder. "Combination of complex-based and magnitude-based multiecho water-fat separation for accurate quantification of fat-fraction." eng. In: *Magn Reson Med* 66.1 (July 2011), pp. 199–206. DOI: 10.1002/mrm.22840.

[158] Katie H. Hansen, Michael E. Schroeder, Gavin Hamilton, Claude B. Sirlin, and Mark Bydder. "Robustness of fat quantification using chemical shift imaging." eng. In: *Magn Reson Imaging* 30.2 (Feb. 2012), pp. 151–157. DOI: 10.1016/j.mri.2011.09.011.

[159] Abdullah Alabousi, Salam Al-Attar, Tisha R. Joy, Robert A. Hegele, and Charles A. McKenzie. "Evaluation of adipose tissue volume quantification with IDEAL fat-water separation." eng. In: *J Magn Reson Imaging* 34.2 (Aug. 2011), pp. 474–479. DOI: 10.1002/jmri.22603.

[160] P. A. Bottomley, T. H. Foster, R. E. Argersinger, and L. M. Pfeifer. "A review of normal tissue hydrogen NMR relaxation times and relaxation mechanisms from 1-100 MHz: dependence on tissue type, NMR frequency, temperature, species, excision, and age." eng. In: *Med Phys* 11.4 (1984), pp. 425–448.

[161] David H. Johnson, Sreenath Narayan, Chris A. Flask, and David L. Wilson. "Improved fat-water reconstruction algorithm with graphics hardware acceleration." eng. In: *J Magn Reson Imaging* 31.2 (Feb. 2010), pp. 457–465. DOI: 10.1002/jmri.22051.

[162] L. An and Q. S. Xiang. "Chemical shift imaging with spectrum modeling." eng. In: *Magn Reson Med* 46.1 (July 2001), pp. 126–130.

[163] Scott B. Reeder, Jean H. Brittain, Thomas M. Grist, and Yi-Fen Yen. "Least-squares chemical shift separation for (13)C metabolic imaging." eng. In: *J Magn Reson Imaging* 26.4 (Oct. 2007), pp. 1145–1152. DOI: 10.1002/jmri.21089.

[164] Viola Rieke and Kim Butts Pauly. "MR thermometry." eng. In: *J Magn Reson Imaging* 27.2 (Feb. 2008), pp. 376–390. DOI: 10.1002/jmri.21265.

[165] Markus Untenberger, Markus Hüllebrand, Lennart Tautz, Arun A. Joseph, Dirk Voit, K Dietmar Merboldt, and Jens Frahm. "Spatiotemporal phase unwrapping for real-time phase-contrast flow MRI." eng. In: *Magn Reson Med* (Oct. 2014). DOI: 10.1002/mrm.25471.

[166] Souheil J Inati, Michael S Hansen, and Peter Kellman. "A Solution to the Phase Problem in Adaptive Coil Combination". In: *In Proc. Intl. Soc. Mag. Reson. Med. 21*. 2013.

[167] M. F. Salfity, J. M. Huntley, M. J. Graves, O. Marklund, R. Cusack, and D. A. Beauregard. "Extending the dynamic range of phase contrast magnetic resonance velocity imaging using advanced higher-dimensional phase unwrapping algorithms." eng. In: *J R Soc Interface* 3.8 (June 2006), pp. 415–427. DOI: 10.1098/rsif.2005.0096.

[168] G. Z. Yang, P. Burger, P. J. Kilner, S. P. Karwatowski, and D. N. Firmin. "Dynamic range extension of cine velocity measurements using motion-registered spatiotemporal phase unwrapping." eng. In: *J Magn Reson Imaging* 6.3 (1996), pp. 495–502.

[169] M Hüllebrand, A Hennemuth, D Messroghli, and J Kühne. "An OsiriX plugin for integrated cardiac image processing research". In: *Proc SPIE Med Imaging*. 2014.

[170] L Tautz, A Hennemuth, and HO Peitgen. "Motion analysis with quadrature filter based registration of tagged MRI sequences." In: *In: Statistical Atlases and Computational Models of the Heart. Imaging and Modelling Challenges*. 2011.

[171] T. E. Conturo and G. D. Smith. "Signal-to-noise in phase angle reconstruction: dynamic range extension using phase reference offsets." eng. In: *Magn Reson Med* 15.3 (Sept. 1990), pp. 420–437.

[172] N. J. Pelc, R. J. Herfkens, A. Shimakawa, and D. R. Enzmann. "Phase contrast cine magnetic resonance imaging." eng. In: *Magn Reson Q* 7.4 (Oct. 1991), pp. 229–254.

[173] Q. S. Xiang. "Temporal phase unwrapping for CINE velocity imaging." eng. In: *J Magn Reson Imaging* 5.5 (1995), pp. 529–534.

[174] Satoshi Tomioka and Shusuke Nishiyama. "Phase unwrapping for noisy phase map using localized compensator." eng. In: *Appl Opt* 51.21 (July 2012), pp. 4984–4994.

[175] J. M. Huntley. "Three-dimensional noise-immune phase unwrapping algorithm." eng. In: *Appl Opt* 40.23 (Aug. 2001), pp. 3901–3908.

[176] Wentao Liu, Xin Tang, Yajun Ma, and Jia-Hong Gao. "3D phase unwrapping using global expected phase as a reference: application to MRI global shimming." eng. In: *Magn Reson Med* 70.1 (July 2013), pp. 160–168. DOI: 10.1002/mrm.24448.

Curriculum Vitae

Markus Untenberger

Dipl.-Phys.

Personal Information

Name	Markus Florian Untenberger
Title	Diplom-Physiker
Date of Birth	May 13, 1985 in Villingen-Schwenningen, Germany
Address	Am Pfingstanger 53, 37075 Göttingen, Germany
eMail	untenberger@yahoo.de
	markus.untenberger@mpibpc.mpg.de

Education

since 2010 **PhD Student**, *Biomedizinische NMR Forschungs GmbH am Max-Planck Institut für biophysikalische Chemie*, Göttingen.
Title: Multi-Echo Radial FLASH Techniques for Real-Time MRI
Supervisors: Prof. Dr. Jens Frahm, Prof. Dr. Oliver Speck

2004-2010 **Physics Diploma**, *Universität Konstanz*, Konstanz, *gut.*

1991-2004 **Abitur**, *Gymnasium am Deutenberg*, Villingen-Schwenningen, *1.7.*

Experience

Vocational

2010 **Research Assistant**, *Universität Konstanz*, Konstanz, Diplom-Physiker.
Diffusing-wave spectroscopy with dynamic contrast variation

2008 **Internship**, *Institute for Astronomy, University of Hawaii*, Pukalani.
Developing a control software for a coelostat

2006-2008 **Teaching Assistant**, *Universität Konstanz, Department of Mathematics and Statistics*, Konstanz.
Teaching Courses Mathematik für Physiker 3, Analysis I, Funktionentheorie

Miscellaneous

since 2013 **Team Manager**, *ASC 3rd male volleyballteam*, Göttingen.
Team manager and member of the ASC 3. male volleyballteam

2013 **Meeting Coordinator**, *PhDnet at Max-Planck Society*.
Coordinated the PhDnet General Meeting 2013 in Göttingen

2012-2013 **Team Manager**, *ASC 4th male volleyballteam*, Göttingen.
Team manager and member of the ASC 4. male volleyballteam

2008-2010 **Fire-fighter**, *Volunteer Fire Department Konstanz*, Konstanz.
Member of fire brigade 6

2001-2010 **Fire-fighter**, *Volunteer Fire Department Schwenningen*, Villingen-Schwenningen.

Thesis

Diploma Thesis

Title Diffusing Wave Spectroscopy mit akustischer Markierung

Supervisors PD Dr. Thomas Gisler, Prof. Dr. Georg Maret

Am Pfingstanger 53 – 37075 Gottingen – Germany
+49 (0) 151 507 287 45 • untenberger@yahoo.de